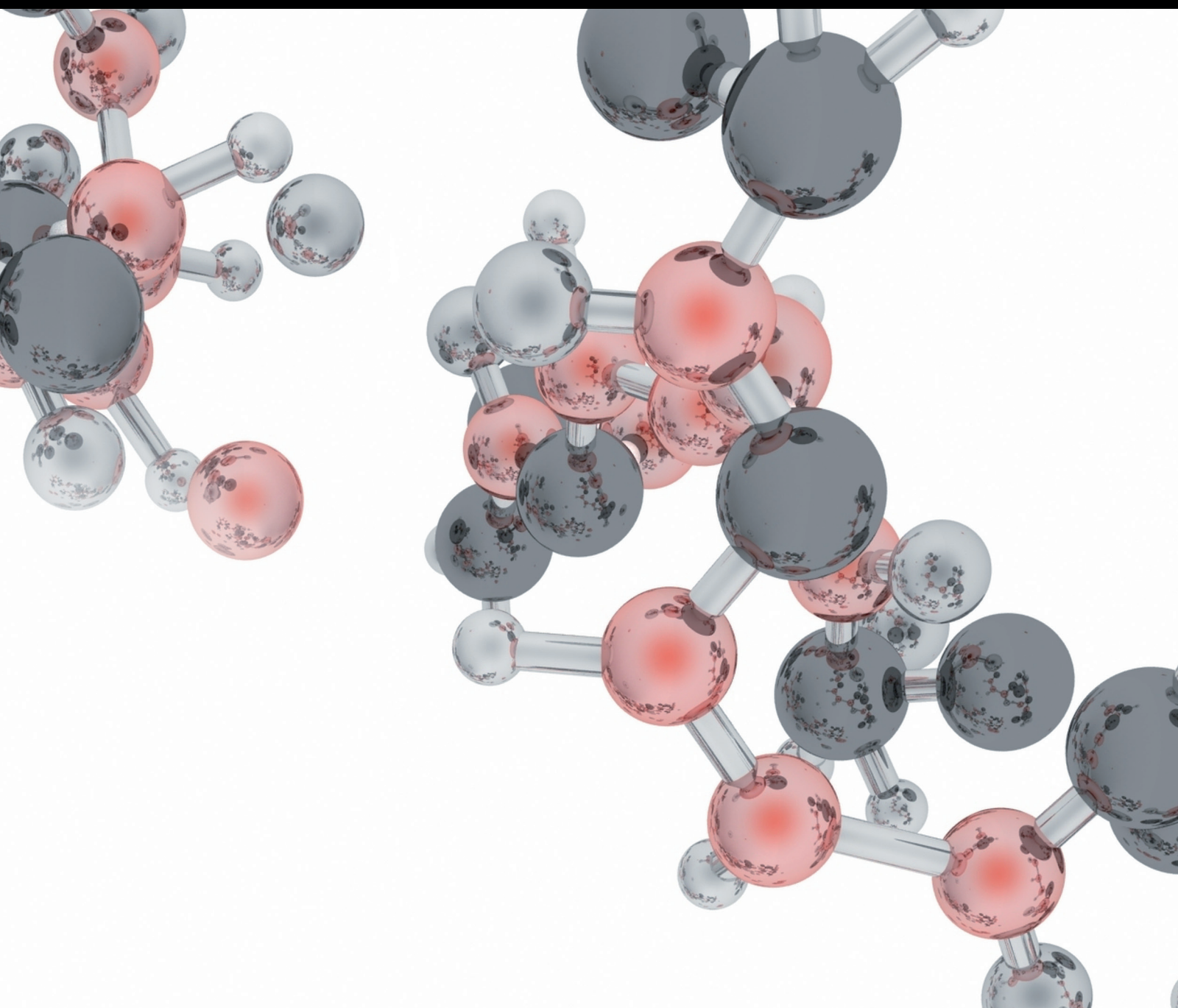


Fluorescence Analysis: From Sensing to Imaging

Lead Guest Editor: Subhankar Singha

Guest Editors: Dokyoung Kim, Sankarprasad Bhuniya, and Tushar Kumeria





Fluorescence Analysis: From Sensing to Imaging

Fluorescence Analysis: From Sensing to Imaging

Lead Guest Editor: Subhankar Singha

Guest Editors: Dokyoung Kim, Sankarprasad Bhuniya,
and Tushar Kumeria



Copyright © 2018 Hindawi. All rights reserved.

This is a special issue published in "Journal of Analytical Methods in Chemistry." All articles are open access articles distributed under the Creative Commons Attribution License, which permits unrestricted use, distribution, and reproduction in any medium, provided the original work is properly cited.

Editorial Board

Mohamed Abdel-Rehim, Sweden
Hassan Y. Aboul Enein, Egypt
Silvana Andreescu, USA
Aristidis N. Anthemidis, Greece
Alessandro Buccolieri, Italy
Antony C. Calokerinos, Greece
Luca Campone, Italy
Ricardo Jorgensen Cassella, Brazil
Angela Chambery, Italy
Igor Chourpa, France
Filomena Conforti, Italy
Guido Crisponi, Italy
Eduardo Dellacassa, Uruguay
Ana María Díez-Pascual, Spain
Gauthier Eppe, Belgium
Josep Esteve-Romero, Spain
Valdemar Esteves, Portugal
Núria Fontanals, Spain
Constantinos Georgiou, Greece
Gabriele Giancane, Italy

Karoly Heberger, Hungary
Antonio V. Herrera-Herrera, Spain
Eliseo Herrero-Hernández, Spain
Bernd Hitzmann, Germany
Chih-Ching Huang, Taiwan
Jaroon Jakmunee, Thailand
Christos Kontoyannis, Greece
Radosław Kowalski, Poland
Eulogio J. Llorent-Martínez, Spain
Mercedes G. Lopez, Mexico
Miren Lopez de Alda, Spain
Larisa Lvova, Italy
Jose Carlos Marques, Portugal
Christophe A. Marquette, France
Serban C. Moldoveanu, USA
Yolanda Moliner Martínez, Spain
Paolo Montuori, Italy
Sibel A. Ozkan, Turkey
Federica Pellati, Italy
Verónica Pino, Spain

Pablo Richter, Chile
Fábio Rodrigo Piovezan Rocha, Brazil
Erwin Rosenberg, Austria
Jose Vicente Ros-Lis, Spain
Giuseppe Ruberto, Italy
Antonio Ruiz Medina, Spain
Bradley B. Schneider, Canada
Jesus Simal-Gandara, Spain
Hana Sklenarova, Czech Republic
Beate Strehlitz, Germany
Luca Tortora, Italy
Marek Trojanowicz, Poland
Bengi Uslu, Turkey
Anna Vallverdu-Queral, France
Krishna K. Verma, India
Brian K. Via, USA
Adam Voelkel, Poland
Rongda Xu, USA
B. M. Nikolova-Damyanova, Bulgaria

Contents

Fluorescence Analysis: From Sensing to Imaging

Subhankar Singha , Dokyoung Kim , Sankarprasad Bhuniya , and Tushar Kumeria 
Editorial (2 pages), Article ID 2654127, Volume 2018 (2018)

A Facile Synthesis of Highly Nitrogen-Doped Carbon Dots for Imaging and Detection in Biological Samples

Qianchun Zhang , Siqi Xie, Yanqun Yang, Yun Wu, Xingyi Wang, Jincheng Wu, Li Zhang, Junyu Chen, and Yuan Wang 
Research Article (9 pages), Article ID 7890937, Volume 2018 (2018)

A Simple Separation Method of the Protein and Polystyrene Bead-Labeled Protein for Enhancing the Performance of Fluorescent Sensor

Hye Jin Kim, Dong-Hoon Kang, Seung-Hoon Yang, Eunji Lee, Taewon Ha, Byung Chul Lee, Youngbaek Kim, Kyo Seon Hwang, Hyun-Joon Shin, and Jinsik Kim 
Research Article (7 pages), Article ID 8461380, Volume 2018 (2018)

Benzo[*g*]coumarin-Based Fluorescent Probes for Bioimaging Applications

Yuna Jung, Junyang Jung , Youngbuhm Huh , and Dokyoung Kim 
Review Article (11 pages), Article ID 5249765, Volume 2018 (2018)

Sensing of Vascular Permeability in Inflamed Vessel of Live Animal

Sang A Park, Soi Jeong , Young Ho Choe , and Young-Min Hyun 
Research Article (6 pages), Article ID 5797152, Volume 2018 (2018)

A Pyridazine-Based Fluorescent Probe Targeting A β Plaques in Alzheimer's Disease

Yong Dae Park , Jeum-Jong Kim, Sungbeom Lee, Chul-Hong Park, Hyoung-Woo Bai, and Seung Sik Lee
Research Article (5 pages), Article ID 1651989, Volume 2018 (2018)

Editorial

Fluorescence Analysis: From Sensing to Imaging

Subhankar Singha ¹, **Dokyoung Kim** ², **Sankarprasad Bhuniya** ³,
and Tushar Kumeria ⁴

¹Department of Chemistry, School of Molecular Science (BK21PLUS), Pohang University of Science and Technology (POSTECH), 77 Cheongam-Ro, Nam-Gu, Pohang, Gyeongbuk 37673, Republic of Korea

²Department of Anatomy and Neurobiology, Center for Converging Humanities, College of Medicine, Kyung Hee University, 26 Kyungheedae-Ro, Dongdaemun-Gu, Seoul 02447, Republic of Korea

³Department of Chemical Engineering and Materials Science, Amrita Centre for Industrial Research and Innovation, Amrita School of Engineering, Amrita Vishwa Vidyapeetham, Coimbatore 64112, India

⁴School of Pharmacy, University of Queensland, 20 Cornwall Street, Woolloongabba, Brisbane, QLD 4102, Australia

Correspondence should be addressed to Subhankar Singha; subhankar@postech.ac.kr

Received 24 June 2018; Accepted 24 June 2018; Published 1 August 2018

Copyright © 2018 Subhankar Singha et al. This is an open access article distributed under the Creative Commons Attribution License, which permits unrestricted use, distribution, and reproduction in any medium, provided the original work is properly cited.

Fluorescence sensing and imaging combined with fluorescence microscopy technology has revolutionized human ability to study and visualize complex life phenomena at the molecular level to understand the cellular events with least ambiguity. Being a simple, fast, direct detection system with real-time monitoring capability, fluorescence sensing is highly demanding for *in vitro* as well as *in vivo* analysis in the recent time. In this special issue, we aim to create a platform for introducing the recent advances in the field of fluorescence-based analysis and imaging techniques.

The promising features of fluorescence analysis in turn have inspired a quest for novel fluorescent materials/fluorophores as well as fluorescence probes/sensors with various applications in imaging. In this respect, development of fluorescent materials based on quantum dots has attracted the current research. Importantly, due to advantageous features of lower cytotoxicity, organic quantum dots are preferred over inorganic ones. In this issue, Zhang et al. report a facile, green, and high-output synthesis of highly fluorescent nitrogen-doped carbon quantum dots which show strong blue fluorescence along with high photostability and excellent biocompatibility. The carbon dots further find the utility as a fluorescence probe for cell imaging as well as for detection of Fe^{3+} in serum.

Due to superiority of two-photon excitation-based imaging techniques, especially in the field of medical sciences,

development of novel two-photon fluorophores is of highest priority. Kim and coworkers introduce a novel two-photon excitable fluorophore-benzo[*g*]coumarin and summarize the photophysical properties and synthetic methods along with the promising applications for bioimaging and sensing of biologically important species using benzo[*g*]coumarin analogues. An advanced application of two-photon intravital fluorescence microscopy is further demonstrated by Hyun and coworkers to report the sensing of vascular permeability from the inflamed vessel of live animals. The investigation shows how blood vessel is ruptured and vascular leakage occurs during acute inflammation in correlation with neutrophil infiltration at the subvascular level under inflammatory condition in the cremaster muscle of mice. Compared to the previously reported methods, this intravital imaging method helps to measure more accurate vascular leakage in terms of time and location *in vivo*.

As the current research on fluorescence sensing and imaging is majorly focused on disease diagnosis, accordingly development of diagnostic imaging agents for disease biomarkers is also important. Park et al. develop a pyridazine-based fluorescent probe targeting amyloid-beta ($A\beta$) peptides, the neuropathological hallmarks of Alzheimer's disease (AD). Besides the key features of selective detection and imaging of $A\beta$ plaques through strong fluorescence enhancement, the reasonable hydrophobic nature for blood-brain barrier (BBB) penetration would be helpful to use the

probe as a promising imaging agent for AD diagnosis in the near future.

Biomolecule labeling is a common trend, in the recent time, to visualize and track the various biological processes. In the course of labeling, it is essential to separate the nonconjugated residues from the molecules conjugated with labels. Through comparing the average intensity of fluorescence, Kim et al. successfully demonstrate a dielectrophoresis-based separation method between the unlabeled protein (unreacted) and the labeled one with polystyrene beads, onto a single electrode platform having two different sizes of microholes. This research is also scientifically appealing for enhancing the performance of fluorescent sensors.

In conclusion, this special issue covers the broad area of fluorescence analysis starting from the development of fluorescent materials to the applications for fluorescence sensing and imaging, thus attracting the attention from the various research areas including Chemistry, Biology, Materials, and Polymers. Moreover, the research articles containing the original research results and the review articles share the current state of the art of this fundamental research area among the readers of this journal.

Subhankar Singha
Dokyoung Kim
Sankarprasad Bhuniya
Tushar Kumeria

Research Article

A Facile Synthesis of Highly Nitrogen-Doped Carbon Dots for Imaging and Detection in Biological Samples

Qianchun Zhang , Siqi Xie, Yanqun Yang, Yun Wu, Xingyi Wang, Jincheng Wu, Li Zhang, Junyu Chen, and Yuan Wang 

School of Biology and Chemistry, Xingyi Normal University for Nationalities, Xingyi 562400, China

Correspondence should be addressed to Qianchun Zhang; qianchunzhang@qq.com and Yuan Wang; 45001490@qq.com

Received 21 March 2018; Accepted 17 May 2018; Published 15 July 2018

Academic Editor: Subhankar Singha

Copyright © 2018 Qianchun Zhang et al. This is an open access article distributed under the Creative Commons Attribution License, which permits unrestricted use, distribution, and reproduction in any medium, provided the original work is properly cited.

A facile, green, and high-output hydrothermal synthesis was proposed for the fabrication of highly fluorescent nitrogen-doped carbon quantum dots (N-doped CDs). The nitrogen content in N-doped CDs reached 19.2% and demonstrated strong blue fluorescence emission was obtained with fluorescence quantum yield (QY) of up to 32.9%, which exhibit high fluorescence quantum yield, high photostability, and excellent biocompatibility. The N-doped CDs possess high photostability, low toxicity, and excellent biocompatibility, based on which the N-doped CDs were successfully applied as a fluorescence probe for cell imaging. Moreover, it was then successfully demonstrated for sensitive and selective detection of Fe^{3+} in serum.

1. Introduction

During the past few years, fluorescent CDs have attracted tremendous attention due to their unique optical and electronic properties [1–6]. Compared to conventional semiconductor quantum dots and organic fluorescent dyes, CDs possess several superior features including functionalization, low toxicity, excellent water dispersibility, tunable fluorescence emission, excellent photostability, upconversion, and biocompatibility, thus demonstrating potential application in the fields of bioimaging, in vivo theranostics, drug delivery, light-emitting diodes, photocatalysis solar cells, and heavy metal ion detection [7–11]. In addition, doping CDs with other nonmetallic components, such as N, S, and P, can inject electrons into carbon-based materials and change the electronic transport properties and PL properties [12, 13]. However, in most cases, the QY of the as-synthesized CD was less than 10%, and the QY is a key parameter to evaluate the quality of CDs, which limit the sensitivity and selectivity. So, synthesis of high-fluorescence carbon quantum dots is the direction of development.

The use of N-containing precursors has proved to be an effective route for obtaining N-doped CDs. Chen et al. [14] used 2-azidoimidazole as precursor in a hydrothermal

process at 70°C overnight to obtain nitrogen-rich CDs. Lv et al. [15] using ethanediamine and citric acid as precursors obtained N-doped CDs and achieved good results in iron detection. Wang and Zhou. [16] used milk to prepare N-CDs hydrothermally at 180°C for 2 h. In another study, Hsu and Chang [17] found that compounds containing both amino and carboxyl groups are beneficial for synthesizing CDs with high PL quantum yield. Based on the benefits of N-doping in carbon nanostructures, it can be extrapolated that the introduction of N to carbon dots would further enhance their versatile properties. However, most N-doped CDs are unsatisfactory due to harsh synthetic conditions and long reaction times. Thus, a time-saving and eco-friendly synthesis of N-doped CDs is of interest.

Herein, a facile, green, and high-output thermal strategy is proposed for the fabrication of highly fluorescent N-doped CDs. We used L-citrulline as the precursor for a facile and eco-friendly one-step hydrothermal method without the assistance of any chemicals (except pure water) to obtain highly fluorescent N-doped CDs. The as-prepared N-doped CDs exhibit good water solubility, good biocompatibility, and high fluorescence quantum yield (32.9%). Owing to the unique properties of the N-doped CD nanoprobe with good membrane permeability and excellent biocompatibility, it

was used for imaging of HeLa cells with high discrimination. Moreover, it was further applied for detection of Fe^{3+} ions in serum, and the fluorescence intensity exhibited a good linear relationship in the Fe^{3+} concentration range from 0 to $50 \mu\text{M}$ with a detection limit of about 37 nM.

2. Experimental

2.1. Materials. L-citrulline (98%) and quinine sulphate (98%) were purchased from J&K Scientific Inc. (Beijing, China). 3-(4,5-Dimethylthiazol-2-yl)-2, 5-diphenyltetrazolium bromide (MTT, 98%) was obtained from Sangon Biotechnology Inc. (Shanghai, China). Dimethyl sulphoxide (DMSO) was obtained from Xilong Reagents Company (Guangdong, China). Penicillin-streptomycin, Dulbecco's modified Eagle's medium (DMEM), and foetal bovine serum (FBS) were purchased from Solarbio (Beijing, China). NaCl, KCl, MgCl_2 , AlCl_3 , CaCl_2 , $\text{Cr}(\text{NO}_3)_3$, FeCl_2 , FeCl_3 , $\text{Co}(\text{NO}_3)_2$, CuSO_4 , ZnCl_2 , $\text{Cd}(\text{NO}_3)_2$, SrCl_2 , and $\text{Hg}(\text{NO}_3)_2$ were purchased from Aladdin (Shanghai, China). HeLa cell lines were obtained from Cellcook. Human serum samples were provided by Xing Ying People's Hospital Blood Center (Xingyi, China). Ultrapure water (18.2 M Ω , Millipore Co., USA) was used in all experiments. Other chemical reagents (analytical grade) were purchased from Beijing Chemical Company (Beijing, China).

2.2. Instrumentation and Characterization. The morphologies and sizes of N-doped CDs were characterized by high-resolution transmission electron microscopy (HRTEM, Hitachi-F20) at an accelerating voltage of 200 kV and atomic force microscopy (AMF, Bruker Multimode 8) in the tapping mode. Fourier transform infrared (FT-IR) spectra were obtained on a Nicolet 6700 FT-IR spectrometer using KBr pellets. X-ray photoelectron spectroscopy (XPS) was performed using an ESCALAB 250Xi (Thermo Scientific). X-ray diffraction (XRD) was carried out using a Rigaku diffractometer in the 2θ range 10–80° with step width of 0.02°. UV-Vis absorption spectra were recorded on a DU 800 UV-Vis spectrophotometer. The PL decay curves were obtained on a Leica SP5 FLIM system using a 405 nm laser excitation source. Fluorescence spectroscopy and stability were measured on a PerkinElmer LS 55 with 5/5 nm slit width and equipped with a 1 cm quartz cell. A TGL-20LM-B high-speed refrigerated centrifuge (Hunan Xingke Instrument Co., Ltd., China) was used to purify the N-doped CDs. Cell imaging was carried out using a Leica SP8 confocal laser scanning microscope (Leica, Germany).

2.3. Synthesis of N-Doped CDs. N-doped CDs were synthesized by a facile hydrothermal method. Briefly, 0.50 g-L-citrulline was dissolved in 25 mL ultrapure water and subjected to ultrasonic oscillation for 20 min. The solution was transferred to a Teflon-equipped stainless steel autoclave and reacted at 220°C for 12 h. After the reaction liquid was cooled to room temperature, the reaction liquid was centrifuged at 17,000 rpm for 40 min to separate aggregated particles. The supernatant fluid was removed by filtration with a 0.22 μm filter membrane. The as-prepared N-doped CD solution was stored at 4°C for further use.

2.4. MTT Assay and Intracellular Fluorescence Imaging. Cytotoxicity of the N-doped CDs was investigated with the cancer cell line HeLa by an MTT assay. HeLa cells were seeded in a 96-well plate at a density of 4×10^3 cells per well for 24 h in an incubator (37°C, 5% CO_2). The culture medium was replaced with 100 μL fresh DMEM containing the N-doped CDs at concentrations of 0, 25, 50, 100, 250, and 500 $\mu\text{g}/\text{mL}$ and incubated in an incubator (37°C, 5% CO_2). After 24 or 48 h, 20 μL MTT (5 mg/mL) solution was added to each cell well, which was incubated for 4 h. Subsequently, the culture medium with MTT was removed and 100 μL DMSO was added, followed by shaking for 10 min. The optical density (OD) of each well at 490 nm was measured on the enzyme-linked immunosorbent detector.

HeLa cells (1×10^5 cells/dish) were seeded in a confocal dish with 100 μL fresh DMEM containing 10% FBS and incubated in an incubator (37°C, 5% CO_2). After 24 h, the N-doped CDs with concentrations of 50, 200, 400, and 600 $\mu\text{g}/\text{mL}$ were added to the confocal dish and incubated at 37°C in 5% CO_2 for another 4 h. Subsequently, the adherent cells were carefully washed three times with PBS (0.01 M, pH 7.4). Finally, the laser confocal microscopy imaging of HeLa cells was performed at excitations of 405 and 488 nm. Bright-field images were captured to ensure the locations of fluorescent tag signals.

2.5. Metal Ion Detection by N-Doped CDs. Sources of various metal ions such as Na^+ , Mg^{2+} , Al^{3+} , Ca^{2+} , Cr^{3+} , Fe^{2+} , Fe^{3+} , Co^{2+} , Cu^{2+} , Zn^{2+} , Cd^{2+} , Sr^{2+} , K^+ , and Hg^{2+} were applied for detection. N-doped CD stock solution (2.0 mg/mL, 250 μL) was mixed with 50 μL of 120 μM solutions of different metal ions to reach the final concentration of 20 μM , respectively. Afterward, the mixtures were recorded under excitation at 360 nm. To evaluate the selectivity of this N-doped CD toward Fe^{3+} , interference assays were performed under identical conditions using above ions and Fe^{3+} , and the N-doped CD stock solution was added to different concentrations of Fe^{3+} solution in a similar manner.

3. Results and Discussion

3.1. Characterization of N-Doped CDs. The size and morphology of N-doped CDs were characterized by HRTEM and AFM. The TEM image (Figure 1(a)) clearly revealed N-doped CDs with spherical morphology, average diameter (inset in Figure 1(a)) of 2.7 nm, and a narrow particle size distribution of 2.3–3.3 nm. HRTEM images (Figure 1(b)) showed that the average lattice spacing of the N-doped CDs was 0.32 nm, in agreement with the (002) diffraction planes of graphite [18, 19]. The AFM 3D image and topography image (Figures 2(a) and 2(b)) indicate that the N-doped CDs had a spherical shape, which is consistent with the TEM results. The average height (Figure 2(c)) of N-doped CDs was 3.16 nm, which is close to the diameter of N-doped CDs measured by TEM (2.68 nm). Hence, in accordance with the previous reports, the N-doped CDs were almost spherical carbon nanoparticles [20, 21]. FT-IR spectroscopy and XPS analyses were performed to study the

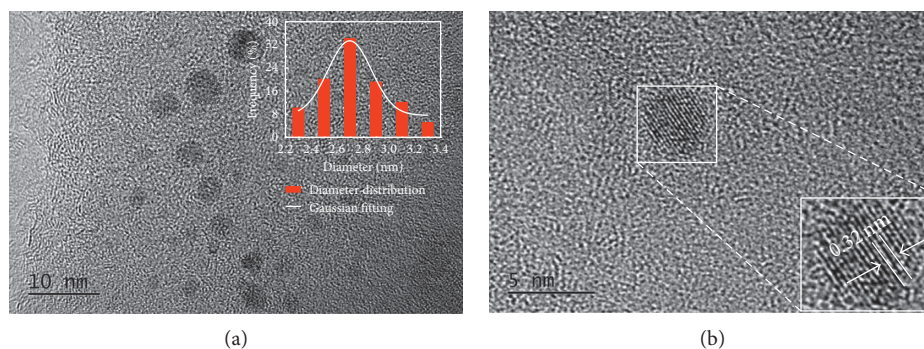


FIGURE 1: (a) TEM image of N-doped CDs. Inset shows the size distribution of N-doped CDs. (b) HRTEM reveals lattice spacing of N-doped CDs.

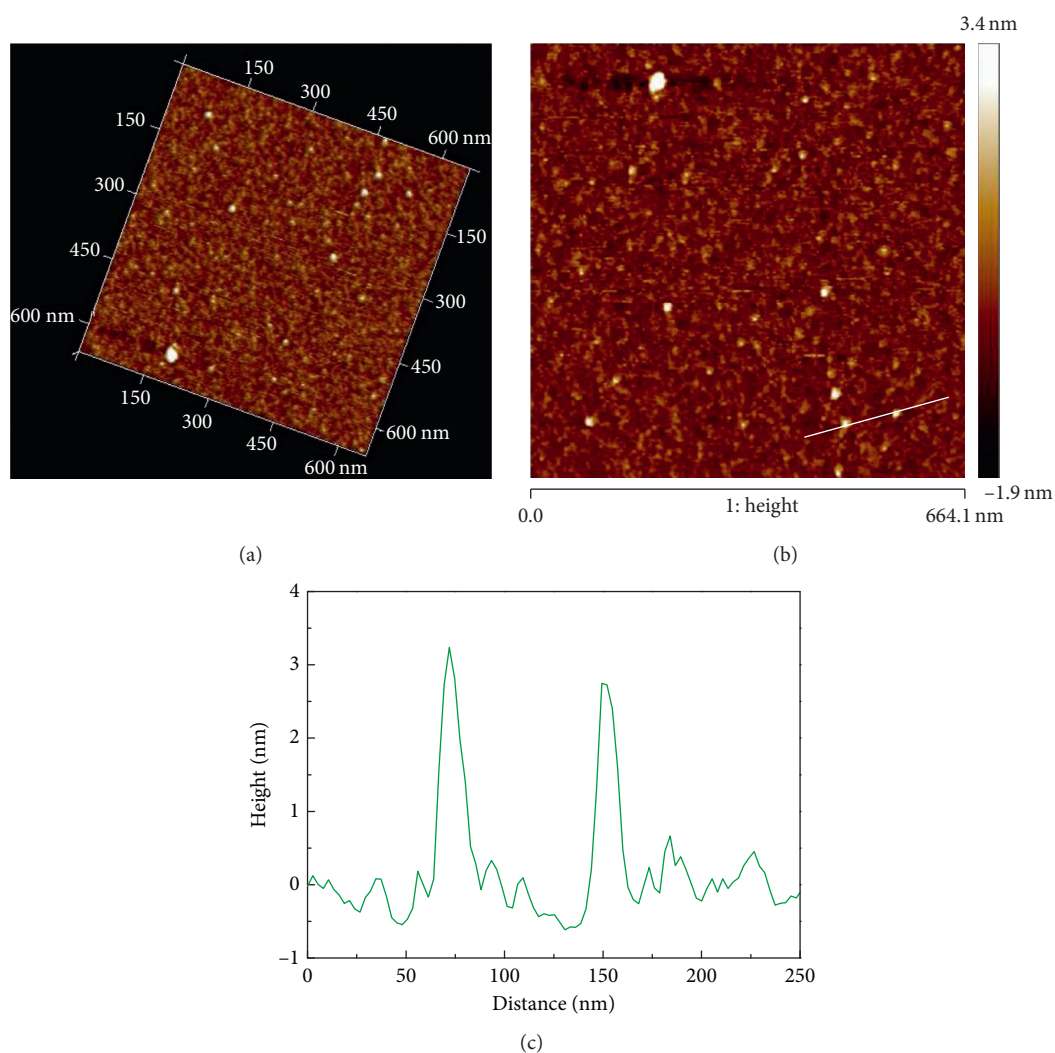


FIGURE 2: AMF images of N-doped CDs. (a) AMF 3D image, (b) AMF topography image, and (c) height profile along the line in (b).

chemical composition and functional groups of the N-doped CDs. In the FT-IR spectrum in Figure 3(a), the peak at 3433 cm^{-1} is attributed to the stretching vibration of -NH , the peaks at 1625 cm^{-1} indicate the existence of C=C , the peak at 1408 cm^{-1} was assigned to the bending vibration of C-NH (indicating the successful adulteration of nitrogen atoms into the C-dots), and the absorption at

674 cm^{-1} is ascribed to C-H . These FT-IR assignments were further verified by XPS analysis. XPS was used to measure the surface chemical composition and elemental analysis of N-doped CDs. The three main peaks at 284.78, 400.48, and 530.38 eV of the XPS survey spectrum (shown in Figure 3(b)) correspond to C1s , N1s , and O1s , respectively. The N-doped CDs contained 54.5 at.% carbon, 19.2 at. % nitrogen, and 26.3

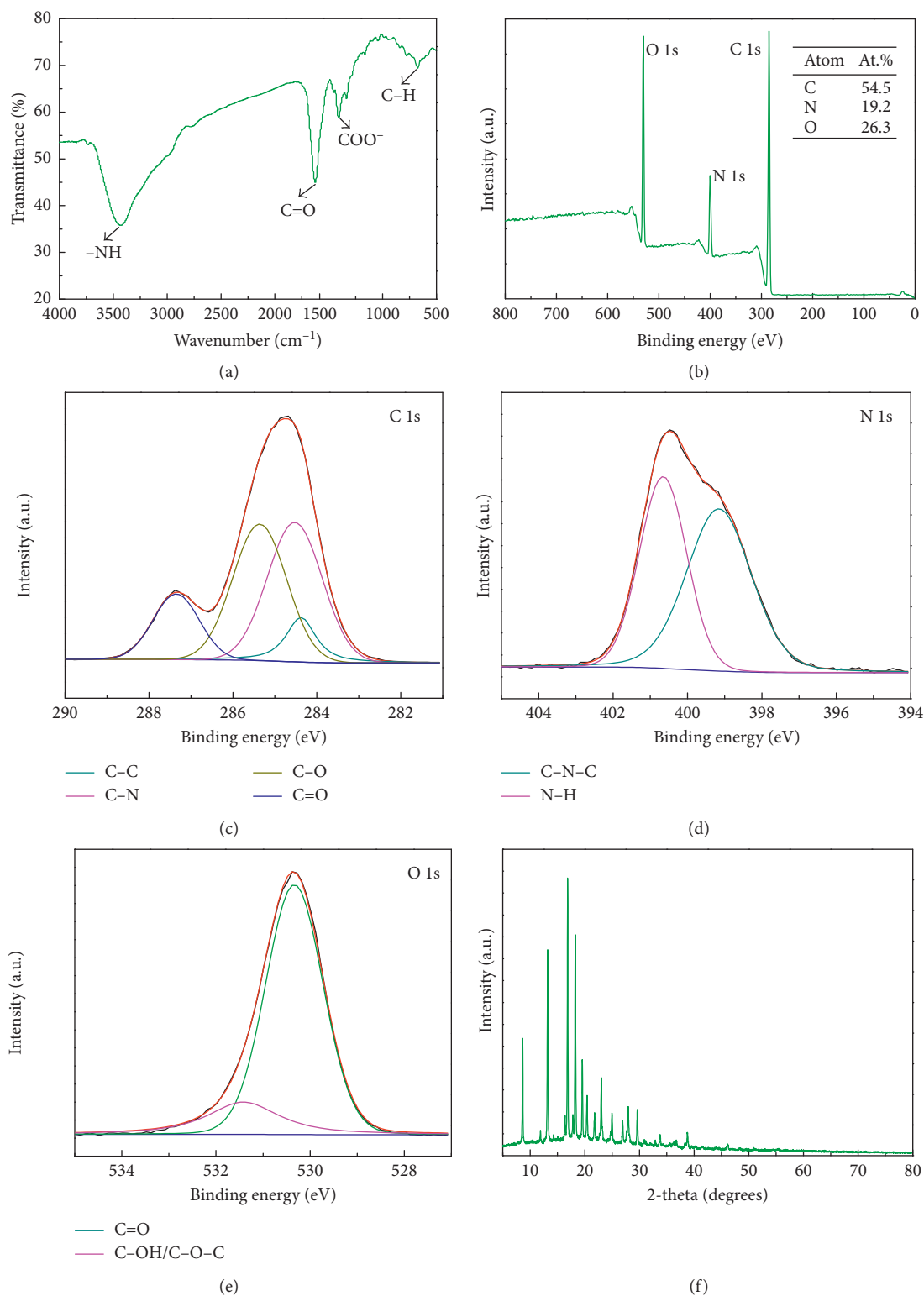


FIGURE 3: (a) FT-IR spectra of N-doped CDs. (b) XPS survey spectrum of N-doped CDs and high-resolution spectra of C1s (c), N1s (d), and O1s (e). (f) XRD pattern of N-doped CDs.

at. % oxygen at the corresponding binding energies given in Figure 3(b). High-resolution XPS spectra of C1s (Figure 3(c)) can be ascribed to four component peaks with binding energies of about 284.38, 284.48, 285.38, and 287.38 eV. Here,

the anterior peak located at 284.38 eV reflects the bonding structure of C-C (sp^3) bonds, the peak located at 284.48 eV reflects the bonding structure of the C-N (sp^3) bonds, and the peaks at 285.38 and 287.38 eV are attributed to the C-O (sp^2)

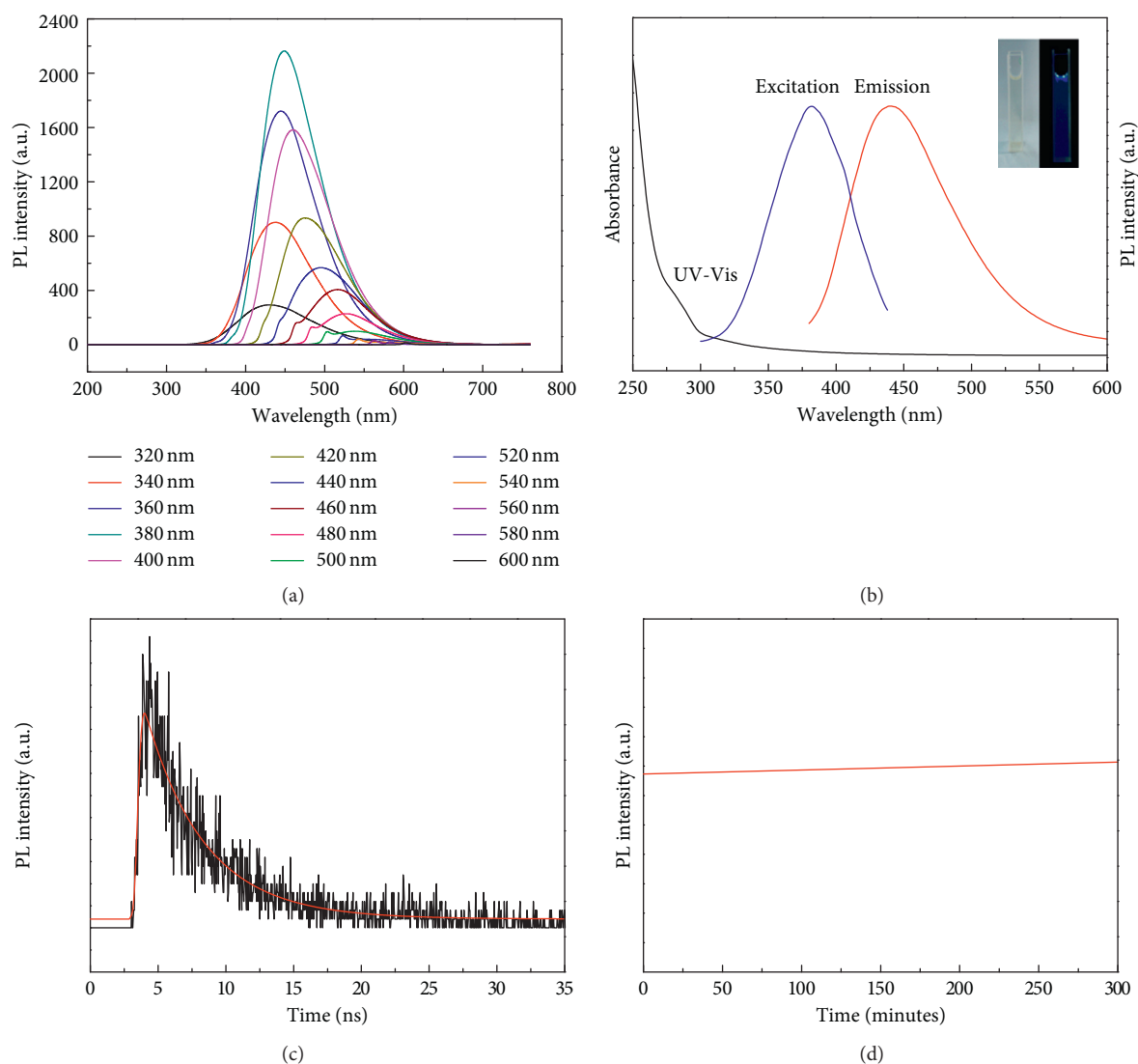


FIGURE 4: (a) UV-Vis absorption spectrum (black line), fluorescence excitation (red line, $\lambda_{em} = 438$ nm), and emission spectra (blue line, $\lambda_{ex} = 377$ nm) of N-doped CDs. The insets show the photograph (left) and fluorescence image of N-doped CD solution under 365 nm UV light (right). (b) Fluorescence emission spectra of the N-doped CDs. (c) The fluorescence decay curve of N-doped CDs. (d) Fluorescence stability of N-doped CDs.

and C=O (sp^2) bonds, respectively [22]. This indicated that the as-prepared N-doped CDs were rich in hydrophilic groups on their surfaces, which was consistent with the corresponding FT-IR spectrum. As shown in Figure 3(d) (partial XPS spectrum of N1s), the N1s peak can also be resolved into two components centred at 399.18 and 400.48 eV; the anterior peak located at 399.18 eV reflects the bonding structure of C–N–C bonds, and the second peak located at 400.48 eV reflects the bonding structure of the N–H bonds [23, 24]. The O1s peak had two components at 530.38 and 531.38 eV for adsorbed oxygen: C=O and C–OH/C–O–C (Figure 3(e)), respectively [21]. Surface functionality analyses via XPS are in agreement with FT-IR results. The above analysis indicated that the N-doped CDs synthesized might have functional groups like –COOH, –OH, and –NH. XRD patterns (Figure 3 (f)) showed many narrow 2θ diffraction peaks at about 8.65° , 11.91° , 13.21° , 16.39° , 16.86° , 17.82° , 18.27° , 19.55° , 20.41° ,

21.79° , 23.02° , 24.73° , 24.97° , 26.93° , 27.97° , 29.62° , 33.76° , and 38.75° , suggesting ordered carbon in N-doped CDs.

3.2. Spectral Properties and Cytotoxicity Assay of N-Doped CDs. As displayed in Figure 4(a), the excellent optical properties of the synthesized N-doped CDs were demonstrated by absorption and PL spectroscopy. The N-doped CDs displayed broad UV-Vis absorption, which was attributed to the $n-\pi^*$ transition in N-doped CDs. The emission wavelength of N-doped C-dots was red-shifted from 430 to 600 nm with excitation wavelength ranging from 320 to 600 nm [25]. In addition, the optimal excitation and emission wavelengths of the N-doped CDs solution were located at 377 and 438 nm (Figure 4(b)). Separately, the N-doped CD aqueous solution emitted strong blue light upon ultraviolet excitation at 365 nm (right inset, Figure 4(b)).

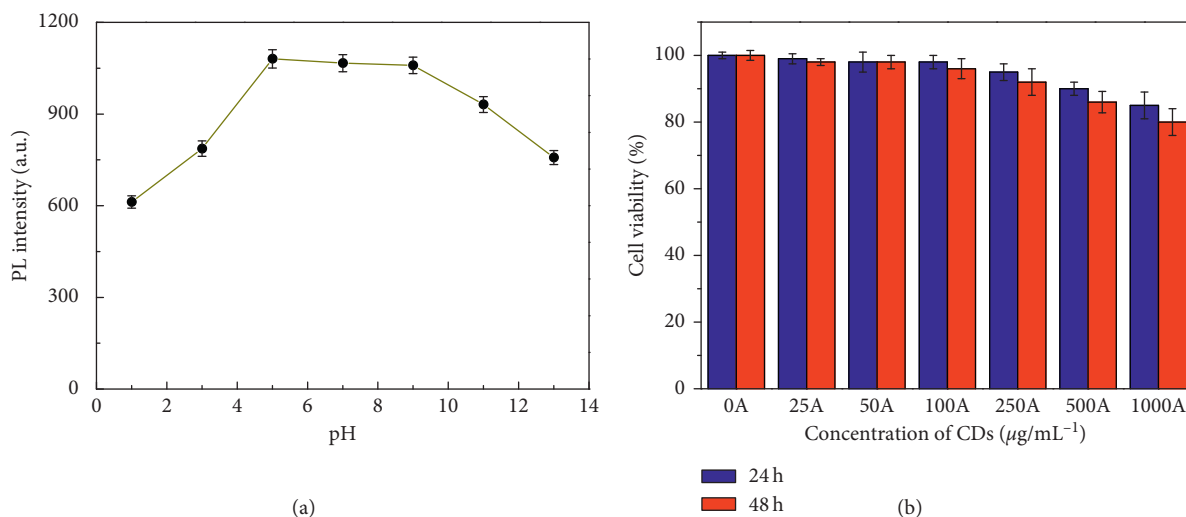


FIGURE 5: (a) PL spectra of N-doped CD aqueous solutions at different pH ($\lambda_{\text{ex}} = 365 \text{ nm}$). (b) Cytotoxicity testing results via an MTT assay.

To further investigate the optical properties of the as-obtained N-doped CDs, the PL excitation spectrum of the N-doped CDs was observed (Figure 4(b)). The spectrum displayed typical excitation wavelength dependence, and the emission wavelength was red-shifted when excited with longer wavelengths. This behaviour of the N-doped CDs has been suggested to be a result of different sizes or the existence of different emissive sites on the surfaces [26]. This excitation-dependent emission property of carbon dots has also been found in the previous reports [27–29]. We further investigated the fluorescence stability of N-doped CDs. Time-correlated single-photon counting (TCSPC) was applied to measure the fluorescence lifetime of the N-doped CDs. As presented in Figure 4(c), the decay lifetime of the N-doped CDs was measured with the previous reports [30], and the calculated average fluorescence lifetime for the N-doped CDs was $4.45 \pm 0.05 \text{ ns}$. Moreover, the photostability (Figure 4(d)) of the N-doped CDs synthesized was tested upon continuous excitation at 360 nm for 5 h; the fluorescence remained intact without any photobleaching, which corroborates to reasonably good photostability of N-doped CDs.

To investigate the applicability of N-doped CDs as a fluorescence biomarker in a practical biological environment, the fluorescence stability of N-doped CD aqueous solution was evaluated. As revealed in Figure 5(a), with increase in pH from 3.0 to 5.0, the fluorescence intensity reached a peak and decreased with pH ranging from 5.0 to 13.0. The original solution pH of the N-doped CDs was approximately 9.0. The figure shows that the fluorescence intensity of the N-doped CDs at pH 7.0–9.0 was stronger than that at 9.0 and the fluorescence intensity had not clearly declined at 7.0–9.0. A physiological environment generally has pH of 7.0–8.0, which is beneficial for bioimaging applications. In addition, fluorescence QY of the N-doped CDs was found using quinine sulphate as standard (measured at 350 nm excitation wavelength, QY = 54%). The average QY of N-doped CDs in aqueous solution at room temperature was 32.9%. The high QY is possibly due to the existence of nitrogen-containing

functional groups, which are generally excellent auxochromes and greatly enhance photoluminescence.

The biological application of N-doped CDs was also explored. MTT assays were carried out to evaluate the cytotoxicity of the as-prepared N-doped CDs to living cells. As expected, cell viabilities were estimated to be greater than 90% upon addition of N-doped CDs over a wide concentration range (0–500 $\mu\text{g/mL}$) and after incubation for 48 h (Figure 5(b)). High cell viabilities confirmed the low toxicity, excellent biocompatibility, and great potential of the as-prepared N-doped CDs for imaging in living cells. These also indicate that the as-prepared N-doped CDs can be considered safe for in vitro and in vivo applications.

3.3. Application of N-Doped CDs

3.3.1. Imaging of HeLa Cells. Based on these fluorescence properties, experiments were carried out to further demonstrate the availability of the as-prepared N-doped CDs for imaging in cells and plants. Figure 6 shows CLSM images under bright field, 405 nm, 458 nm, and 514 nm excitations of HeLa cells incubated for 4 h at 37°C with 50, 200, 400, and 600 $\mu\text{g}\cdot\text{mL}^{-1}$ N-doped CDs. As shown in the figure, strong blue and green fluorescence of the HeLa cells can be seen at 405 and 488 nm. More careful observation revealed that the luminescence spots appeared widely in the membrane and cytoplasmic areas of the HeLa cells. In addition, with the increase in the concentration of N-doped CDs, the fluorescence enhancement helped identify tumour cells. According to the previous studies, the cytoplasm-specific property of N-doped CDs should be related to endocytosis [1, 9, 14, 21]. The results indicated that N-doped CDs could be used for in vitro tumour cell labelling via a simple incubation method.

3.3.2. Selectivity and Ratiometric Detection of Fe^{3+} in Serum. As shown in Figure 7(a), under the same conditions, in sharp contrast to Fe^{3+} , other ions including Hg^{2+} , Cr^{3+} , Fe^{2+} , Co^{2+} ,

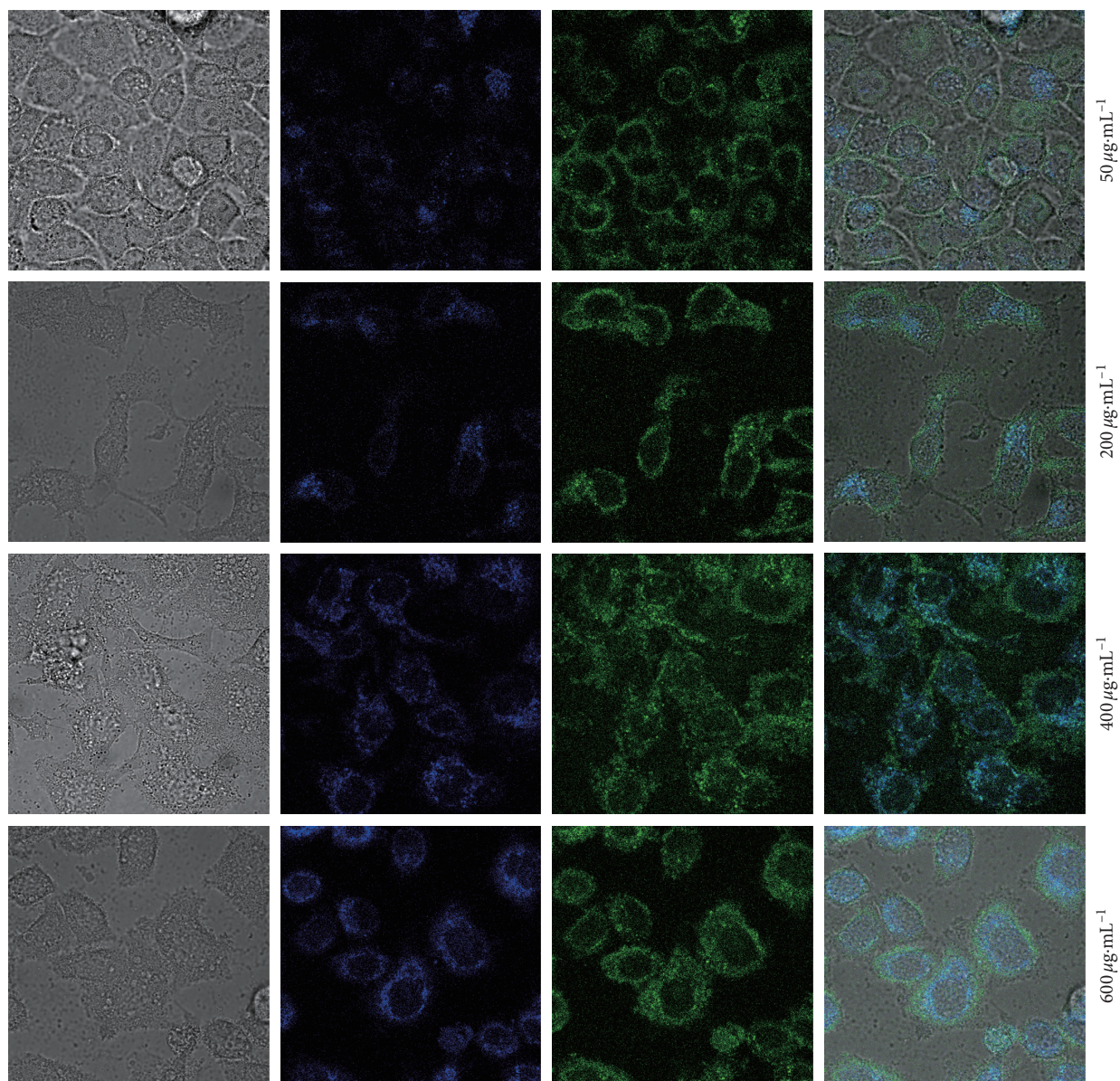


FIGURE 6: Laser scanning confocal microscopy images of HeLa cells with different concentrations of N-doped CDs.

Cd^{2+} , Sr^{2+} , Al^{3+} , Mg^{2+} , Zn^{2+} , Ca^{2+} , K^{+} , Na^{+} , and Cu^{2+} showed almost no influence on the spectra of the nanoprobe. The fluorescence could be quenched by Fe^{3+} ion due to the special coordination interaction between Fe^{3+} ion and the hydroxy groups on the surface of CDs, which may contribute to nonradiative electron transfer that involves partial transfer of an electron in the excited state to the d orbital of Fe^{3+} . To further investigate the FL quenching mechanism of N-doped CDs, different concentrations of Fe^{3+} solution were added to N-doped CD stock solution. As shown in Figure 7(b), the FL intensity of N-doped CDs gradually decreased with increasing Fe^{3+} concentration and the inset shows the relationship of the relative fluorescence intensity F/F_0 with Fe^{3+} concentration. Dynamic fluorescence quenching is described by the Stern–Volmer equation [31]. The inset in Figure 6(b) shows a linear relationship ($R^2=0.998$) in the range of Fe^{3+} concentration from 0 to $50\ \mu\text{M}$. The detection

limit was $37\ \text{nM}$ (signal-to-noise ratio of 3). The results demonstrated that N-doped CDs show promise as a sensitive and selective probe for the detection of Fe^{3+} . In order to demonstrate the analytical performance of the proposed N-doped CDs in complicated biological samples, the capability of the N-doped CDs was evaluated by quantitative detection of Fe^{3+} in human serum, and it was spiked with different concentrations of Fe^{3+} and measured by the proposed method. Table 1 shows that the recoveries were 95.2–112% with the relative standard deviation (RSD, $n=5$) less than 5.8%, which indicates that the proposed method was sensitive and accurate.

4. Conclusions

We demonstrated a facile and green synthesis method to prepare novel fluorescent N-doped CDs by hydrothermal reaction using amino acid L-citrulline as precursor.

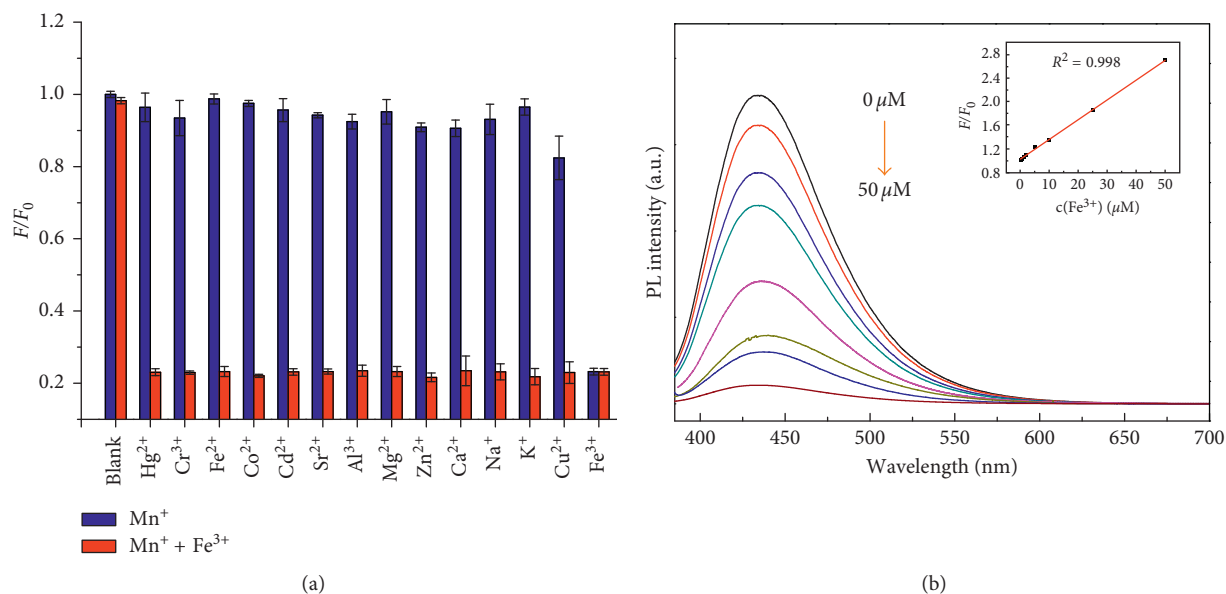


FIGURE 7: Ion detection of N-doped CDs. (a) Fluorescence recovery efficiency F/F_0 response of the N-doped CDs toward Fe^{3+} and other interference. (b) PL spectra of N-doped CDs with different Fe^{3+} concentrations (0 to 50 μM). Inset: the dependence of F/F_0 on concentration (0 to 50 μM).

TABLE 1: Determination of iron in human serum using N-doped CDs.

Samples	Added ($\mu mol/L$)	Found ($\mu mol/L$)	Recovery (%)	RSD% ($n = 5$)
Serum	0.250	0.281	112	5.8
	2.50	2.61	104	4.6
	25.0	23.8	95.2	3.9

The N-doped CD aqueous solution emitted strong blue light under UV irradiation with a fluorescence quantum yield of 32.9%, and the emission wavelength was red-shifted under excitation with longer wavelengths. The fluorescent N-doped CDs acted as novel fluorescence probes that facilitated simultaneous imaging of HeLa cells and sensitivity detection of Fe^{3+} ions. The N-doped CDs showed outstanding overall performance such as outstanding optical properties, good chemical and photochemical stability, inertness to interference of metal ions and biomolecular species, and excellent biocompatibility, which make N-doped CDs a desirable alternative probe for biological imaging, detection, and many other applications.

Data Availability

The data used to support the findings of this study are included within the article, and any further information is available from the corresponding author upon request.

Conflicts of Interest

The authors declare that there are no conflicts of interest regarding the publication of this paper.

Acknowledgments

This work was supported by the National Natural Science Foundation of China (no. 21505115), the Science and

Technology Foundation of the Guizhou Province, Science and Technology Department (nos. LH20147406 and LH20167034), the Natural Science Foundation of the Guizhou Province, Education Department (no. KY(2017)368), the Social Development Foundation of the Science and Technology Bureau of Qianxinan Prefecture (no. 2016-1-29), and the Ph.D. Programs Foundation of Xingyi Normal University for Nationalities (no. 16XYBS20).

References

- [1] Y. W. Zheng, D. Yang, X. Wu et al., "A facile approach for the synthesis of highly luminescent carbon dots using vitamin-based small organic molecules with benzene ring structure as precursors," *RSC Advances*, vol. 5, no. 110, pp. 90245–90254, 2015.
- [2] V. Georgakilas, J. A. Perman, J. Tucek, and R. Zboril, "Broad family of carbon nanoallotropes: classification, chemistry, and applications of fullerenes, carbon dots, nanotubes, graphene, nanodiamonds, and combined superstructures," *Chemical Reviews*, vol. 115, no. 11, pp. 4744–4822, 2015.
- [3] M. J. Meziani, X. L. Dong, L. Zhu et al., "Visible-light-activated bactericidal functions of carbon "quantum" dots," *ACS Applied Materials and Interfaces*, vol. 8, no. 17, pp. 10761–10766, 2016.
- [4] S. Mandani, D. Dey, B. Sharma, and T. K. Sarma, "Natural occurrence of fluorescent carbon dots in honey," *Carbon*, vol. 119, no. 9, pp. 569–572, 2017.
- [5] S. Li, Z. Guo, Y. Zhang, W. Xue, and Z. H. Liu, "Blood compatibility evaluations of fluorescent carbon dots," *ACS*

- Applied Materials and Interfaces*, vol. 7, no. 34, pp. 19153–19162, 2015.
- [6] H. Ding, S. B. Yu, J. S. Wei, and H. M. Xiong, “Full-color light-emitting carbon dots with a surface-state-controlled luminescence mechanism,” *ACS Nano*, vol. 10, no. 1, pp. 484–491, 2016.
- [7] H. Li, W. Q. Kong, J. Liu et al., “Fluorescent N-doped carbon dots for both cellular imaging and highly-sensitive catechol detection,” *Carbon*, vol. 91, no. 11, pp. 66–475, 2015.
- [8] L. Liu, L. Chen, J. G. Liang, L. Z. Liu, and H. Y. Han, “A novel ratiometric probe based on nitrogen-doped carbon dots and rhodamine b isothiocyanate for detection of Fe³⁺ in aqueous solution,” *Journal of Analytical Methods in Chemistry*, vol. 2016, Article ID 4939582, 7 pages, 2016.
- [9] S. Y. Lim, W. Shen, and Z. Q. Gao, “Carbon quantum dots and their applications,” *Chemical Society Reviews*, vol. 44, no. 1, pp. 362–381, 2015.
- [10] Y. B. Song, S. J. Zhu, S. Y. Xiang et al., “Investigation into the fluorescence quenching behaviors and applications of carbon dots,” *Nanoscale*, vol. 6, no. 9, pp. 4676–4682, 2014.
- [11] J. J. Zhao, M. J. Huang, L. L. Zhang et al., “A unique approach to develop carbon dot-based nanohybrid near-infrared ratiometric fluorescent sensor for the detection of mercury ions,” *Analytical Chemistry*, vol. 89, no. 15, pp. 8044–8049, 2017.
- [12] K. Jiang, S. Sun, L. Zhang, Y. H. Wang, C. Z. Cai, and H. W. Lin, “Bright-yellow-emissive N-doped carbon dots: preparation, cellular imaging, and bifunctional sensing,” *ACS Applied Materials and Interfaces*, vol. 7, no. 41, pp. 23231–23238, 2015.
- [13] X. J. Gong, W. J. Lu, Y. Liu et al., “Low temperature synthesis of phosphorous and nitrogen co-doped yellow fluorescent carbon dots for sensors and bioimaging,” *Journal of Materials Chemistry B*, vol. 3, no. 33, pp. 6813–6819, 2015.
- [14] X. X. Chen, Q. Q. Jin, L. Z. Wu, C. H. Tung, and X. J. Tang, “Synthesis and unique photoluminescence properties of nitrogen-rich quantum dots and their applications,” *Angewandte Chemie International Edition*, vol. 53, no. 51, pp. 14447–14450, 2014.
- [15] P. F. Lv, Y. X. Yao, H. M. Zhou et al., “Synthesis of novel nitrogen-doped carbon dots for highly selective detection of iron ion,” *Nanotechnology*, vol. 28, no. 12, pp. 165502–165511, 2017.
- [16] L. Wang and H. S. Zhou, “Green synthesis of luminescent nitrogen-doped carbon dots from milk and its imaging application,” *Analytical Chemistry*, vol. 86, no. 15, pp. 8902–8905, 2014.
- [17] P. C. Hsu and H. T. Chang, “Synthesis of high-quality carbon nanodots from hydrophilic compounds: role of functional groups,” *Chemical Communications*, vol. 48, no. 33, pp. 3984–3986, 2012.
- [18] Z. H. Kang, E. B. Wang, B. D. Mao et al., “Controllable fabrication of carbon nanotube and nanobelt with a polyoxometalate-assisted mild hydrothermal process,” *Journal of the American Chemical Society*, vol. 127, no. 18, pp. 6534–6535, 2005.
- [19] J. Lu, J. X. Yang, J. Z. Wang, A. L. Lim, S. Wang, and K. P. Loh, “One-pot synthesis of fluorescent carbon nanoribbons, nanoparticles, and graphene by the exfoliation of graphite in ionic liquids,” *ACS Nano*, vol. 3, no. 8, pp. 2367–2375, 2009.
- [20] N. Li, A. Than, C. C. Sun et al., “Monitoring dynamic cellular redox homeostasis using fluorescence-switchable graphene quantum dots,” *ACS Nano*, vol. 10, no. 12, pp. 11475–11482, 2016.
- [21] L. Yang, W. H. Jiang, L. P. Qiu et al., “One pot synthesis of high quantum yield of polyethylene glycol anchored carbon dots and functionalized with nuclear localization signal peptide for cell nucleus imaging,” *Nanoscale*, vol. 7, no. 14, pp. 6104–6113, 2015.
- [22] X. Q. Niu, G. S. Liu, L. Y. Li, Z. Fu, H. Xu, and F. L. Cui, “Green and economical synthesis of nitrogen-doped carbon dots from vegetables for sensing and imaging applications,” *RSC Advances*, vol. 5, no. 115, pp. 95223–95229, 2015.
- [23] J. Ju and W. Chen, “Synthesis of highly fluorescent nitrogen-doped graphene quantum dots for sensitive, label-free detection of Fe (III) in aqueous media,” *Biosensors and Bioelectronics*, vol. 58, no. 8, pp. 219–225, 2014.
- [24] X. W. Dong, Y. J. Su, H. J. Geng et al., “Fast one-step synthesis of N-doped carbon dots by pyrolyzing ethanolamine,” *Journal of Materials Chemistry C*, vol. 2, no. 36, pp. 7477–7481, 2014.
- [25] H. J. Zhang, Y. L. Chen, M. J. Liang et al., “Solid-phase synthesis of highly fluorescent nitrogen-doped carbon dots for sensitive and selective probing ferric ions in living cells,” *Analytical Chemistry*, vol. 86, no. 19, pp. 9846–9852, 2014.
- [26] Y. Q. Dong, H. C. Pang, H. B. Yang et al., “Carbon-based dots co-doped with nitrogen and sulfur for high quantum yield and excitation-independent emission,” *Angewandte Chemie International Edition*, vol. 52, no. 30, pp. 7800–7804, 2013.
- [27] L. Y. Zhang, D. H. Wang, H. W. Huang et al., “Preparation of gold-carbon dots and ratiometric fluorescence cellular imaging,” *ACS Applied Materials and Interfaces*, vol. 8, no. 10, pp. 6646–6655, 2016.
- [28] A. M. Alam, B. Y. Park, Z. K. Ghouri, M. Park, and H. Y. Kim, “Synthesis of carbon quantum dots from cabbage with down- and up-conversion photoluminescence properties: excellent imaging agent for biomedical applications,” *Green Chemistry*, vol. 17, no. 7, pp. 3791–3797, 2015.
- [29] J. Hou, J. Yan, Q. Zhao, Y. Li, H. Ding, and L. Ding, “A novel one-pot route for large-scale preparation of highly photoluminescent carbon quantum dots powders,” *Nanoscale*, vol. 5, no. 20, pp. 9558–9561, 2013.
- [30] J. C. Shen, Q. Li, Y. Zhang, X. J. She, C. F. Wang, and S. Chen, “Nitrogen-doped carbon dots derived from polyamindamine dendrimer,” *RSC Advances*, vol. 6, no. 64, pp. 59702–59707, 2016.
- [31] S. Mohapatra, S. Sahu, N. Sinha, and S. K. Bhutia, “Synthesis of carbon dot based photoluminescent probe for selective and ultrasensitive detection of Hg²⁺ in water and living cells,” *Analyst*, vol. 140, no. 4, pp. 1221–1228, 2015.

Research Article

A Simple Separation Method of the Protein and Polystyrene Bead-Labeled Protein for Enhancing the Performance of Fluorescent Sensor

Hye Jin Kim,¹ Dong-Hoon Kang,² Seung-Hoon Yang,³ Eunji Lee,⁴ Taewon Ha,⁵ Byung Chul Lee,⁶ Youngbaek Kim,⁵ Kyo Seon Hwang,¹ Hyun-Joon Shin,² and Jinsik Kim ⁴

¹Department of Clinical Pharmacology, Kyung Hee University, Seoul 02447, Republic of Korea

²Center for Bionics, Korea Institute of Science and Technology, Seoul 02792, Republic of Korea

³Systems Biotechnology Research Center, Korea Institute of Science and Technology, Gangneung 25451, Republic of Korea

⁴Department of Medical Biotechnology, Dongguk University, Seoul 04620, Republic of Korea

⁵Center for Nano-Photonics Convergence Technology, Korea Institute of Industrial Technology (KITECH), Gwangju 61012, Republic of Korea

⁶Center for BioMicrosystems, Korea Institute of Science and Technology (KIST), Seoul 02792, Republic of Korea

Correspondence should be addressed to Jinsik Kim; lookup2@dongguk.edu

Received 23 March 2018; Revised 31 May 2018; Accepted 7 June 2018; Published 11 July 2018

Academic Editor: Subhankar Singha

Copyright © 2018 Hye Jin Kim et al. This is an open access article distributed under the Creative Commons Attribution License, which permits unrestricted use, distribution, and reproduction in any medium, provided the original work is properly cited.

Dielectrophoresis- (DEP-) based separation method between a protein, amyloid beta 42, and polystyrene (PS) beads in different microholes was demonstrated for enhancement of performance for bead-based fluorescent sensor. An intensity of $\nabla|E|^2$ was relative to a diameter of a microhole, and the diameters of two microholes for separation between the protein and PS beads were simulated to $3\ \mu\text{m}$ and $15\ \mu\text{m}$, respectively. The microholes were fabricated by microelectromechanical systems (MEMS). The separation between the protein and the PS beads was demonstrated by comparing the average intensity of fluorescence (AIF) by each molecule. Relative AIF was measured in various applying voltage and time conditions, and the conditions for allocating the PS beads into $15\ \mu\text{m}$ hole were optimized at 80 mV and 15 min, respectively. In the optimized condition, the relative AIF was observed approximately 4.908 ± 0.299 . Finally, in $3\ \mu\text{m}$ and $15\ \mu\text{m}$ hole, the AIFs were approximately 3.143 and -1.346 by 2 nm of protein and about -2.515 and 4.211 by 30 nm of the PS beads, respectively. The results showed that 2 nm of the protein and 30 nm of PS beads were separated by DEP force in each microhole effectively, and that our method is applicable as a new method to verify an efficiency of the labeling for bead-based fluorescent sensor $\nabla|E|^2$.

1. Introduction

Labeling is one of the essential processes for analyzing and tracking the biomolecules and proceeds by conjugating the molecules with various materials such as isotope markers [1], photochromic compounds [2], and fluorescence polystyrene (PS) beads [3–5]. Especially, fluorescent PS beads have competitive price, high accessibility, and controllability so that various biomolecules such as protein [6], cell [3], and

deoxyribonucleic acid (DNA) [7] have been conjugated with fluorescent PS beads followed by being quantified and qualified [8–10]. Qin et al. separated the protein which conjugated with surface-modified fluorescent PS [11], and Fakhri et al. multidetected the viral DNA using gold nanoparticle-coated fluorescent PS beads [12]. However, fluorescent PS beads are not conjugated with biomolecules perfectly; in other words, their labeling efficiency is under 100%, and consequently, not only biomolecules conjugated

with fluorescent PS beads but also nonconjugated biomolecules existed in the analyte. The nonconjugated biomolecules decrease the accuracy and sensitivity in analyzing and tracking of the biomolecules; hence, a method is required for separating the biomolecules conjugated with PS beads and nonconjugated biomolecules, namely, the residue molecules. So, residue biomolecules after labeling need to be separated from the biomolecules, which are conjugated with labels, ideally. Although centrifugation approaches [13, 14] and fluidic-based approaches [15] are suitable for separating the residue molecules, these approaches are complex and require an additional process.

Dielectrophoresis (DEP), resulting from inhomogeneous electric fields, has been utilized for the specific manipulation of the particles, cells, and viruses as well as biomolecules such as DNA and even single protein, because of its simplicity, efficiency, and usability [16–18]. The intensity of the DEP force is dominated by the size of the molecules and the strength of the electric fields, which occurred between the electrodes, so that various molecules are affected by a different intensity of the force according to the size of the molecules and the structure of the electrode. Lapizco-Encinas et al. concentrated and separated the live and dead bacteria with insulator-based DEP (iDEP) [19]. But two types of bacteria were separated according to different types of DEP force, negative DEP and positive DEP, and Chen et al. suggested a simplified dielectrophoretic-based microfluid device for particle separation [20]. But these approaches were limited for observing the various molecules simultaneously or consisted of the complex structure.

Here, we suggest a simple method to separate the non-conjugated protein, namely, the residue protein, and the protein conjugated with PS beads with the DEP force, which is applicable for verifying the efficiency of labeling between protein and PS beads. The protein and PS beads were separated into two microholes with different diameters and formed on a single electrode according to the intensity of DEP force induced. The intensity of the DEP force increased when the diameter of the microhole was smaller, and thus, stronger repulsive force and attractive force occurred in the small microhole than the large one. Consequently, the smaller molecules, residue protein, were allocated into the small microhole, whereas the bigger molecules, PS beads, were expelled from that small microhole followed by allocating into the large microhole; it means that the protein and PS beads were separated. To verify the separation between protein and PS beads, approximately 2 nm of the protein, amyloid beta 42, and 30 nm fluorescent PS beads were used. The diameter of the two microholes for separating the protein and PS beads was optimized to 3 μm and 15 μm , respectively, by calculating the intensity of $\nabla|E|^2$ in each microhole with COMSOL simulation. Also, an applied voltage to induce the DEP force was optimized to 80 mV, which induced a difference in the $\nabla|E|^2$ force approximately 9.059-fold between two microholes. The microholes were fabricated by micro-electromechanical systems (MEMS) technique, and separation between the protein and polystyrene beads was demonstrated by comparing a relative averaged intensity of fluorescence (AIF) by each protein and each PS bead.

2. Materials and Methods

2.1. Theory. The molecule present in an inhomogeneous electric field, E , is influenced by the DEP force, F_{DEP} , which is expressed as follows [21]:

$$F_{\text{DEP}} = 2\pi r^3 \epsilon_m K(\omega) \cdot \nabla |\vec{E}|^2, \quad (1)$$

where r , ϵ_m , and $K(\omega)$ represent the radius of molecules, the effective permittivity of liquid, and the Clausius–Mossotti factor, respectively. The E and gradient of the electric field $\nabla|E|^2$ are described as follows:

$$\vec{E} = -\frac{\Delta V}{\Delta d}, \quad (2)$$

$$\nabla|\vec{E}| = \frac{\partial^2 V}{\partial d^2} \hat{x} + \frac{\partial^2 V}{\partial d^2} \hat{y} + \frac{\partial^2 V}{\partial d^2} \hat{z}, \quad (3)$$

where V and d are the applying voltage and the distance between the electrodes, respectively. On the basis of (1) and (3), the intensity of the DEP force can be modified through (4) as follows:

$$F_{\text{DEP}} \propto \frac{r^3}{d^2}. \quad (4)$$

The intensity of $\nabla|E|^2$ is calculated with a finite-element model (FEM) in the AC/DC module of COMSOL Multiphysics software 5.2 (COMSOL Inc., USA).

2.2. Materials. Thirty nanometres of the carboxylate-modified polystyrene (PS) bead labeled with fluorescence (Sigma-Aldrich Inc., Korea) and 2 nm of the TAMRA-labeled beta-amyloid (1–42) protein (AnaSpec Inc., USA) were used to verify the separation of molecules, whose excitation/emission wavelength ($\lambda_{\text{ex}}/\lambda_{\text{em}}$) was $\sim 470/505$ nm and $\sim 544/572$ nm, respectively. The protein and PS beads were diluted with 1 mM PBS buffer (Corning Korea Co. Ltd., Korea) to create a 1 ng·mL⁻¹ solution.

2.3. Fabrication of Microholes. Microholes were fabricated by a standard MEMS process. First, an insulation layer, 300 nm of SiO₂, and an electrode layer, 30 nm of tantalum (Ta) and 150 nm of platinum (Pt), were sequentially deposited on the 4-inch silicon (Si) wafer by thermal oxidation and sputtering, respectively. Next, an AZ GXR 601 photoresist (AZ Electronic Materials, Luxembourg) was coated by a spin coater (30 s, 3000 rpm) and exposed (3.8 s, 12 mW·cm⁻²). Then, the hole patterns were etched by inductively coupled plasma etching (Oxford Instruments), and the photoresist was stripped by Microwave Plasma Asher (Plasma-Finish, Germany).

2.4. System Setup for Molecules Separation and Fluorescence Analysis. A DG4062 Series waveform generator (Rigol Technologies Inc., USA) (frequency range: up to 60 MHz; voltage range: up to 10 V), which applies a sinusoidal AC voltage for inducing the DEP force in the microhole on

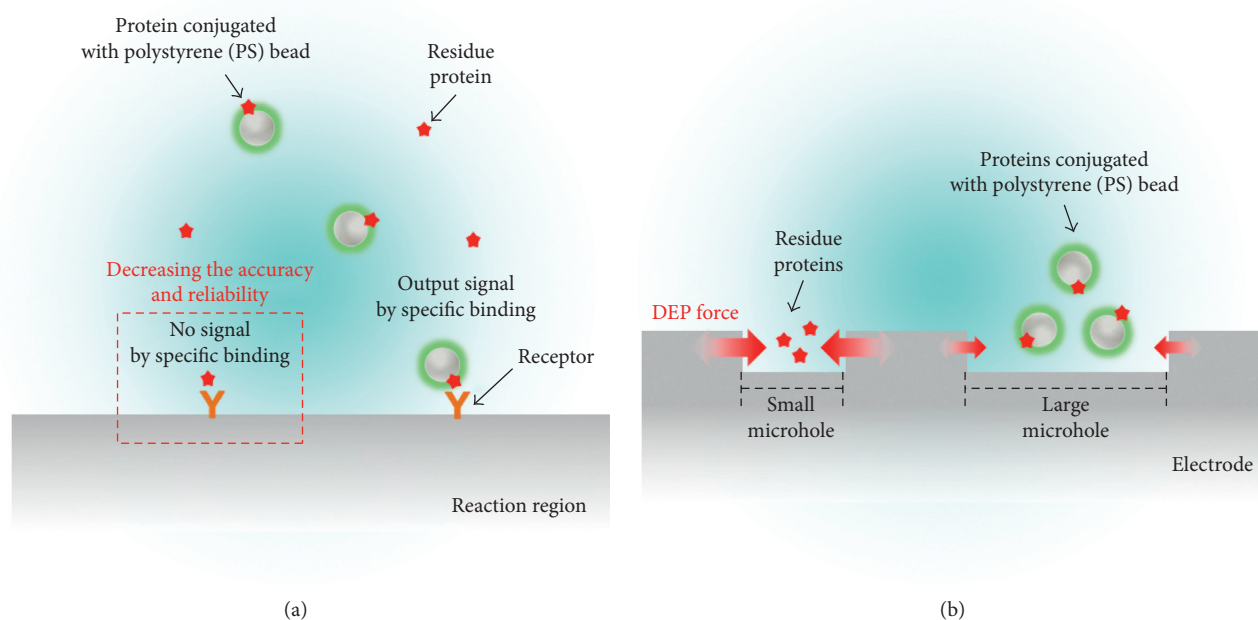


FIGURE 1: Schematic illustration of a simple separation method of the protein and protein conjugated with polystyrene (PS) beads. (a) Intensity of fluorescence by a specific binding of the protein conjugated with PS beads decreased due to a specific binding of the non-conjugated protein, expressed as residue protein. (b) Residue protein and protein conjugated with PS beads were separated by the dielectrophoresis (DEP) force in different microholes, respectively.

a single electrode, was used. The intensity of fluorescence was observed via an electron-multiplying charge-coupled device (ANDORiXonEM), an oil immersion 100x lens (Nikon Corp., Japan) (NA: 1.4), and an Eclipse Ti inverted microscope (Nikon Corp.) equipped with a halogen lamp and a 593 nm (bandwidth: 40 nm) filter and was analyzed by Image-Pro Plus 6.0 (Media Cybernetics Inc., USA). The average intensity of fluorescence (AIF) was calculated by values measured at five random positions in the microhole, and a value of a relative AIF was calculated by dividing the AIF values measured at each condition by the value in the reference condition.

3. Results and Discussion

Protein, nonconjugated with PS beads after labeling, does not emit the fluorescence but binds to the receptor specifically so that it impedes the specific binding between the ideally conjugated protein with PS beads and receptor, followed by decreasing the accuracy and reliability in the molecules' analyzing and tracking process (Figure 1(a)). Thus, the nonconjugated protein, namely, the residue protein, should be separated from the protein conjugated with PS beads. When alternating current (AC) voltage is applied to the electrode with microholes, the protein is allocated into each microhole according to the intensity of the DEP force that occurred in each microhole. The intensity of the DEP force is related to the diameter of the molecules and the distance between the electrodes, namely, the size of microholes, as described in (4), and consequently allocates different molecules into each microhole, respectively:

residue protein, smaller than the PS beads, is allocated into the small microhole, whereas the PS beads are placed in the large microhole—two molecules separate into small and large microholes, respectively (Figure 1(b)).

In order to separate the residue protein and conjugated protein with PS beads in each microhole, 4.5 kDa of amyloid beta, whose diameter was calculated to be approximately 2 nm, was used as a residue protein, and the conjugated protein with PS beads was simplified to just PS beads. The length and width of the electrode were fixed to 27 μm and 21 μm , respectively, and the diameter of the small microhole, d , and pitch between two microholes, p , were fixed to 3 μm . The intensity of the applied AC voltage and size of microholes were optimized via the COMSOL simulation (Figure 2(a)). Firstly, maximum intensity of $\nabla|E|^2$ in the small microhole was simulated according to the applied AC voltage (Figure 2(b)). Black line and scatter showed the maximum intensity of $\nabla|E|^2$ that occurred in the small microhole, and red line and scatter indicated the size of protein, which was allocated into the small microhole, depending on the intensity of the applied AC voltage. The intensity of $\nabla|E|^2$ increased parabolically and size of the protein decreased accordingly. The results signified that approximately 30 mV voltage, which resulted in $\nabla|E|^2$ with intensity approximately $2.310 \times 10^{13} \text{ V}^2 \cdot \text{m}^{-3}$, was required to place 2 nm of the protein in the 3 μm hole. Also, the maximum intensity of $\nabla|E|^2$ that occurred in the other microhole was simulated according to the size of the other microhole at the condition that applied 30 mV AC voltage (Figure 2(c)). The diameter of the other microhole was expressed as a ratio to the diameter for the 3 μm hole, and the

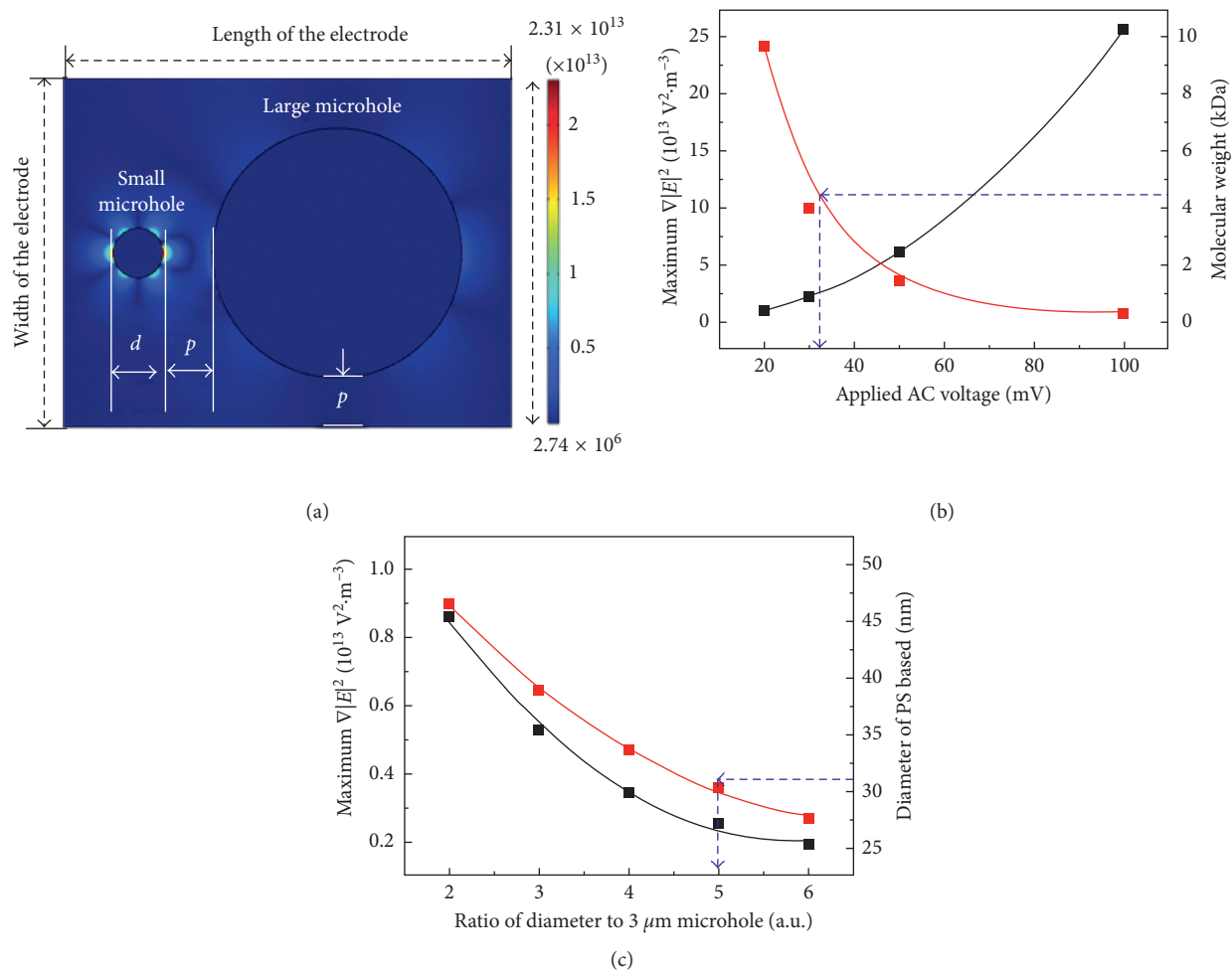


FIGURE 2: Simulation for separating the molecules by DEP force in the two microholes. (a) Distribution of $\nabla|E|^2$ at the top view of the electrode. The diameter of the small microhole and pitch between two microholes were represented as “ d ” and “ p ,” respectively. (b) According to the applied voltage, maximum intensity of $\nabla|E|^2$ occurring in the $3 \mu\text{m}$ hole increased, whereas molecular weight of the protein, allocated into the microhole, decreased. (c) Maximum intensity of $\nabla|E|^2$ in the other microhole and the diameter of PS beads, allocated into the hole, decreased according to the increase of the diameter.

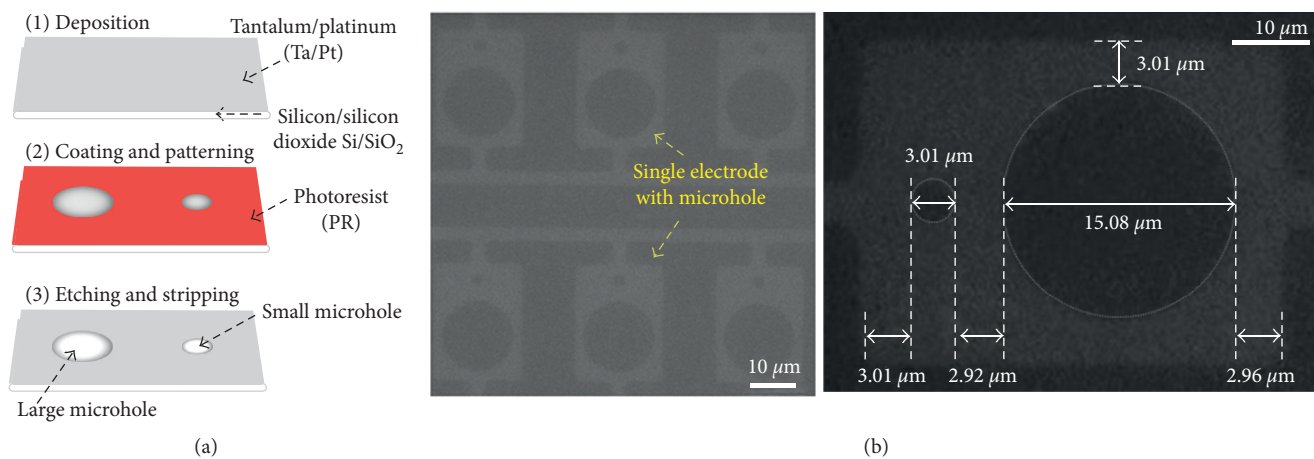


FIGURE 3: Fabrication of the single electrode consisting of two different-sized microholes by MEMS technology. (a) Schematic illustration of the fabrication process of the microholes. (b) Microscopic image of the two different microholes.

intensity of $\nabla|E|^2$ decreased according to the increase in the ratio of the diameter. In the $6 \mu\text{m}$ microhole (the ratio was 2), intensity of $\nabla|E|^2$ was about $0.861 \times 10^{13} \text{ V}^2 \cdot \text{m}^{-3}$ and it is too

strong to allocate 30 nm of the PS beads into the hole. $\nabla|E|^2$ was approximately $0.528 \times 10^{13} \text{ V}^2 \cdot \text{m}^{-3}$, $0.347 \times 10^{13} \text{ V}^2 \cdot \text{m}^{-3}$, $0.255 \times 10^{13} \text{ V}^2 \cdot \text{m}^{-3}$, and $0.194 \times 10^{13} \text{ V}^2 \cdot \text{m}^{-3}$ in each value of

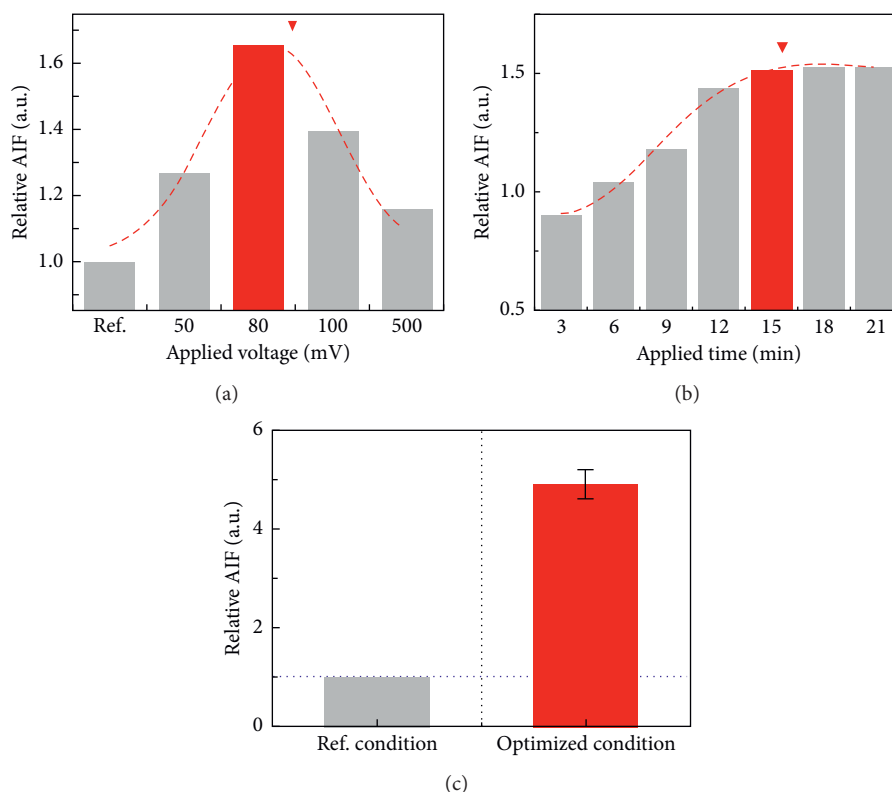


FIGURE 4: Optimization of the DEP condition by measuring the average intensity of fluorescence (AIF) of the PS beads in the $15\ \mu\text{m}$ hole. Relative AIF was verified according to (a) the applied voltage and (b) the applied time of AC voltage. (c) Relative AIF by the PS beads in the $15\ \mu\text{m}$ hole was compared in each reference and optimized DEP condition.

the ratio, and an optimized size of the microhole for placing 30 nm of the PS beads into the hole was verified to be $15\ \mu\text{m}$. Thus, the two microholes for separating the residue protein and protein conjugated with PS beads were optimized to $3\ \mu\text{m}$ and $15\ \mu\text{m}$, respectively, whose difference in the intensity was approximately 9.059-fold.

Two microholes in the electrode were produced via a standard MEMS process on a 4-inch silicon (Si) wafer. The fabrication process consisted of 3 steps (Figure 3(a)), and details of the process are described in Material and Methods. The diameter of the fabricated small and large microholes was approximately $3\ \mu\text{m}$ and $15\ \mu\text{m}$, respectively, and pitch between two microholes was about $3\ \mu\text{m}$ (Figure 3(b)).

Various conditions of DEP, intensity of the DEP force and applied time, were optimized by measuring the relative AIF resulting from placing the PS beads in the $15\ \mu\text{m}$ hole. In order to optimize the intensity of the DEP force, the applied frequency required for the DEP force to occur was fixed at 50 MHz. Firstly, relative AIF was measured in various applying voltage conditions ranging from 0 V (ref.) to 500 mV, and consequently, it was maximized at 80 mV (Figure 4(a)). The values were approximately 1, 1.265, 1.655, 1.396, and 1.1604 in ref., 50 mV, 80 mV, 100 mV, and 500 mV, respectively. The results indicated that the PS beads were most effectively placed in the microhole by the DEP force induced by the applied voltage 80 mV; consequently, the intensity of the applied voltage was settled to 80 mV. Also, in order to optimize the applied time condition of DEP force, the

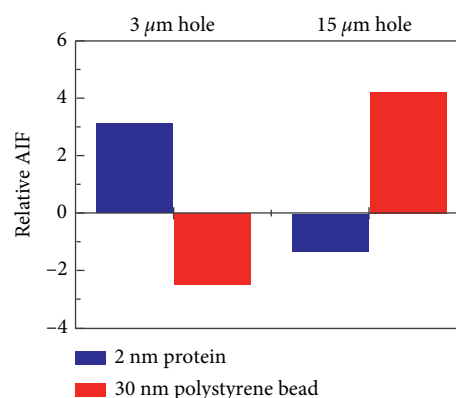


FIGURE 5: Relative AIF by 2 nm of the protein and 30 nm of the PS beads in $3\ \mu\text{m}$ and $15\ \mu\text{m}$ holes, respectively.

relative AIF was measured according to time every 3 minutes up to 21 minutes (Figure 4(b)). The AIF increased gradually depending on the time up to 15 min and was saturated afterward: each value of the AIF was approximately 0.907, 1.048, 1.184, 1.450, 1.526, 1.535, and 1.536 according to the applied time. Hence, the applied voltage and time were optimized to 80 mV and 15 minutes, respectively, and the relative AIF was observed to be approximately 4.908 ± 0.299 in the optimized condition (Figure 4(c)). The result demonstrated that the PS beads were allocated into the $15\ \mu\text{m}$ hole effectively.

Finally, based on these results, a separation of the protein and PS beads in $3\ \mu\text{m}$ and $15\ \mu\text{m}$ holes, respectively, was demonstrated (Figure (5)). It was also confirmed by comparing the AIF by each molecule in the two microholes at the previous optimized condition. The relative AIF by 2 nm of the protein in the $3\ \mu\text{m}$ hole was a positive value, but the value by 30 nm of the PS beads was negative, and the values were approximately 3.143 and -1.346 , respectively, whereas in the $15\ \mu\text{m}$ hole, the relative AIFs by the protein and the PS beads showed an opposite sign compared with the previous values, and the values were approximately -2.515 and 4.211 , respectively. The negative value of the AIF indicated that the molecules were moving far away owing to the strong DEP force in the microhole, and the positive value of the AIF signified that the molecules were attracted and trapped into the microhole by the DEP force. Thus, the results signified that the DEP force allocated 2 nm of the protein and 30 nm of the PS beads into $3\ \mu\text{m}$ and $15\ \mu\text{m}$ holes, respectively. The results demonstrated that 2 nm of the protein and 30 nm of the PS beads were separated by DEP force in each microhole, effectively.

4. Conclusions

In this paper, a simple method for separation between 2 nm of the protein and PS beads into different microholes, respectively, by the DEP force was demonstrated. In order to separate two molecules, the diameter of the two microholes was simulated and the intensity of the DEP force induced in the microholes was calculated via simulation. The optimized diameter of the two microholes was $3\ \mu\text{m}$ and $15\ \mu\text{m}$, and a difference in the DEP force between two microholes was approximately 9.059-fold. The condition of the DEP force to separate two molecules was optimized experimentally: intensity of the AC voltage was 80 mV and the applied time was 15 minutes. The molecules which were separated by the DEP force in each microhole were verified by measuring the relative AIF by each molecule. In $3\ \mu\text{m}$ and $15\ \mu\text{m}$ holes, the AIFs were approximately 3.143 and -1.346 by 2 nm of the protein and about -2.515 and 4.211 by 30 nm of the PS beads, respectively. Consequently, the results demonstrated that 2 nm of the protein and 30 nm of the PS beads were separated by DEP force in each microhole, effectively. Our method has high expandability in separation of various-sized molecules, and furthermore, it is applicable for verification of the labeling efficiency.

Data Availability

The data used to support the findings of this study are available from the corresponding author upon request.

Conflicts of Interest

The authors declare that there are no conflicts of interest regarding the publication of this paper.

Acknowledgments

This work was mainly supported by the Dongguk University Research Fund of 2017. Taewon Ha and Youngbaek Kim are

grateful for financial support from the Korea Institute of Industrial Technology (Project no. EO170047).

References

- [1] X. Chen, L. M. Smith, and E. M. Bradbury, "Site-specific mass tagging with stable isotopes in proteins for accurate and efficient protein identification," *Analytical Chemistry*, vol. 72, no. 6, pp. 1134–1143, 2000.
- [2] M. Lummer, F. Humpert, M. WiedenlÜbbert, M. Sauer, M. SchÜttpelz, and D. Staiger, "A new set of reversibly photoswitchable fluorescent proteins for use in transgenic plants," *Molecular Plant*, vol. 6, no. 5, pp. 1518–1530, 2013.
- [3] H. Sahoo, "Fluorescent labeling techniques in biomolecules: a flashback," *RSC Advances*, vol. 2, no. 18, pp. 7017–7029, 2012.
- [4] D. Jung, K. Min, J. Jung, W. Jang, and Y. Kwon, "Chemical biology-based approaches on fluorescent labeling of proteins in live cells," *Molecular BioSystems*, vol. 9, no. 5, pp. 862–872, 2013.
- [5] M. M. Bonar and J. C. Tilton, "High sensitivity detection and sorting of infectious human immunodeficiency virus (HIV-1) particles by flow virometry," *Virology*, vol. 505, pp. 80–90, 2017.
- [6] C. Obermaier, A. Griebel, and R. Westermeier, "Principles of protein labeling techniques," *Proteomic Profiling: Methods and Protocols*, vol. 1295, pp. 153–165, 2015.
- [7] T. T. Weil, R. M. Parton, and I. Davis, "Making the message clear: visualizing mRNA localization," *Trends in Cell Biology*, vol. 20, no. 7, pp. 380–390, 2010.
- [8] J. Lu, G. Getz, E. A. Miska et al., "MicroRNA expression profiles classify human cancers," *Nature*, vol. 435, pp. 834–838, 2005.
- [9] B. S. Edwards, T. Oprea, E. R. Prossnitz, and L. A. Sklar, "Flow cytometry for high-throughput, high-content screening," *Current Opinion in Chemical Biology*, vol. 8, no. 4, pp. 392–398, 2004.
- [10] X. H. Gao and S. M. Nie, "Quantum dot-encoded mesoporous beads with high brightness and uniformity: rapid readout using flow cytometry," *Analytical Chemistry*, vol. 76, no. 8, pp. 2406–2410, 2004.
- [11] L. Qin, X. W. He, W. Zhang, W. Y. Li, and Y. K. Zhang, "Surface-modified polystyrene beads as photografting imprinted polymer matrix for chromatographic separation of proteins," *Journal of Chromatography A*, vol. 1216, no. 5, pp. 807–814, 2009.
- [12] H. H. Fakih, M. M. Itani, and P. Karam, "Gold nanoparticles-coated polystyrene beads for the multiplex detection of viral DNA," *Sensors and Actuators B: Chemical*, vol. 250, pp. 446–452, 2017.
- [13] E. Fernández-Vizarrá, M. J. López-Pérez, and J. A. Enriquez, "Isolation of biogenetically competent mitochondria from mammalian tissues and cultured cells," *Methods*, vol. 26, no. 4, pp. 292–297, 2002.
- [14] U. Michelsen and J. von Hagen, "Isolation of subcellular organelles and structures," in *Methods in Enzymology*, pp. 305–328, Academic Press, Cambridge, MA, USA, 2009.
- [15] A. A. S. Bhagat, H. Bow, H. W. Hou, S. J. Tan, J. Han, and C. T. Lim, "Microfluidics for cell separation," *Medical and Biological Engineering and Computing*, vol. 48, pp. 999–1014, 2010.
- [16] S. Paracha and C. Hestekin, "Field amplified sample stacking of amyloid beta (1-42) oligomers using capillary electrophoresis," *Biomicrofluidics*, vol. 10, no. 3, article 033105, 2016.

- [17] T. D. Mai, F. Qukacine, and M. Taverna, "Multiple capillary isotachopheresis with repetitive hydrodynamic injections for performance improvement of the electromigration pre-concentration," *Journal of Chromatography A*, vol. 1453, pp. 116–123, 2016.
- [18] L. Zheng, J. P. Brody, and P. J. Burke, "Electronic manipulation of DNA, proteins, and nanoparticles for potential circuit assembly," *Biosensors and Bioelectronics*, vol. 20, no. 3, pp. 606–619, 2004.
- [19] B. H. Lapizco-Encinas, B. A. Simmons, E. B. Cummings, and Y. Fintschenko, "Dielectrophoretic concentration and separation of live and dead bacteria in an array of insulators," *Analytical Chemistry*, vol. 76, no. 16, pp. 1571–1579, 2004.
- [20] X. Chen, Y. Ren, W. Liu et al., "A simplified microfluidic device for particle separation with two consecutive steps: induced charge electro-osmotic prefocusing and dielectrophoretic separation," *Analytical Chemistry*, vol. 89, no. 17, pp. 9583–9592, 2017.
- [21] A. Ramos, H. Morgan, N. G. Green, and A. Castellanos, "Ac electrokinetics: a review of forces in microelectrode structures," *Journal of Physics D: Applied Physics*, vol. 31, no. 18, p. 2338, 1998.

Review Article

Benzo[*g*]coumarin-Based Fluorescent Probes for Bioimaging Applications

Yuna Jung,¹ Junyang Jung ,^{1,2} Youngbuhm Huh ,^{1,2} and Dokyoung Kim ^{1,2,3}

¹Department of Biomedical Science, Graduate School, Kyung Hee University, 26 Kyungheedaero, Dongdaemun-Gu, Seoul 02447, Republic of Korea

²Department of Anatomy and Neurobiology, College of Medicine, Kyung Hee University, 26 Kyungheedaero, Dongdaemun-Gu, Seoul 02447, Republic of Korea

³Center for Converging Humanities, Kyung Hee University, 26 Kyungheedaero, Dongdaemun-Gu, Seoul 02447, Republic of Korea

Correspondence should be addressed to Dokyoung Kim; dkim@khu.ac.kr

Received 9 March 2018; Accepted 22 April 2018; Published 14 June 2018

Academic Editor: Verónica Pino

Copyright © 2018 Yuna Jung et al. This is an open access article distributed under the Creative Commons Attribution License, which permits unrestricted use, distribution, and reproduction in any medium, provided the original work is properly cited.

Benzo[*g*]coumarins, which consist of coumarins fused with other aromatic units in the linear shape, have recently emerged as an interesting fluorophore in the bioimaging research. The pi-extended skeleton with the presence of electron-donating and electron-withdrawing substituents from the parent coumarins changes the basic photophysical parameters such as absorption and fluorescence emission significantly. Most of the benzo[*g*]coumarin analogues show red/far-red fluorescence emission with high two-photon absorbing property that can be applicable for the two-photon microscopy (TPM) imaging. In this review, we summarized the recently developed benzo[*g*]coumarin analogues including photophysical properties, synthesis, and applications for molecular probes that can sense biologically important species such as metal ions, cell organs, reactive species, and disease biomarkers.

1. Introduction

Coumarin (2*H*-chromen-2-one) is a chemical compound in the benzopyrone chemical class that can be found in many natural species [1, 2]. Coumarins possess variety of biological activities and unique photophysical properties. Among them, the fluorescent property received much attention recently due to its high quantum yield, high stability, and biological compatibility [3, 4]. The coumarin-based fluorescent dyes and molecular probes have been applied not only for basic science such as physics, chemistry, medical science, and clinical science but also for industry and engineering [5, 6]. In progress, various kinds of the expanded or combined structure of coumarin derivatives have been discovered. Among them, linearly extended derivatives, benzo[*g*]coumarin, show superior photophysical properties in the bioimaging applications over the other derivatives [7]. Moreover, a large two-photon absorbing ability with longer excitation and

emission wavelengths in optical window, high photostability, and high chemical stability are the key advantageous features of benzo[*g*]coumarin derivatives. In this review, we describe a brief explanation of benzocoumarin analogues with photophysical properties, their synthetic methods, and the recently developed benzo[*g*]coumarin-based one/two-photon excitable fluorescent dyes/probes that can sense biologically important species.

2. Benzo[*g*]coumarins

Benzocoumarin derivatives can be categorized into four types depending on the position of the fused aromatic ring in the parent coumarin backbone (Figure 1): (1) benzo[*c*]coumarin (3,4-benzocoumarin) fused on 3,4-position; (2) benzo[*g*]coumarin (6,7-benzocoumarin) fused on 6,7-position; (3) benzo[*f*]coumarin (5,6-benzocoumarin) fused on 5,6-position; and (4) benzo[*h*]coumarin (7,8-benzocoumarin) fused on 7,8-position.

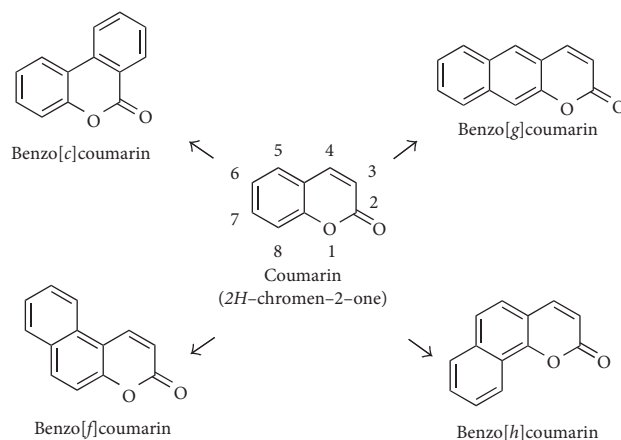


FIGURE 1: Chemical structures of coumarin and benzocoumarin derivatives.

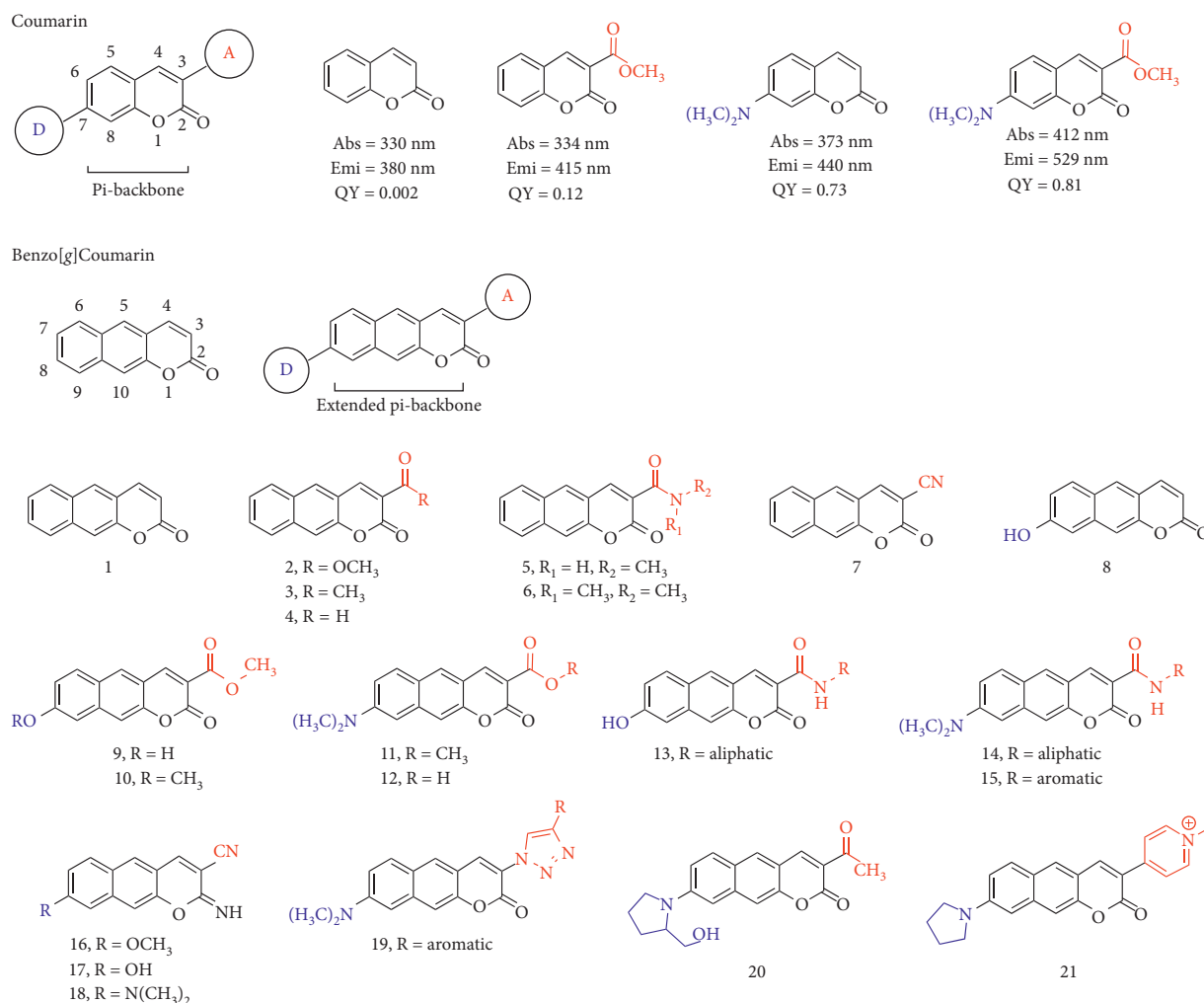


FIGURE 2: Chemical structure and basic photophysical properties of coumarin and benzo[g]coumarin derivatives. D: electron-donating group; A: electron-accepting group. The wavelengths are derived from the highest intensity values in the absorption and fluorescence emission spectra.

2.1. Photophysical Properties of Benzo[g]coumarin Analogues. The photophysical property such as absorption and fluorescence emission of coumarin derivatives has been

identified by many scientists in various fields. Among the derivatives, the functional group substitution on the 3- and 7-position gives large property changes from the original

backbone. Typically, coumarin itself shows maximum absorbance and emission at a short wavelength ($\lambda_{\max, \text{abs}} = 330 \text{ nm}$; $\lambda_{\max, \text{emi}} = 380 \text{ nm}$) with poor fluorescence quantum yield (Φ_F) (Figure 2) [7]. However, the appropriate substitution, electron donor-acceptor- (D-A-) type structure on the pi-backbone, induces intramolecular charge transfer (ICT) accompanied with the quantum yield increment and the red shift of the fluorescence emission wavelength (see the absorption and emission wavelengths with quantum yield information in Figure 2) [8, 9].

Considering the bioimaging application of the coumarin fluorophore, the excitation and emission at a shorter wavelength give drawbacks such as (i) interference of autofluorescence from the biological substances, (ii) limited imaging depth, (iii) photodamage of the sample, and (iv) photobleaching of the fluorophore [10, 11]. In that sense, pi-extended benzo[*g/f/h*]coumarins are expected to provide several advantageous features over the corresponding coumarins due to their extended aromatic backbone that evokes longer wavelength absorption and fluorescence emission. Also, the conformationally restricted pi-backbone extension gives high photostability with a high quantum yield.

The photophysical properties of benzocoumarin analogues may also be predicted based on the type and substitution position. Recently, Ahn et al. reported a systematic analysis result for photophysical properties of benzocoumarin analogues [12]. They revealed that linear-type benzo[*g*]coumarins give similar substitution-induced property changes like parent coumarins, and the fluorescence property is suitable for bioimaging application over the others (very poor or no fluorescence from the benzo[*f/h*] coumarin in aqueous media).

The electron-withdrawing functional group-substituted benzo[*g*]coumarin at 3-position induces a red shift of fluorescence from the parent benzocoumarin (**1**, $\lambda_{\max, \text{emi}} = 459 \text{ nm}$); ester moiety (**2**, 534 nm), ketone (**3**, 549 nm), aldehyde (**4**, 547 nm), amide (**5**, 515 nm), and nitrile (**7**, 533 nm) (Figure 2; Table 1). Interestingly, the combination of electron-withdrawing and electron-donating moieties at 3- and 8-position gives a significant shift of both absorption and emission spectra to the longer wavelength region (**8–21**; Figure 2; Table 1). The substitution of the hydroxyl group alone at 7-position (electron-donating position) shows no significant red shift ($\lambda_{\max, \text{emi}} = 466 \text{ nm}$) (**8**), but the combination with electron-withdrawing substitution (methyl ester) at 3-position induces large changes (**9**, **10**, and **13**; $\lambda_{\max, \text{emi}} > 500 \text{ nm}$). The alkylamine ($-\text{NR}_2$, R = alkyl) substitution at 8-position gives more significantly red-shifted absorption ($>430 \text{ nm}$) and fluorescence emission ($>580 \text{ nm}$) with a combination of ester, amide, nitrile, triazole, and pyridinium salts (**11–21**). The details of each compound with their photophysical properties are covered in the next chapter with the reported applications.

2.2. Synthesis of Benzo[*g*]coumarin Analogues. Synthesis of benzo[*g*]coumarin analogues follows the established synthetic routes including the Knoevenagel condensation or Wittig reaction with intramolecular cyclization reaction to

TABLE 1: Photophysical properties of the benzo[*g*]coumarin derivatives **11–21**. The wavelengths are derived from the highest intensity values in the absorption and fluorescence emission spectra in the described solvent.

Compound	λ_{abs} (nm)	λ_{emi} (nm)	Solvent	Reference
1	320	459	CH ₃ CN	[13]
2	332	534	CH ₃ CN	[13]
3	337	549	CH ₃ CN	[13]
4	345	547	CH ₃ CN	[13]
5	334	515	CH ₃ CN	[13]
6	326	510	CH ₃ CN	[13]
7	335	533	CH ₃ CN	[13]
8	357	466	CHCl ₃	[14]
9	450	603	DI H ₂ O	[12]
10	355	539	DI H ₂ O	[12]
11	467	623	EtOH	[15]
12	413	599	DI H ₂ O	[12]
13	370/453	542/604	pH 4/pH 7 buffer	[16]
14	470	626	pH 7.4 buffer	[17]
15	450	600	pH 7.4 buffer	[18]
16	357	522	DI H ₂ O	[12]
17	435	582	DI H ₂ O	[12]
18	444	607	EtOH	[15, 19]
19	431	591	CH ₃ CN	[20]
20	487	633	pH 7.4 buffer	[21]
21	527	691	EtOH	[22]

o-hydroxynaphthaldehyde (Figure 3(a)) [7]. Alternatively, the direct electrophilic substitution of naphthols with β -keto ester followed by cyclization also gives benzo[*g*] coumarin in the presence of a catalyst. The metal-catalyzed aryl C–H functionalization of alkynoates is also feasible (Figure 3(a)).

Synthetic methods to make an electron-donating moiety on benzo[*g*]coumarin analogues were developed by many scientists including Ahn et al. [12, 15]. Representative derivatives which have a primary/secondary amine or a hydroxy/methoxy moiety at the 8-position were synthesized from the key intermediates A and B (Figure 3(b)). Intermediate A analogues were prepared by monoamination through the Bucherer reaction, protection of the hydroxyl group by methoxymethyl ether (MOM), and formylation through directed lithiation. On the contrary, methoxy or hydroxy group-substituted intermediate B analogues were prepared by monoprotection of the hydroxyl group by MOM first and then by methylation and formylation [12].

The MOM deprotection of the intermediates A and B in acidic condition gives an *o*-hydroxynaphthaldehyde intermediate, and the cascade intramolecular cyclization reaction generates benzo[*g*]coumarin derivatives (Figure 3(b)) [15, 19].

3. Benzo[*g*]coumarins for Fluorescent Probes

Benzo[*g*]coumarin derivatives have been used in various research areas. In particular, their unique photophysical property gives many advantages in the bioimaging applications such as fluorescent probes and tags and photolabile materials.

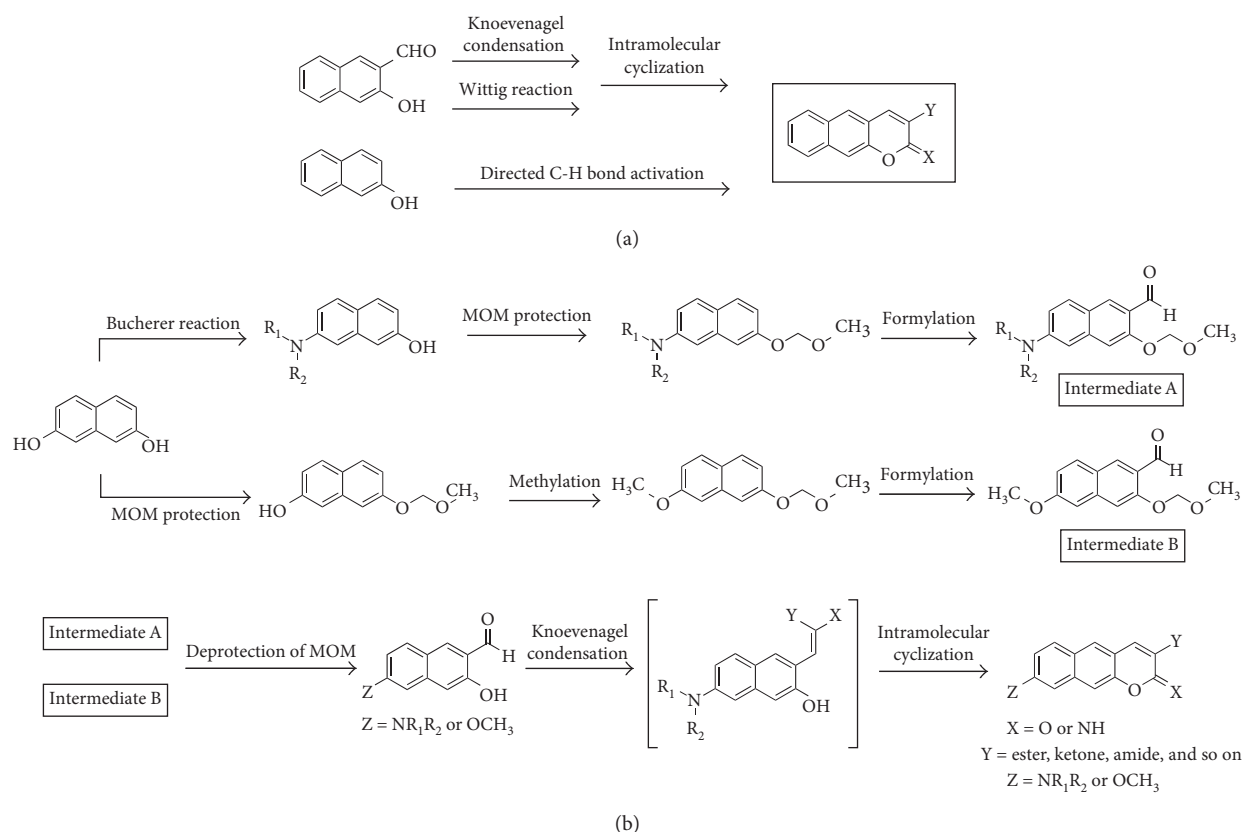


FIGURE 3: Synthetic routes for benzo[*g*]coumarin derivatives. (a) Routes for nonsubstitution at C-8 position. (b) Routes for substitution at C-8 position. X = O or NH; Y = ester, ketone, amide, nitrile, and so on; Z = NR₁R₂ or OR (R = alkyl).

Recently, a few examples of notable applications using benzo[*g*]coumarin derivatives for the fluorescent probes were reported. The fluorescent probe is undoubtedly an essential and useful tool in the biological, medical, and environmental sciences to investigate molecular interactions and biological activities, among others [23]. As we described above, benzo[*g*]coumarin analogues with suitable substitution show the absorption and fluorescence emission at the longer wavelength region (red and near-infrared) that gives better cellular or tissue imaging results than the shorter wavelength. Moreover, the pi-extended structure with proper substitutions gives a sufficiently large two-photon absorbing property that is applicable for the two-photon excitation microscopy [19]. Two-photon excitation microscopy is a fluorescence imaging technique that allows imaging of *ex vivo* and *in vivo* tissue up to millimeter depths [10, 24].

In this chapter, we summarized recently reported fluorescent probes based on the benzo[*g*]coumarin analogues (one/two-photon absorbing) with their interesting applications in the (i) sensing and bioimaging of biologically important species including metal ions, cell organs, reactive oxygen species (ROS), and disease biomarkers and (ii) deep tissue imaging.

3.1. Sensing of Metal Ions

3.1.1. Copper Ions (Cu²⁺). Copper ion plays crucial roles in living systems including signal transduction, oxygen

transportation via copper metalloenzymes, cellular energy generation, and cofactors of protein activity. As a result, the homeostasis of copper ions in the biological system is very important and directly related with various diseases: Alzheimer's disease (AD), Wilson's disease, Prion disease, and Menkes disease [25, 26].

Cho et al. reported a fluorescent probe for Cu²⁺ and quantitatively estimated ion concentrations in human tissues by two-photon microscopy imaging and analysis [27]. The amide- and dimethylamino-substituted benzo[*g*]coumarin analogue is linked with a benzo[*h*]coumarin analogue as an internal reference (internal reference: insensitive toward substrates or environment and maintains a steady fluorescence intensity) (**22**; Figure 4). The fluorescence intensity of benzo[*g*]coumarin at the red region (emission: 550–650 nm) was decreased through a chelation to the copper ion with a piperazine linker. Benzo[*g*]coumarin analogue (sensing part) and benzo[*h*]coumarin analogue (internal reference part) serve sufficiently high two-photon action cross section ($\Phi\delta$, GM value), 32 GM and 46 GM in ethanolic water (EtOH/HEPES 9:1 v/v, pH 7.0) at 750 nm two-photon excitation, respectively. Probe **22** shows high sensitivity (0.84 μ M) and selectivity toward Cu²⁺ with no perturbation due to high concentration of biological alkali and alkaline earth metal ions. They investigated the quantitative estimation of the Cu²⁺ concentration in live cells, rat brain tissue, and human colon tissue samples by using two-photon microscopy and analyzed the results. The higher

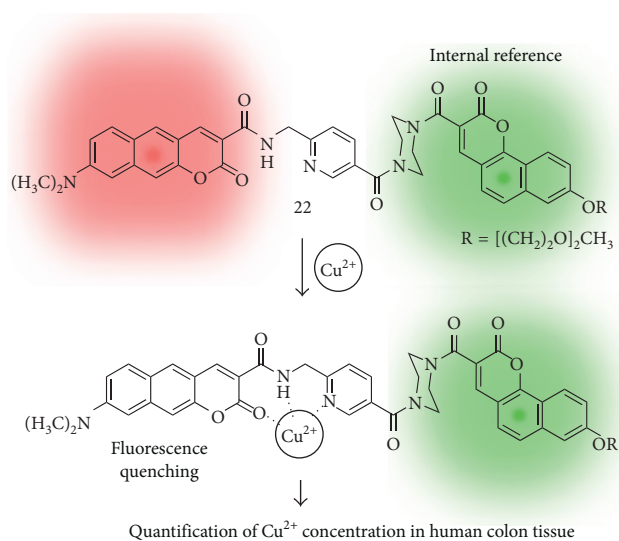


FIGURE 4: Benzo[*g*]coumarin- and benzo[*h*]coumarin-based fluorescent probe for the copper ion (22).

concentration of Cu^{2+} in the cancer tissue ($22 \pm 3 \mu\text{M}$) was observed than in polyp ($13 \pm 2 \mu\text{M}$) or normal ($8.2 \pm 0.3 \mu\text{M}$) samples, and it revealed that estimation of Cu^{2+} concentration may be useful for the diagnosis of colon cancer.

3.1.2. Sodium Ions (Na^+). Sodium ion is one of the most important analytes in life science. It is necessary for live species for the nerve impulses, heart activity, metabolic functions, and biological balance [28, 29]. The Na^+ concentration range in the intracellular (5–30 mM) and extracellular (100–150 mM) space was observed, and competitive cation K^+ also showed similar concentrations. Accordingly, a development of tools for selective detection of Na^+ over K^+ is very important and challenging. Recently, Holdt et al. designed a Na^+ selective fluorescent probe based on the benzo[*g*]coumarin derivatives which have an *N*-(*o*-methoxyphenyl)aza-15-crown-5 moiety (23; Figure 5) [20]. A higher Na^+/K^+ selectivity of 23 was observed, but also, it gives a higher K_d value (223 mM) as a limitation for detection of lower concentration of Na^+ . In this study, the bioimaging application was not reported, but they proposed a design strategy to develop benzocoumarin-based fluorescent probes.

3.1.3. Mercury Ions (Hg^{2+}). Mercury ion is a chemical that is widely used in industry and basic science [30]. However, mercury is a highly poisonous element and causes damage to the central nervous system and other organs. So far, various kinds of detecting methods for mercury species (Hg^{2+} , MeHg^+ , etc.) including fluorescent probes have been developed [30]. By using the latent probe approach with the benzo[*g*]coumarin platform, Ahn et al. reported new fluorescent probes for mercury ion sensing (Figure 6) [15]. The cleavage of sensing moiety on the platform by selective and sensitive chemical reaction toward the target analyte generates a chemically unstable intermediate,

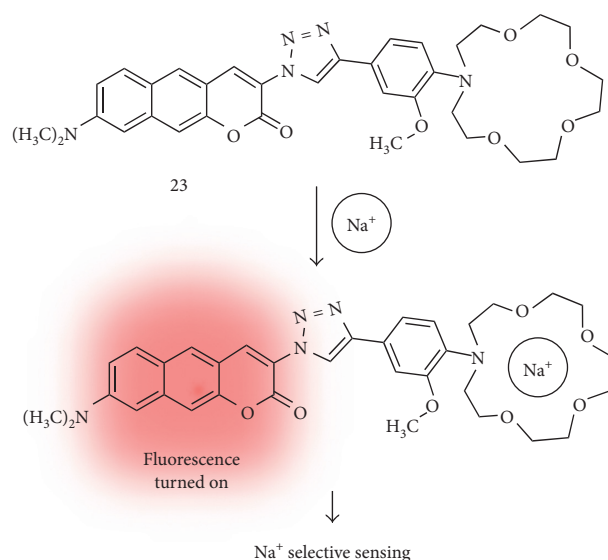


FIGURE 5: Benzo[*g*]coumarin-based fluorescent probe for the sodium ion (23).

which undergoes a fast cyclization reaction to afford an iminobenzo[*g*]coumarin derivative (24; Figure 6(a)). For the mercury ion sensing, they introduce a vinyl ether group to the Hg^{2+} -promoted hydrolysis (25; Figure 6(b)). The probe shows negligible fluorescence emission in the aqueous media due to the generation of the free rotation-induced nonradiative decay pathway from the dicyanoalkene moiety (molecular rotor moiety) and gives significant fluorescence enhancement upon adding mercury ions followed by iminobenzo[*g*]coumarin formation. Compound 24 shows absorption and fluorescence emission maximum at 446 nm and 585 nm, respectively, with a high quantum yield ($\text{QY} = 0.67$).

3.1.4. Fluoride Ions (F^-). Fluoride ion plays an important role in chemistry, environment, medicine, and biology. Therefore, analytical methods that can selectively detect the fluoride ion have been requested in various fields [31]. In this vein, Ahn et al. developed an iminobenzo[*g*]coumarin precursor for fluoride ion sensing (26; Figure 6(c)) [32]. The desilylation of silyl enol ether moiety by fluoride ions followed by the intramolecular cyclization produced a compound 24. In this study, they showed the distribution of fluoride ions in cells and in a live vertebrate, zebrafish, using two-photon microscope (TPM) for the first time. The clear images at deep tissue regions, $\sim 350 \mu\text{m}$ depth, represent the superior property of iminobenzo[*g*]coumarin 24 for the two-photon bioimaging.

3.2. Imaging of Cell Organs

3.2.1. Mitochondria. Mitochondria is an organelle found in almost all eukaryotic organisms and plays important roles such as production of ATP, protein regulation, storage of calcium ions, and cellular metabolism regulation, among others [33]. Therefore, the defects of mitochondrial function

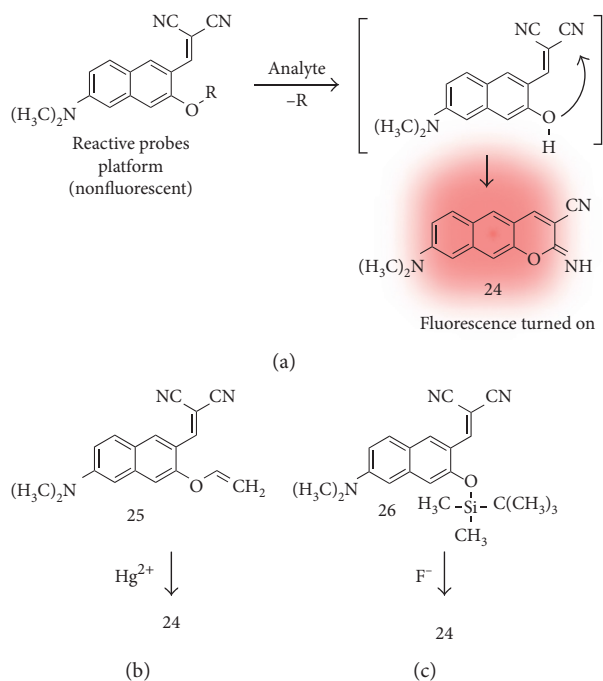


FIGURE 6: (a) Iminobenzo[*g*]coumarin analogue (**24**) and structure of its precursor (reactive probes platform) with a proposed sensing mechanism. Reaction-based fluorescent probes for mercury ion (**25**) (b) and fluoride ion (**26**) (c).

could be directly related to many diseases. So far, various techniques to understand the biological and pathological roles of mitochondria have been developed, and recently, fluorescence methods with imaging materials are used as a standard method to monitor mitochondria dynamics at the subcellular level. In 2014, Kim et al. reported a red-emissive two-photon probe (**27**; Figure 7) based on the benzo[*g*]coumarin for the real-time imaging of mitochondria tracking [17]. The mitochondrial-targeting moiety, triphenylphosphonium (TPP) salt, is linked on the electron-withdrawing part of the benzo[*g*]coumarin core via the amide bond, and the resulting compound **27** exhibited absorption and emission maximum at 470 nm and 626 nm, respectively, with no pH-sensitive changes in the biologically relevant pH range. The staining ability of **27** toward mitochondria was verified by the costaining experiment in the T98G cell line with MitoTracker Green (MTG) as a known mitochondrial labeling marker, and the high Pearson's colocalization coefficient value (0.96) indicates the organ specificity of **27** for mitochondria. In the TPM tissue imaging application using **27**, they observed the evenly distributed mitochondria in the CA1–CA3 region of the rat hippocampal tissue slice at a 200 μm depth.

3.2.2. Mitochondrial pH. The monitoring of pH values and its dynamics in the cellular organs is very important to understand the pH-related biological, physiological, and pathological roles of cells and organisms [34]. In 2016, Kim et al. reported follow-up results that can monitor pH values in the mitochondria using a benzo[*g*]coumarin

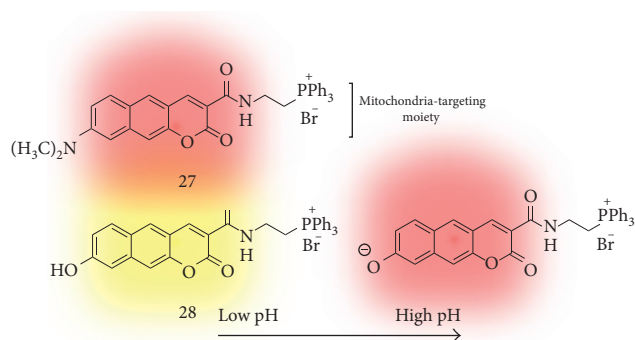


FIGURE 7: Triphenylphosphonium salt-linked benzo[*g*]coumarin probe for mitochondria tracking (**27**) and measuring mitochondrial pH values (**28**).

analogue (**28**; Figure 7) [16]. Probe **28** has a hydroxyl group on the electron-donating position (C-8), and it is protonated or deprotonated at the pK_a value near 8.0 which is a known pH value of mitochondria. At low pH (pH 4.0), **28** shows absorption and emission maximum at 370 nm and 542 nm, respectively, and the peak is shifted to 453 nm and 604 nm at high pH (pH 10.0) in a ratiometric manner. The high two-photon absorption cross section values (20–70 GM) of **28** at pH 4.0 and 10.0 and the high Pearson's colocalization coefficient (0.95) indicate the ability of selective imaging for mitochondria in the tissue samples. In the cellular imaging, a dense population of mitochondria around the nucleus than in the periphery was observed, and higher mitochondrial pH values in the perinuclear position than in the periphery of cells were also monitored. In a further study, they measured the mitochondrial pH values in the astrocyte from the Parkinson's disease (PD) mouse model and in the rat hippocampal tissue slice. Slightly acidic average pH values in the PD model astrocytes are observed compared with the wild-type astrocytes. The deep tissue imaging results provide average mitochondrial pH values in 7.86–7.88 at CA1, CA3, and the dentate gyrus region.

3.3. Sensing of Reactive Species

3.3.1. Nitric Oxide (NO). Nitric oxide is a reactive nitrogen radical species, and its functions in living systems have been recognized to be related with cardiovascular, immune, and central nervous systems [35, 36]. So far, various kinds of chemical tools are developed to monitor the location, amount, and retention time in complex microenvironments such as cell and tissue, and these have been applied for the disease study and management. In 2017, Liu et al. reported a new fluorescent probe specifically for NO based on the *N*-nitrosation of the aromatic amine (**29**; Figure 8) [18]. Probe **29** has a benzo[*g*]coumarin backbone with dimethylamine and amide groups at the 3- and 8-position as an electron-donating and electron-withdrawing moiety, respectively. The original fluorescence emission of benzo[*g*]coumarin at 608 nm (at 473 nm excitation) is quenched by the photo-induced electron transfer (PET) from *p*-phenylenediamine

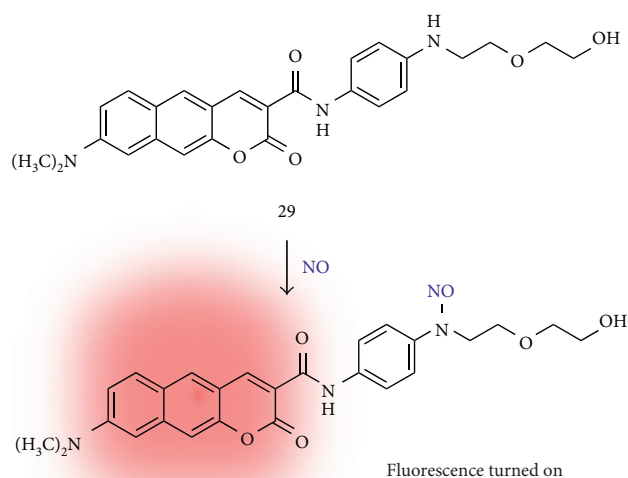


FIGURE 8: *N*-nitrosation-based benzo[*g*]coumarin probe for nitric oxide (NO) (**29**).

moiety and recovered by *N*-nitrosation reaction of NO. The sensitivity toward NO was verified in the screening with the other reactive species such as ClO^- , H_2O_2 , $^{\bullet}\text{OH}$, O_2^- , NO_2^- , and ONOO^- . The two-photon action cross section values were increased from 2.4 GM to 54 GM at 830 nm under the excitation at 760–900 nm after adding the NO species. The TPM imaging studies for the exogenous and endogenous NO detection were carried out in the live cells (HepG2 cell line), mouse brain tissue, and ischemia/reperfusion injury (IRI) mouse model. Higher fluorescence signals in the TPM images of the IRI model compared with the healthy control represent that NO probe can be applied as a practical tool for studying NO-related biological processes.

3.3.2. Hydrogen Sulfide (H_2S). Hydrogen sulfide is an endogenous gaseous transmitter along with carbon monoxide (CO) and nitric oxide (NO) [37]. Recent studies of H_2S revealed that it has a close relationship with neuronal activity, muscle relaxation, insulin management, inflammation, and aging [38]. Very recently, Ahn et al. reported a benzo[*g*]coumarin-based fluorescent probe for monitoring of exogenous and endogenous H_2S (**30**; Figure 9) [39]. The original fluorescence of the benzo[*g*]coumarin analogue (628 nm fluorescence emission at 485 nm excitation) was enhanced by Michael-type addition followed by aldol condensation of the α,β -unsaturated carbonyl group with H_2S [40]. Probe **30** shows the fast response (~ 8 min), high selectivity (negligible changes toward biological species), and high sensitivity (detection limit = $0.9 \mu\text{M}$) for H_2S . Bioimaging accessibility for the H_2S was verified by TPM cellular imaging in the HeLa cell line.

3.3.3. Hypochlorous Acid (HOCl). Hypochlorous acid is a kind of reactive oxygen species (ROS) [41], and the high level of HOCl is reported in several disorders such as cancer,

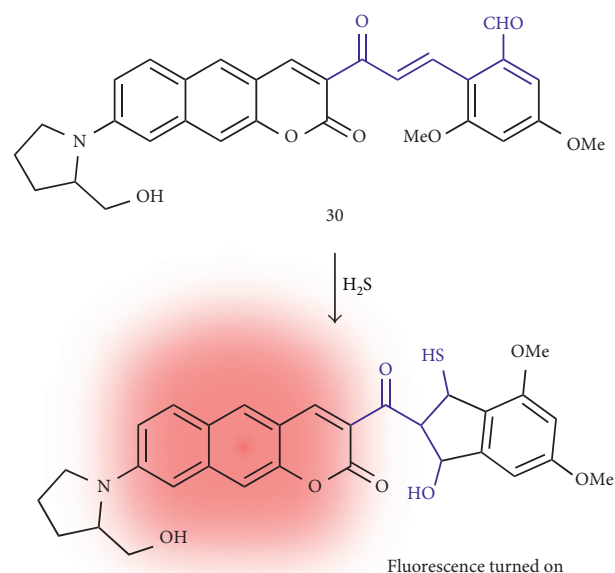


FIGURE 9: Michael addition and aldol condensation-based fluorescent probe for hydrogen sulfide (H_2S) (**30**).

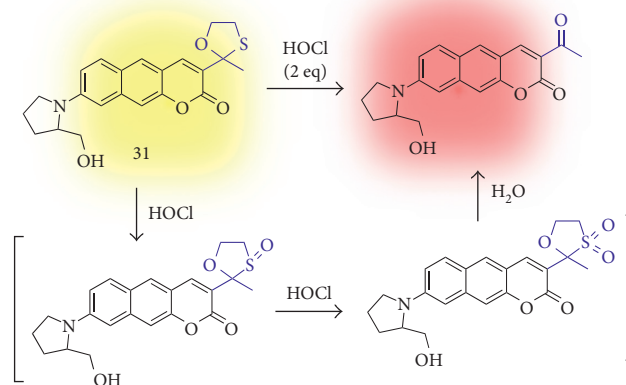


FIGURE 10: Oxathiolane deprotection-based fluorescent probe for hypochlorous acid (HOCl) (**31**).

arthritis, and neurodegenerative disease [42]. Therefore, monitoring the HOCl level and physiological distribution with a pathological mechanism is an important issue. However, the detection of endogenous HOCl is a challenging task due to the low biological concentration, a short lifetime, and a strong oxidizing property [43]. In 2017, Ahn et al. reported a benzo[*g*]coumarin-based ratiometric probe for endogenous HOCl imaging in live cells and tissues (**31**; Figure 10) [21]. An oxathiolane group is substituted at the electron-withdrawing position, and the deprotection into acetyl of this moiety by HOCl causes the intramolecular charge-transfer (ICT) character change of the benzo[*g*]coumarin dye in a ratiometric manner: emission maximum shift from 598 nm (with 424 nm absorption maximum) to 633 nm (with 598 nm absorption maximum). Probe **31** shows a low detection limit at the nanomolar level (34.8 nM) with high sensitivity toward HOCl over various reactive species

including H_2O_2 , $\cdot\text{OH}$, O_2^- , $^1\text{O}_2$, and reactive nitrogen species (RNS). The probe **31** and the reaction product give good two-photon action cross section values, 142 GM and 439 GM, respectively. The level of HOCl in the hippocampal slices of the mouse was analyzed by TPM ratiometric imaging with probe **31**, and the slightly higher concentration of HOCl was observed at the dentate gyrus (DG) which is linked to the cognitive ability and memory retention.

3.4. Sensing of Disease Biomarkers

3.4.1. Amyloid-Beta Plaque ($\text{A}\beta$ Plaque). Amyloid-beta plaque is an abnormal aggregate of the chemically sticky form of the amyloid-beta peptide (up to 42 or 43 amino acids long) that builds up between nerve cells in the AD patients [44, 45]. Therefore, the extracellular $\text{A}\beta$ plaque deposition in the brain is considered as a hallmark of AD. So far, various kinds of contrast agents have been developed for the diagnosis of AD by direct detection of plaques [46]: (i) magnetic resonance imaging (MRI), (ii) positron emission tomography (PET), (iii) single-photon emission computed tomography (SPECT), and (iv) fluorescence imaging. By using the benzo[*g*]coumarin analogue, Ahn et al. found out the selective $\text{A}\beta$ plaque staining ability of the iminobenzo[*g*]coumarin analogue (**24**) [47]. In this study, probe **24** selectively stains the $\text{A}\beta$ plaques including cerebral amyloid angiopathy (CAA) in the whole brain region successfully. Probe **24** is accumulated in the $\text{A}\beta$ plaques accompanying with significant fluorescence increments due to the nature of the donor-acceptor-type dye [48]; strong fluorescence in hydrophobic or viscous environment likes inside of the $\text{A}\beta$ plaque. The *in vivo* TPM deep tissue imaging of $\text{A}\beta$ plaques in the AD mouse model (5XFAD) treated with probe **24** via intraperitoneal injection shows the high blood-brain barrier (BBB) permeability of **24** and its superior deep tissue imaging ability (~ 600 nm depth) with high resolution.

3.4.2. Monoamine Oxidases (MAOs). Monoamine oxidases are a key enzyme responsible for the regulation of intracellular levels of biogenic amines and amine-based neurotransmitters such as dopamine, adrenaline, and serotonin [49]. A recent study revealed that suppressed or overregulated activity of MAOs is observed in several diseases including cancer and neurodegenerative diseases [50], AD, and Parkinson's disease (PD). In 2012, Ahn et al. developed a fluorescent probe (**32**) that can sense the activity of MAOs by enzymatic cleavage of the aminopropyl moiety followed by intramolecular cyclization and generation of an iminobenzo[*g*]coumarin (**24**) (Figure 11) [19]. In the intensive study, they applied probe **32** to find a correlation between activity of MAOs and AD progress in the animal model by using TPM [47]. Interestingly, significant background signal enhancement that correlated with MAO's activity was observed in older AD mice. The MAO's enzymatic product **24** is accumulated from the outside of $\text{A}\beta$ plaques to the inside, and the fluorescence intensity is increased as growing older (increased numbers and size of $\text{A}\beta$ plaques in the brain of the mouse model) (Figure 12). This is

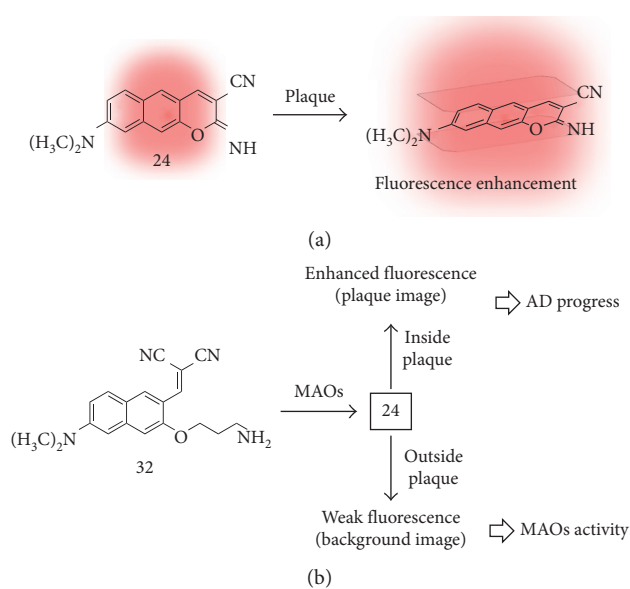


FIGURE 11: (a) Intercalation-based fluorescent probe for amyloid-beta plaque (**24**). (b) Amine oxidation-based fluorescent probe for monoamine oxidases (MAOs) activity in Alzheimer's disease (AD) (**32**).

the first demonstration for following activity of MAOs and AD progress *in vivo*.

3.5. Deep Tissue Imaging. The fluorescence tissue imaging has emerged as the strong tool for studying biological events and clinical applications. In particular, the fluorescence deep tissue imaging with high resolution offers collective information of the cellular processes in a macroscopic view. Among the various imaging techniques, TPM has shown superior performance for deep tissue imaging. However, a key limitation for TPM-based deep tissue imaging is the autofluorescence interference from intrinsic biomolecules in the tissue such as nicotinamide adenine dinucleotide (NADH) and its phosphate analogue (NADPH), riboflavin, and flavoproteins [22]. The autofluorescence issue when using the known two-photon absorbing dyes has been solved by technical methods such as tuning the excitation wavelength, reducing the laser power, and changing the detection channel and/or sensitivity.

To overcome this issue, Ahn et al. focused on the systematic study of the new two-photon absorbing dyes based on benzo[*g*]coumarin analogues. In 2017, they reported pyridyl/pyridinium-benzo[*g*]coumarin analogues which have far-red-emitting (585–691 nm) fluorescence (**33–42**; Figure 13; Table 2) [22]. They optimized the wavelength of benzo[*g*]coumarin analogues that can address the autofluorescence issue. The pyridinium group at electron-withdrawing position (C-3) makes the significant wavelength shift to the far-red region (660–691 nm) from the parent benzo[*g*]coumarin or pyridyl-benzo[*g*]coumarin. In the brain tissue imaging with Py + BC690 (**42**), the clear deep tissue TPM imaging after an optical clearing process (BABB clearing) [51] was observed at the stage down to 1380 nm

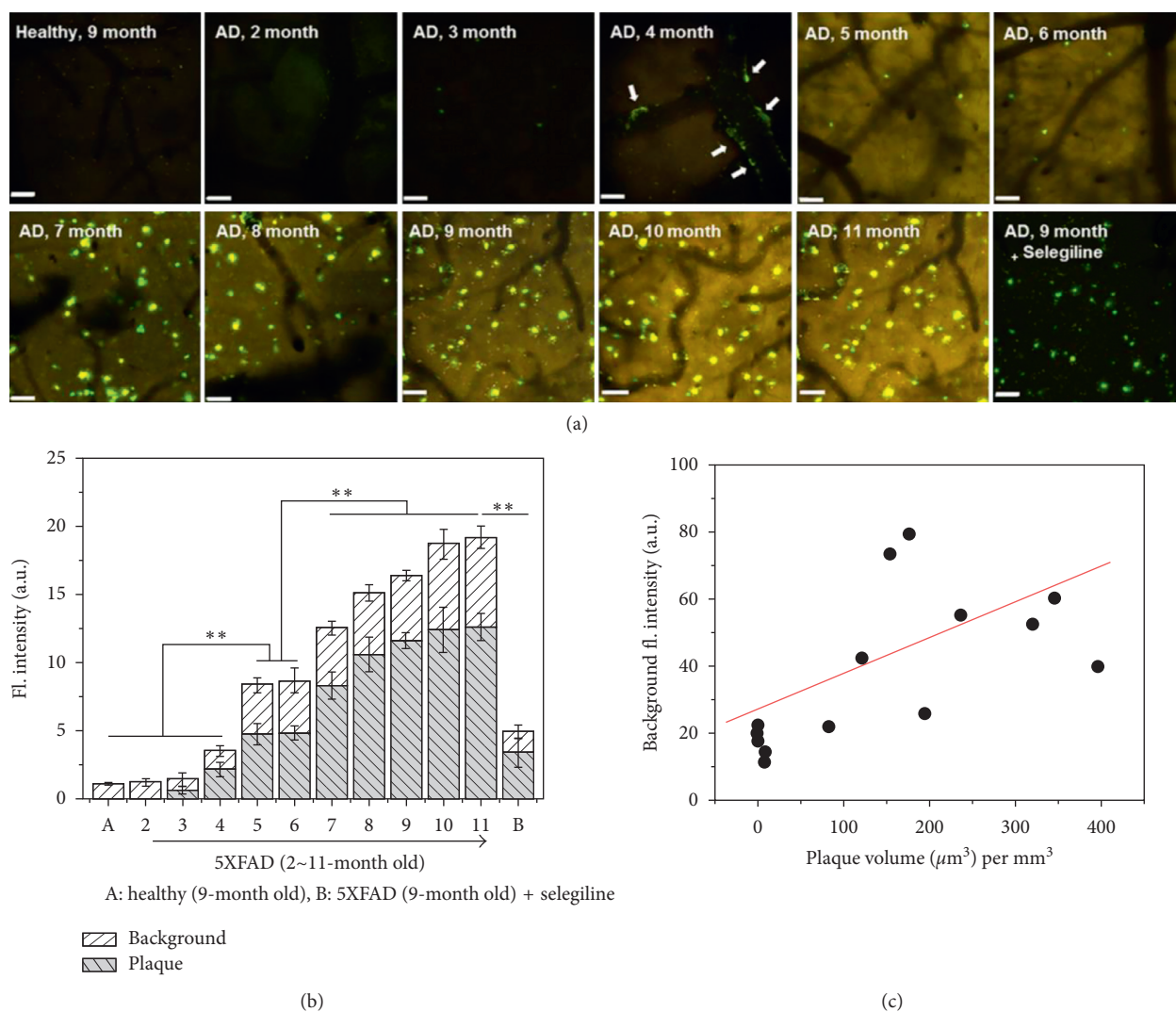


FIGURE 12: *In vivo* TPM coimaging of MAO activity and A β plaques using probe **32**. (a) *In vivo* fluorescence images (from (z)-stack, magnified 20x) of the frontal cortex region of transgenic and healthy mice, obtained after intraperitoneal injection of probe **32**. The scale bar is 60 μm . The images were acquired at 200–300 μm depth from the surface of the cortex. (b) Plots of the average fluorescence intensity of A β plaques and background images in (a), respectively. (c) A plot of the background fluorescence intensity versus the plaque volume (μm^3 per mm^3). ** p -value < 0.01. Reproduced from [43] with permission from the American Chemical Society, copyright 2016.

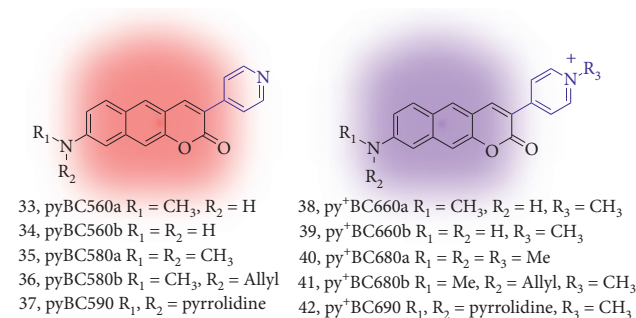


FIGURE 13: Red/far-red-emitting pyridinium-benzo[*g*]coumarin derivatives (33–42).

depth. The imaging depth indicated the high tissue uptake of dye and penetration ability of **42** which are important features as a bioimaging agent.

TABLE 2: Photophysical properties of pyridinium-benzo[*g*]coumarin derivatives (33–42).

Compound	λ_{abs} (nm)	λ_{emi} (nm)	Brightness	GM
33	n.r.	n.r.	n.r.	n.r.
34	n.r.	n.r.	n.r.	n.r.
35	445	585	n.r.	n.r.
36	n.r.	n.r.	n.r.	n.r.
37	n.r.	n.r.	n.r.	n.r.
38	506	663	749	n.d.
39	499	660	510	n.d.
40	513	681	2089	n.d.
41	511	680	1173	150
42	527	691	799	160

The wavelengths, brightness, and GM values are derived from the highest intensity values in the absorption and fluorescence emission spectra. Brightness: molar extinction coefficient ($\text{LMol}^{-1}\cdot\text{cm}^{-1}$) \times quantum yield (Φ_{F}); GM: two-photon absorption cross section (TPACS, Goepfert-Mayer unit); n.r.: not reported; n.d.: not determined.

4. Summary and Outlook

Since the first report about the pi-extended structure of coumarin, the tremendous knowledge and experimental results have been accumulated. In this focused review, the basic photophysical property, synthetic method, and applications of benzo[*g*]coumarin analogues are summarized. Molecular structures of linearly pi-extended benzo[*g*]coumarin analogues are expected to provide a longer excitation and emission wavelength at the red/near-infrared region with larger two-photon absorbing ability, and the experiment results have given evidences. In addition, their rigid conformation with facile function granting serves the high quantum yield, superior photostability/chemical stability, and applicability for the development of molecular probes. Some of the benzo[*g*]coumarin analogues showed promising two-photon absorbing properties holding great promise in the development of two-photon bioimaging probes to sense biologically important species. Most of the bioimaging applications of benzo[*g*]coumarin analogues are carried out very recently; therefore, we hope that this review inspires scientists to develop more advanced systems with useful practical applications such as disease biomarker sensing for prognosis and diagnosis.

Conflicts of Interest

The authors declare that there are no conflicts of interest.

Acknowledgments

This work was supported by a grant from the Kyung Hee University in 2017 (KHU-20170857).

References

- [1] S. M. Sethna and N. M. Shah, "The chemistry of coumarins," *Chemical Reviews*, vol. 36, no. 1, pp. 1–62, 1945.
- [2] A. Thakur, R. Singla, and V. Jaitak, "Coumarins as anticancer agents: a review on synthetic strategies, mechanism of action and SAR studies," *European Journal of Medicinal Chemistry*, vol. 101, pp. 476–495, 2015.
- [3] X. Chen, F. Wang, J. Y. Hyun et al., "Recent progress in the development of fluorescent, luminescent and colorimetric probes for detection of reactive oxygen and nitrogen species," *Chemical Society Reviews*, vol. 45, no. 10, pp. 2976–3016, 2016.
- [4] M. H. Lee, A. Sharma, M. J. Chang et al., "Fluorogenic reaction-based prodrug conjugates as targeted cancer theranostics," *Chemical Society Reviews*, vol. 47, no. 1, pp. 28–52, 2018.
- [5] J. Wu, W. Liu, J. Ge, H. Zhang, and P. Wang, "New sensing mechanisms for design of fluorescent chemosensors emerging in recent years," *Chemical Society Reviews*, vol. 40, no. 7, pp. 3483–3495, 2011.
- [6] S. R. Trenor, A. R. Shultz, B. J. Love, and T. E. Long, "Coumarins in polymers: from light harvesting to photo-cross-linkable tissue scaffolds," *Chemical Reviews*, vol. 104, no. 6, pp. 3059–3078, 2004.
- [7] M. Tasiar, D. Kim, S. Singha, M. Krzeszewski, K. H. Ahn, and D.T. Gryko, " π -expanded coumarins: synthesis, optical properties and applications," *Journal of Materials Chemistry C*, vol. 3, no. 7, pp. 1421–1446, 2015.
- [8] Z. Yang, J. Cao, Y. He et al., "Macro-/micro-environment-sensitive chemosensing and biological imaging," *Chemical Society Reviews*, vol. 43, no. 13, pp. 4563–4601, 2014.
- [9] G. Jones, S. F. Griffin, C. Y. Choi, and W. R. Bergmark, "Electron donor-acceptor quenching and photoinduced electron transfer for coumarin dyes," *Journal of Organic Chemistry*, vol. 49, no. 15, pp. 2705–2708, 1984.
- [10] H. M. Kim and B. R. Cho, "Small-molecule two-photon probes for bioimaging applications," *Chemical Reviews*, vol. 115, no. 11, pp. 5014–5055, 2015.
- [11] J. Chen, W. Liu, B. Zhou et al., "Coumarin- and rhodamine-fused deep red fluorescent dyes: synthesis, photophysical properties, and bioimaging in vitro," *Journal of Organic Chemistry*, vol. 78, no. 12, pp. 6121–6130, 2013.
- [12] D. Kim, Q. P. Xuan, H. Moon, Y. W. Jun, and K. H. Ahn, "Synthesis of benzocoumarins and characterization of their photophysical properties," *Asian Journal of Organic Chemistry*, vol. 3, no. 10, pp. 1089–1096, 2014.
- [13] C. Murata, T. Masuda, Y. Kamochi et al., "Improvement of fluorescence characteristics of coumarins: syntheses and fluorescence properties of 6-methoxycoumarin and benzocoumarin derivatives as novel fluorophores emitting in the longer wavelength region and their application to analytical reagents," *Chemical and Pharmaceutical Bulletin*, vol. 53, no. 7, pp. 750–758, 2005.
- [14] J. A. Key, S. Koh, Q. K. Timerghazin, A. Brown, and C. W. Cairo, "Photophysical characterization of triazole-substituted coumarin fluorophores," *Dyes and Pigments*, vol. 82, no. 2, pp. 196–203, 2009.
- [15] I. Kim, D. Kim, S. Sambasivan, and K. H. Ahn, "Synthesis of π -extended coumarins and evaluation of their precursors as reactive fluorescent probes for mercury ions," *Asian Journal of Organic Chemistry*, vol. 1, no. 1, pp. 60–64, 2012.
- [16] A. R. Sarkar, C. H. Heo, L. Xu et al., "A ratiometric two-photon probe for quantitative imaging of mitochondrial pH values," *Chemical Science*, vol. 7, no. 1, pp. 766–773, 2016.
- [17] A. R. Sarkar, C. H. Heo, H. W. Lee, K. H. Park, Y. H. Suh, and H. M. Kim, "Red emissive two-photon probe for real-time imaging of mitochondria trafficking," *Analytical Chemistry*, vol. 86, no. 12, pp. 5638–5641, 2014.
- [18] Z. Mao, H. Jiang, Z. Li, C. Zhong, W. Zhang, and Z. Liu, "An *N*-nitrosation reactivity-based two-photon fluorescent probe for the specific in situ detection of nitric oxide," *Chemical Science*, vol. 8, no. 6, pp. 4533–4538, 2017.
- [19] D. Kim, S. Sambasivan, H. Nam et al., "Reaction-based two-photon probes for in vitro analysis and cellular imaging of monoamine oxidase activity," *Chemical Communications*, vol. 48, no. 54, pp. 6833–6835, 2012.
- [20] T. Schwarze, H. Müller, D. Schmidt, J. Riemer, and H.-J. Holdt, "Design of Na⁺-selective fluorescent probes: a systematic study of the Na⁺-complex stability and the Na⁺/K⁺-selectivity in acetonitrile and water," *Chemistry—A European Journal*, vol. 23, no. 30, pp. 7255–7263, 2017.
- [21] Y. W. Jun, S. Sarkar, S. Singha et al., "A two-photon fluorescent probe for ratiometric imaging of endogenous hypochlorous acid in live cells and tissues," *Chemical Communications*, vol. 53, no. 78, pp. 10800–10803, 2017.
- [22] Y. W. Jun, H. R. Kim, Y. J. Reo, M. Dai, and K. H. Ahn, "Addressing the autofluorescence issue in deep tissue imaging by two-photon microscopy: the significance of far-red emitting dyes," *Chemical Science*, vol. 8, no. 11, pp. 7696–7704, 2017.
- [23] J. Chan, S. C. Dodani, and C. J. Chang, "Reaction-based small-molecule fluorescent probes for chemoselective bioimaging," *Nature Chemistry*, vol. 4, no. 4, pp. 973–984, 2012.

- [24] W. Denk, J. Strickler, and W. Webb, "Two-photon laser scanning fluorescence microscopy," *Science*, vol. 248, no. 4951, pp. 73–76, 1990.
- [25] D. J. Waggoner, T. B. Bartnikas, and J. D. Gitlin, "The role of copper in neurodegenerative disease," *Neurobiology of Disease*, vol. 6, no. 4, pp. 221–230, 1999.
- [26] M. G. Savelieff, S. Lee, Y. Liu, and M. H. Lim, "Untangling amyloid- β , tau, and metals in Alzheimer's disease," *ACS Chemical Biology*, vol. 8, no. 5, pp. 856–865, 2013.
- [27] D. E. Kang, C. S. Lim, J. Y. Kim, E. S. Kim, H. J. Chun, and B. R. Cho, "Two-photon probe for Cu^{2+} with an internal reference: quantitative estimation of Cu^{2+} in human tissues by two-photon microscopy," *Analytical Chemistry*, vol. 86, no. 11, pp. 5353–5359, 2014.
- [28] E. Murphy and D. A. Eisner, "Regulation of intracellular and mitochondrial sodium in health and disease," *Circulation Research*, vol. 104, no. 3, pp. 292–303, 2009.
- [29] D. Landowne, "Movement of sodium ions associated with the nerve impulse," *Nature*, vol. 242, no. 5398, pp. 457–459, 1973.
- [30] H. N. Kim, W. X. Ren, J. S. Kim, and J. Yoon, "Fluorescent and colorimetric sensors for detection of lead, cadmium, and mercury ions," *Chemical Society Reviews*, vol. 41, no. 8, pp. 3210–3244, 2012.
- [31] M. Cametti and K. Rissanen, "Highlights on contemporary recognition and sensing of fluoride anion in solution and in the solid state," *Chemical Society Reviews*, vol. 42, no. 5, pp. 2016–2038, 2013.
- [32] D. Kim, S. Singha, T. Wang et al., "In vivo two-photon fluorescent imaging of fluoride with a desilylation-based reactive probe," *Chemical Communications*, vol. 48, no. 82, pp. 10243–10245, 2012.
- [33] C. P. Baines, "The cardiac mitochondrion: nexus of stress," *Annual Review of Physiology*, vol. 72, no. 1, pp. 61–80, 2010.
- [34] J. Santo-Domingo and N. Demareux, "The renaissance of mitochondrial pH," *Journal of General Physiology*, vol. 139, no. 6, pp. 415–423, 2012.
- [35] V. Calabrese, C. Mancuso, M. Calvani, E. Rizzarelli, D. A. Butterfield, and A. M. Giuffrida Stella, "Nitric oxide in the central nervous system: neuroprotection versus neurotoxicity," *Nature Reviews Neuroscience*, vol. 8, no. 10, pp. 766–775, 2007.
- [36] C. Szabo, "Gasotransmitters in cancer: from pathophysiology to experimental therapy," *Nature Reviews Drug Discovery*, vol. 15, no. 3, pp. 185–203, 2015.
- [37] R. Wang, "Hydrogen sulfide: the third gasotransmitter in biology and medicine," *Antioxidants and Redox Signaling*, vol. 12, no. 9, pp. 1061–1064, 2010.
- [38] L. Li, P. Rose, and P. K. Moore, "Hydrogen sulfide and cell signaling," *Annual Review of Pharmacology and Toxicology*, vol. 51, no. 1, pp. 169–187, 2011.
- [39] H. G. Ryu, S. Singha, Y. W. Jun, Y. J. Reo, and K. H. Ahn, "Two-photon fluorescent probe for hydrogen sulfide based on a red-emitting benzocoumarin dye," *Tetrahedron Letters*, vol. 59, no. 1, pp. 49–53, 2018.
- [40] S. Singha, D. Kim, H. Moon et al., "Toward a selective, sensitive, fast-responsive, and biocompatible two-photon probe for hydrogen sulfide in live cells," *Analytical Chemistry*, vol. 87, no. 2, pp. 1188–1195, 2015.
- [41] S. J. Klebanoff, "Myeloperoxidase: friend and foe," *Journal of Leukocyte Biology*, vol. 77, no. 5, pp. 598–625, 2005.
- [42] O. M. Panasenko, I. V. Gorudko, and A. V. Sokolov, "Hypochlorous acid as a precursor of free radicals in living systems," *Biochemistry*, vol. 78, no. 13, pp. 1466–1489, 2013.
- [43] Y. Yue, F. Huo, C. Yin, J. O. Escobedo, and R. M. Strongin, "Recent progress in chromogenic and fluorogenic chemosensors for hypochlorous acid," *Analyst*, vol. 141, no. 6, pp. 1859–1873, 2016.
- [44] D. J. Selkoe and J. Hardy, "The amyloid hypothesis of Alzheimer's disease at 25 years," *EMBO Molecular Medicine*, vol. 8, no. 6, pp. 595–608, 2016.
- [45] P. Lewczuk, B. Mroczko, A. Fagan, and J. Kornhuber, "Biomarkers of Alzheimer's disease and mild cognitive impairment: a current perspective," *Advances in Medical Sciences*, vol. 60, no. 1, pp. 76–82, 2015.
- [46] V. L. Villemagne, V. Doré, S. C. Burnham, C. L. Masters, and C. C. Rowe, "Imaging tau and amyloid- β proteinopathies in Alzheimer disease and other conditions," *Nature Reviews Neurology*, vol. 14, no. 4, pp. 225–236, 2018.
- [47] D. Kim, S. H. Baik, S. Kang et al., "Close correlation of monoamine oxidase activity with progress of Alzheimer's disease in mice, observed by in vivo two-photon imaging," *ACS Central Science*, vol. 2, no. 12, pp. 967–975, 2016.
- [48] D. Kim, H. Moon, S. H. Baik et al., "Two-photon absorbing dyes with minimal autofluorescence in tissue imaging: application to in vivo imaging of amyloid- β plaques with a negligible background signal," *Journal of the American Chemical Society*, vol. 137, no. 21, pp. 6781–6789, 2015.
- [49] D. E. Edmondson, C. Binda, J. Wang, A. K. Upadhyay, and A. Mattevi, "Molecular and mechanistic properties of the membrane-bound mitochondrial monoamine oxidases," *Biochemistry*, vol. 48, no. 20, pp. 4220–4230, 2009.
- [50] M. B. H. Youdim, D. Edmondson, and K. F. Tipton, "The therapeutic potential of monoamine oxidase inhibitors," *Nature Reviews Neuroscience*, vol. 7, no. 4, pp. 295–309, 2006.
- [51] H.-U. Dodt, U. Leischner, A. Schierloh et al., "Ultra-microscopy: three-dimensional visualization of neuronal networks in the whole mouse brain," *Nature Methods*, vol. 4, no. 4, pp. 331–336, 2007.

Research Article

Sensing of Vascular Permeability in Inflamed Vessel of Live Animal

Sang A Park, Soi Jeong , Young Ho Choe , and Young-Min Hyun 

Department of Anatomy and Brain Korea 21 PLUS Project for Medical Science, Yonsei University College of Medicine, Seoul 03722, Republic of Korea

Correspondence should be addressed to Young-Min Hyun; ymhyun@yuhs.ac

Received 25 January 2018; Accepted 15 March 2018; Published 15 May 2018

Academic Editor: Dokyoung Kim

Copyright © 2018 Sang A Park et al. This is an open access article distributed under the Creative Commons Attribution License, which permits unrestricted use, distribution, and reproduction in any medium, provided the original work is properly cited.

Increase in vascular permeability is a conclusive response in the progress of inflammation. Under controlled conditions, leukocytes are known to migrate across the vascular barriers to the sites of inflammation without severe vascular rupture. However, when inflammatory state becomes excessive, the leakage of blood components may occur and can be lethal. Basically, vascular permeability can be analyzed based on the intensity of blood outflow. To evaluate the amount and rate of leakage in live mice, we performed cremaster muscle exteriorization to visualize blood flow and neutrophil migration. Using two-photon intravital microscopy of the exteriorized cremaster muscle venules, we found that vascular barrier function is transiently and locally disrupted in the early stage of inflammatory condition induced by N-formylmethionyl-leucyl-phenylalanine (fMLP). Measurement of the concentration of intravenously (i.v.) injected Texas Red dextran inside and outside the vessels resulted in clear visualization of real-time increases in transient and local vascular permeability increase in real-time manner. We successfully demonstrated repeated leakage from a target site on a blood vessel in association with increasing severity of inflammation. Therefore, compared to other methods, two-photon intravital microscopy more accurately visualizes and quantifies vascular permeability even in a small part of blood vessels in live animals in real time.

1. Introduction

Control of vascular permeability allows leukocyte migration, provides nutrition, and maintains homeostasis of the body [1]. Due to its importance, therefore, vascular permeability has been actively investigated in the field of medical science [2–4]. Various stimuli act on endothelial cells and adjust the tightness of the vascular barrier by remodeling actins [3]. VE-cadherin, which is only expressed in the epithelial cell, and JAM-1 are key factors in vascular hemostasis and angiogenesis [5, 6]. Metastasis of cancer cells is strongly associated with vascular integrity since a highly permeable endothelial barrier induces angiogenesis, which eventually supports the dissemination of tumor cells [7–9]. Despite numerous studies, detailed steps of controlling mechanisms about vascular permeability have not been uncovered.

Therefore, we prepared cremaster muscle of mice in order to observe the changes in vascular integrity in acute inflammatory conditions. The cremaster muscle was treated with bacterial chemoattractant, fMLP, and two-photon intravital imaging of cremaster muscle venules was conducted for more than 3 hours. fMLP was used to recruit neutrophils along the cremaster vessels [10, 11]. The major premise of this study was that neutrophils activated by fMLP would increase the secretion of vascular endothelial growth factor A (VEGF-A); therefore, vascular integrity would be decreased by cytoskeletal contraction [2, 12]. We were able to detect increased vascular permeability with this methodology; we analyzed the characteristics of this phenomenon by comparing several targeted locations on inflamed vessels. Morphological changes in leukocytes and the intensity of blood flow were also evaluated.

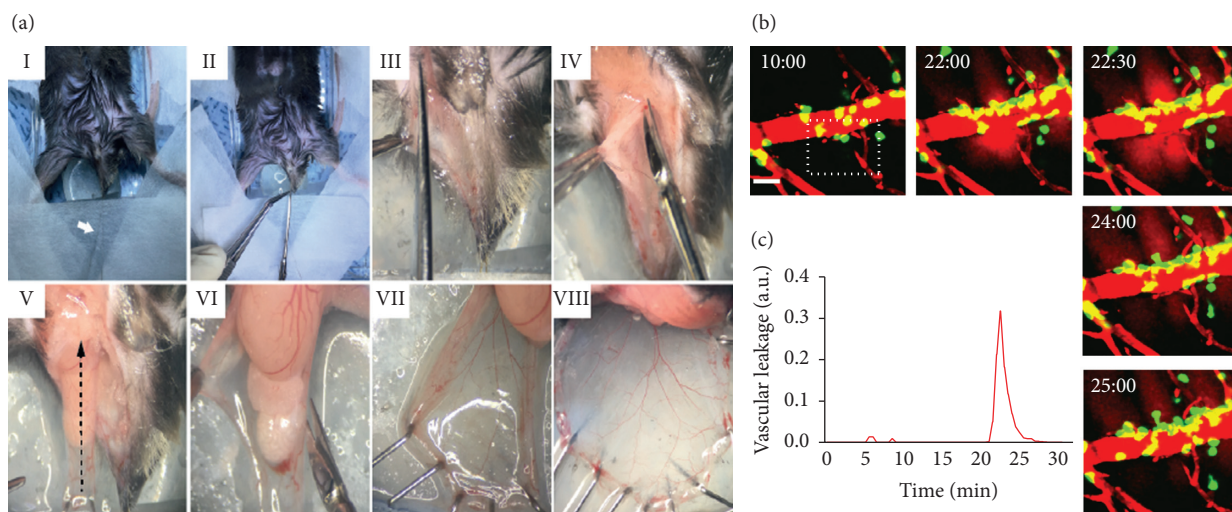


FIGURE 1: Cremaster surgery and intravital imaging of inflamed cremaster vessel. (a) (I) The body of the mouse was fixed in a chamber, using surgical tape, with traction on the scrotum using suture thread. (II) The scrotum was cut with scissors after filling the chamber with sterile 1x PBS. (III) The epidermis in the scrotum was cut along its edge. (b, c) Changes in vessel permeability with time (min) were observed using intravital imaging. Vascular leakage was measured as an arbitrary unit. An intact vessel with zero leakage was set as the baseline for this unit. A graph of vascular leakage shows local and transient increase in blood permeability. Scale bar: $30\ \mu\text{m}$. See Video 1.

2. Materials and Methods

2.1. Mice. LysM-GFP mice were used for two-photon intravital imaging [13, 14]. The animal and experimental facilities were located at Yonsei University College of Medicine's specific pathogen-free zone. Only heterogenous mice (GFP/+) were used for experiments. The institutional review board of Yonsei University College of Medicine approved the study.

2.2. Cremaster Exteriorization for Intravital Imaging. The mouse cremaster muscle was chosen for intravital imaging, as it can be locally stimulated by exposure to fMLP after exteriorization [10]. Mice were anesthetized with a Zoletil and Rompun mixture (3:2) via intramuscular injection (10 mg/kg). Texas Red dextran was injected via i.v. injection in order to label the blood flow. After a few seconds, mice were placed on the cremaster imaging chamber and firmly fixed with surgical tape. Body hair was removed with a razor and shaving cream along the scrotum and testes. The upper skin of the scrotal sac was retracted with forceps and secured with insect pins. After this procedure, the mouse skin was ready for exposure. From this point, 1x phosphate-buffered saline (PBS) preheated to around $34\text{--}35^\circ\text{C}$ was always running inside the chamber sink in order to maintain the temperature and humidity of the cremaster tissue. Attachment of a yellow tip to the PBS tube was useful for continuous water irrigation. Under stereoscopic microscopy, the ventral surface of the pinned scrotal sac was incised. The testicle was removed through the sac with mild pressure on the abdominal cavity. Connective tissues between the scrotal skin and cremaster muscle were gently detached, and the separated scrotal skin was everted to avoid disturbing the cremaster muscle preparation. Finally, the cremaster muscle was gently spread on the silicone bed with several pins. Before imaging, the prepared cremaster muscle was washed

once again with preheated 1x PBS in order to obtain a clear view.

2.3. Two-Photon Intravital Imaging of Inflamed Cremaster Muscle Venules. After cremaster surgery, vessel inflammation was induced with drops of fMLP ($1\ \mu\text{M}$). Multiphoton microscopy (LSM 7 MP; Zeiss) with two-photon excitation (3 colors: blue, green, and red. Each of the three channels has an emission wavelength of 420–475 nm, 500–550 nm, and 565–610 nm.) was used at a wavelength of 880–900 nm. Second harmonic generation was represented by blue, and Texas Red dextran and neutrophils were visualized with red and green, respectively. MaiTai Deep See laser system (Spectra-Physics) which detects wavelengths from 690 to 1040 nm was used for excitation. Video resolution was fixed at 512×512 pixels.

2.4. Vascular Permeability Analysis. Vascular permeability or leakage was measured using an arbitrary unit, a.u. An intact vessel with zero leakage was set as the baseline for this unit (Figure 1). Absolute values were used to represent intensity in % and blood leakage volumes (Figures 2 and 3).

2.5. Imaging Data Analysis. ZEN operating software (Carl Zeiss) was used for operating software of two-photon microscope and data gathering. Volocity (PerkinElmer) was used for tracking of neutrophils and vascular permeability. Graphs were drawn using Prism Software (GraphPad).

3. Results

3.1. Angiorrhhexis Is a Local and Transient Event throughout a Blood Vessel during Inflammation. fMLP is a bacterial chemoattractant used to induce an inflammatory state, in which neutrophils infiltrate across blood vessels in damaged or infected interstitium; this may induce vascular disruption

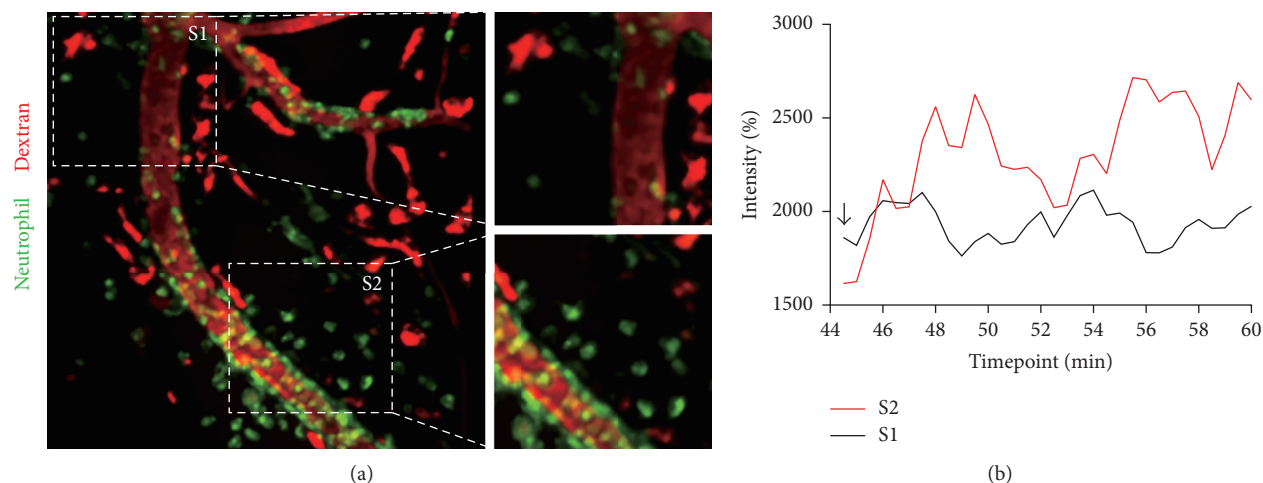


FIGURE 2: Vascular leakage occurs at specific sites on a vessel despite uniform fMLP treatment. (a) Blood vessels are visualized with dextran, and neutrophils appear green on the image. When fMLP was used to activate neutrophils, the site of leakage was designated as S2 and the area where leakage did not occur was designated as S1 in the same blood vessel (blood leakage occurred at S2, with no apparent change in S1). Scale bar: $30\ \mu\text{m}$. See Video 2. (b) When leakage occurred at S1 and S2, blood was extruded and the intensity of red was increased. The graphical display compares the intensity at two areas at 44 to 60 min in Video 2. At the time of initial imaging (arrow), the intensity of S1 is higher than that of S2 because the background becomes reddish as overlap occurs due to motion during *in vivo* imaging. Graph B shows the percent intensity (%) of blood flow in the two areas, as measured by the leakage of dextran.

[15–17]. The mouse cremaster muscle was prepared for this experiment since a few drops of fMLP can be directly applied to induce vascular inflammation (Figure 1(a)). We hypothesized that fMLP-induced inflammation would lead to neutrophil infiltration and disruption of the vascular barrier in whole blood vessels. However, when fMLP was evenly applied to the exteriorized cremaster muscle, vascular leakage only increased in part of the blood vessel (Figure 1(b) and Video 1). Thus, disruption did not develop simultaneously in the entire inflamed vessel. On the contrary, vascular leakage occurred locally, and the intensity varied significantly between intact and damaged vessel walls (Figure 1(c)). In addition, neutrophil recruitment was only observed near the site of vessel wall disruption (S2 in Figure 2(a) and Video 2), and only a few neutrophils were detected near the intact vessel structures (S1 in Figure 2(a) and Video 2). Interestingly, neutrophils in S2 were attached in a row at the outer surface of the weakened vessel, as if supporting the unstable membrane. Comparison of S1 and S2 clearly showed differences in inflammation progression. Indeed, the change in background intensity, namely, the black space in Figure 2(a), showed that blood leakage was more intense at S2 than at S1 (Figure 2(b)). Therefore, even though it is known that neutrophil infiltration does not coincide with vascular leakage at the same site in a blood vessel [18, 19], neutrophil adhesion to the abluminal side could induce vascular leakage at a delayed time point following infiltration at the same site. As intravital time-lapse imaging was performed in live animals, shaking occasionally occurred during image capture. This could cause cremaster muscle contraction and negligible variation in Texas Red intensity, as indicated by the arrow in S1 in Figure 2(b).

3.2. Repetitive and Transient Leakage Occurs at a Consistent Point on the Inflamed Blood Vessel. Vascular leakage is

a transient and local event in the blood vessel under inflammation. Thus, a point on the stimulated vessel can be more rapidly disrupted than another site on the same stimulated vessel, as shown in Figures 1(b) and 2(a). After detection of vascular leakage at a vulnerable point on the inflamed vessel (S2 in Figure 2(a)), we further tracked the target area to quantify blood outflow using a rainbow scale. The principle of the rainbow scale is similar to that of the contour line; when the rate of leakage is high, the area appears red. Areas with relatively low rates of leakage appear blue to green. From the rainbow scale-based tracking of S2, we observed that there were two separate disruptive events at the same site on the vessel (Figure 3(a)). A period of mild vascular leakage was observed at one site, with outflow of about $75\ \mu\text{m}^3$ of dextran at peak for 48–50 min. Once outflow began, the Texas Red dextran quickly and widely spread across the interstitial area and became undetectable on two-photon intravital imaging. Interestingly, after an interval of 5 min, another more significant leakage event occurred at the same site on the blood vessel. The peak volume of the second leakage event reached $180\ \mu\text{m}^3$ (Figure 3(b)). Based on the graphical display of vascular leakage, blood was suddenly extruded from this particular site on the vessel, and the second extrusion phase was more significant than the first. Thus, leakage from inflamed vasculature is a discontinuous event and may repeatedly occur depending on the progress of inflammation. Therefore, our data verified that two-photon intravital microscopy can be used as a precise tool for research on leakage at an individual vascular level.

4. Discussion

Traditional *in vitro* methodologies used to study vascular permeability include measurement of hydraulic

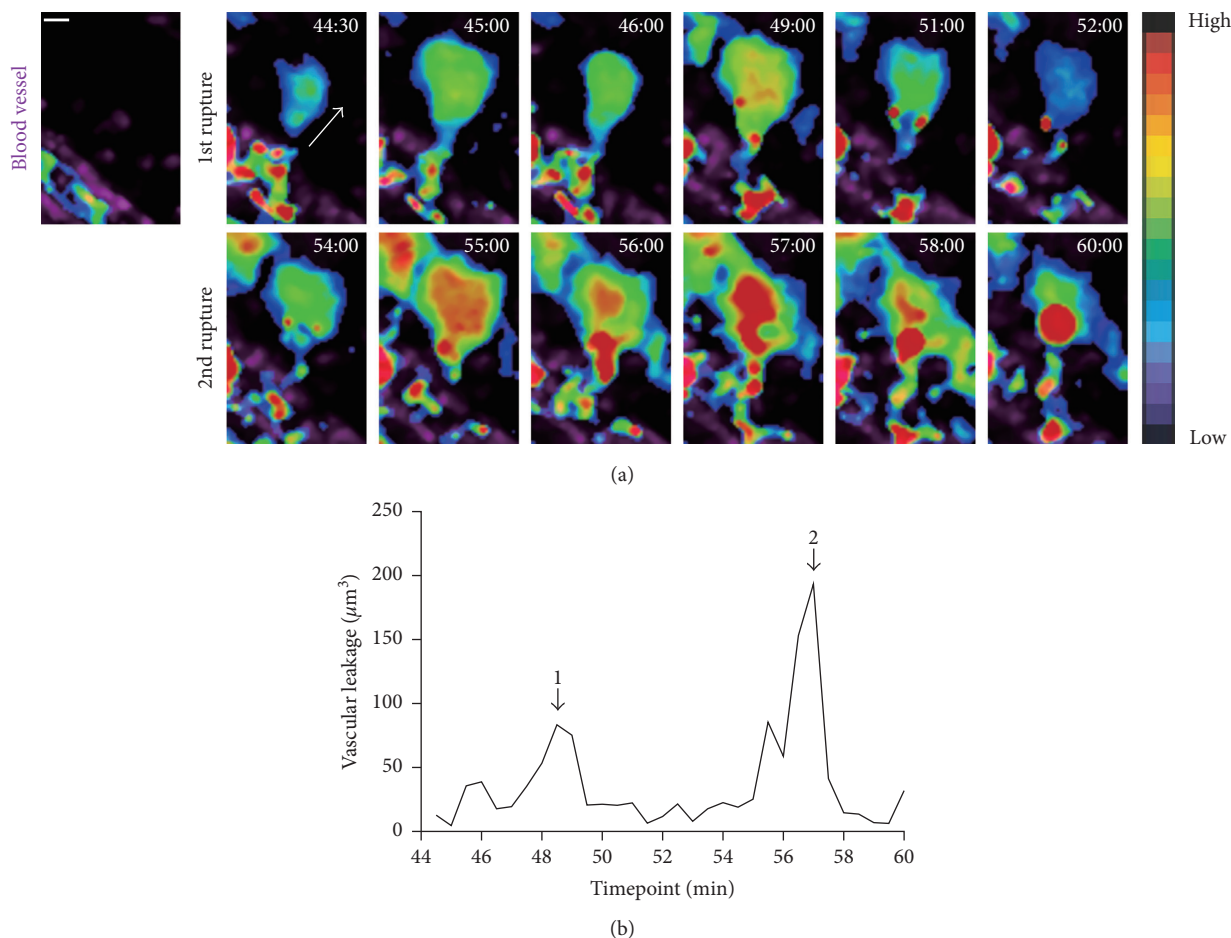


FIGURE 3: Leakage occurs in a repetitive and consistent manner. (a) The first image without blood leakage in S2 was set as a control condition. Color change shows the amount of leakage. Vessels appear magenta and blood flow is seen with rainbow colors. It is apparent that two disruptive events occurred within 16 min. A much greater amount of leakage was observed during the second disruptive event. (b) Vascular permeability was visually demonstrated, and the graph quantitatively shows about twice as much leakage. The graphical display is consistent with transient leakage from the same site. Endothelial barrier disruption did not always result in leakage. Two arrows in the figure indicate that leakage has occurred. Graph B shows the volume of leakage measured according to site. Scale bar: 10 μm .

conductivity, transendothelial electrical resistance, and albumin transport [20]. However, these techniques are inadequate for replication of actual vascular condition and disease models. In addition to the methods described above, a human microvascular endothelial cell (hMVEC) assay is used to reproduce an actual microvascular environment. With this hMVEC assay system, scientists can directly apply cytokines and growth factors such as interleukin-8 and VEGF to induce inflammatory conditions that are similar to an *in vivo* setting [21]. However, it is important to note that almost every *in vitro* experiment shows greater permeability levels compared to *in vivo* trials [20]. *In vitro* studies are performed under precisely controlled conditions, whereas *in vivo* studies are always affected by complicated and confounding factors.

Vascular permeability assays *in vivo* using Evans blue dye can be useful in overcoming the limitation of cellular and membrane-based experiments. Intravenous injection of Evans blue, a dye that binds to albumin, will circulate throughout the animal body. Due to the impermeability of the endothelium to

albumin, Evans blue should remain inside the liver in the control animal [22]. However, when vascular permeability is increased with inflammatory stimulation, leakage of Evans blue will be detected around affected vessels and organs. For example, Han et al. [23] were able to prove that angioedema is mediated by bradykinin via Bk2R by comparing the intensity of Evans blue concentration in the digested mouse ear and intestinal tissues. A vascular permeability assay, however, cannot directly show real-time leakage of blood. Combining our cremaster fluorescence analysis and Evans blue dye assay may compensate for the shortcomings of these methods.

In this study, we performed two-photon intravital microscopy to measure how vascular leakage occurs at the subvascular level under fMLP-induced inflammatory conditions. The cremaster muscle is useful for intravital fluorescent imaging since it can be easily exteriorized and is transparent. We investigated how blood vessels are disrupted and vascular leakage occurs during acute inflammation in correlation with neutrophil infiltration. Therefore, we used LysM-GFP mice, in which neutrophils were clearly

visualized by detection of green fluorescence following intravenous injection of Texas Red dextran (70 kDa). Texas Red dextran demonstrates a green color in the absence of bleeding, with use of a long wavelength laser (880–900 nm). This wavelength rarely induces tissue phototoxicity or photobleaching. Thus, it was possible to perform intravital imaging at the same site for up to several hours without severe photo-induced damage. When injected, dextran circulates within and clearly outlines the vasculature. Therefore, Texas Red leakage is a marker of vascular disruption. We locally induced an acute inflammatory state by treatment of the exteriorized mouse cremaster muscle with fMLP. As precise two-photon intravital imaging detects the concentration of Texas Red dextran inside and outside blood vessels, we were able to visualize how leakage occurs from any site on a blood vessel in a living animal. Therefore, this intravital imaging method enables more accurate assessment of vascular leakage in terms of time and location. As shown in our data, vascular leakage is a local and transient event in a blood vessel during acute inflammation. Use of intravital imaging to visualize leakage of intravascular components under inflammatory conditions makes it possible to detect subvascular level disruption of the blood vessel in the target organ. In combination with further research on signaling mechanisms such as cytokine interactions among cells and receptors, this fluorescent intravital approach can provide essential information for development of therapeutic methods for diseases associated with blood vessel malfunction.

Data Availability

The data used to support the findings of this study are available from the corresponding author upon request.

Disclosure

Sang A Park is currently working at the School of Medicine, CHA University, Seongnam, Republic of Korea.

Conflicts of Interest

The authors declare that they have no conflicts of interest.

Authors' Contributions

Sang A Park and Soi Jeong contributed equally. Sang A Park and Soi Jeong performed the experiments and wrote the manuscript. Young Ho Choe performed the experiments. Young-Min Hyun conceived the study, performed the experiments, and wrote the manuscript.

Acknowledgments

This study was supported by the faculty research grant of Yonsei University College of Medicine (6-2016-0132) and the National Research Foundation of Korea (NRF) grant funded by the Korean government (MSIP) (2016R1A2B4008199) (Young-Min Hyun) and the Ministry of Health & Welfare, Republic of Korea (Grant no. H114C1324).

Supplementary Materials

Supplementary 1. Video 1: transient and local vascular leakage during CXCL2 stimulated blood vessel.

Supplementary 2. Video 2: spatiotemporal vascular rupture induced vascular permeability increase.

References

- [1] G. Egawa, S. Nakamizo, Y. Natsuaki, H. Doi, Y. Miyachi, and K. Kabashima, "Intravital analysis of vascular permeability in mice using two-photon microscopy," *Scientific Reports*, vol. 3, no. 1, p. 1932, 2013.
- [2] D. Mehta and A. B. Malik, "Signaling mechanisms regulating endothelial permeability," *Physiological Reviews*, vol. 86, no. 1, pp. 279–367, 2006.
- [3] E. Vandembroucke, D. Mehta, R. Minshall, and A. B. Malik, "Regulation of endothelial junctional permeability," *Annals of the New York Academy of Sciences*, vol. 1123, no. 1, pp. 134–145, 2008.
- [4] J. A. Nagy, L. Benjamin, H. Zeng, A. M. Dvorak, and H. F. Dvorak, "Vascular permeability, vascular hyperpermeability and angiogenesis," *Angiogenesis*, vol. 11, no. 2, pp. 109–119, 2008.
- [5] E. Dejana, R. Spagnuolo, and G. Bazzoni, "Interendothelial junctions and their role in the control of angiogenesis, vascular permeability and leukocyte transmigration," *Thrombosis and Haemostasis*, vol. 86, no. 7, pp. 308–315, 2001.
- [6] J. Gavard and J. S. Gutkind, "VEGF controls endothelial-cell permeability by promoting the beta-arrestin-dependent endocytosis of VE-cadherin," *Nature Cell Biology*, vol. 8, no. 11, pp. 1223–1234, 2006.
- [7] D. M. McDonald and P. Baluk, "Significance of blood vessel leakiness in cancer," *Cancer Research*, vol. 62, no. 18, pp. 5381–5315, 2002.
- [8] H. F. Dvorak, "Vascular permeability factor/vascular endothelial growth factor: a critical cytokine in tumor angiogenesis and a potential target for diagnosis and therapy," *Journal of Clinical Oncology*, vol. 20, no. 21, pp. 4368–4380, 2002.
- [9] H. Maeda, J. Wu, T. Sawa, Y. Matsumura, and K. Hori, "Tumor vascular permeability and the EPR effect in macromolecular therapeutics: a review," *Journal of Controlled Release*, vol. 65, no. 1-2, pp. 271–284, 2000.
- [10] Y. M. Hyun, R. Sumagin, P. P. Sarangi et al., "Uropod elongation is a common final step in leukocyte extravasation through inflamed vessels," *Journal of Experimental Medicine*, vol. 209, no. 7, pp. 1349–1362, 2012.
- [11] S. Baez, "An open cremaster muscle preparation for the study of blood vessels by in vivo microscopy," *Microvascular Research*, vol. 5, no. 3, pp. 384–394, 1973.
- [12] P. Kumar, Q. Shen, C. D. Pivetti, E. S. Lee, M. H. Wu, and S. Y. Yuan, "Molecular mechanisms of endothelial hyperpermeability: implications in inflammation," *Expert Reviews in Molecular Medicine*, vol. 11, 2009.
- [13] N. Faust, F. Varas, L. M. Kelly, S. Heck, and T. Graf, "Insertion of enhanced green fluorescent protein into the lysozyme gene creates mice with green fluorescent granulocytes and macrophages," *Blood*, vol. 96, no. 2, pp. 719–726, 2000.
- [14] D. Kreisel, R. G. Nava, W. Li et al., "In vivo two-photon imaging reveals monocyte-dependent neutrophil extravasation during pulmonary inflammation," *Proceedings of the National Academy of Sciences*, vol. 107, no. 42, pp. 18073–18078, 2010.

- [15] D. Feng, J. A. Nagy, K. Pyne, H. F. Dvorak, and A. M. Dvorak, "Neutrophils emigrate from venules by a transendothelial cell pathway in response to FMLP," *Journal of Experimental Medicine*, vol. 187, no. 6, pp. 903–915, 1998.
- [16] G. F. Elphick, P. P. Sarangi, Y.-M. Hyun et al., "Recombinant human activated protein C inhibits integrin-mediated neutrophil migration," *Blood*, vol. 113, no. 17, pp. 4078–4085, 2009.
- [17] L. Zhu and P. He, "fMLP-stimulated release of reactive oxygen species from adherent leukocytes increases microvessel permeability," *American Journal of Physiology-Heart and Circulatory Physiology*, vol. 290, no. 1, pp. 365–372, 2006.
- [18] P. He, "Leucocyte/endothelium interactions and microvessel permeability: coupled or uncoupled?," *Cardiovascular Research*, vol. 87, no. 2, pp. 281–290, 2010.
- [19] P. Baluk, P. Bolton, A. Hirata, G. Thurston, and D. M. McDonald, "Endothelial gaps and adherent leukocytes in allergen-induced early- and late-phase plasma leakage in rat airways," *American Journal of Pathology*, vol. 152, no. 6, pp. 1463–1476, 1998.
- [20] D. O. Bates, "Vascular endothelial growth factors and vascular permeability," *Cardiovascular Research*, vol. 87, no. 2, pp. 262–271, 2010.
- [21] M. Martins-Green, M. Petreaca, and M. Yao, "An assay system for in vitro detection of permeability in human "endothelium"," *Methods in Enzymology*, vol. 443, pp. 137–153, 2008.
- [22] M. Radu and J. Chernoff, "An in vivo assay to test blood vessel permeability," *Journal of Visualized Experiments*, vol. 73, p. e50062, 2013.
- [23] E. D. Han, R. C. MacFarlane, A. N. Mulligan, J. Scafidi, and A. E. Davis, "Increased vascular permeability in C1 inhibitor-deficient mice mediated by the bradykinin type 2 receptor," *Journal of Clinical Investigation*, vol. 109, pp. 1057–1063, 2002.

Research Article

A Pyridazine-Based Fluorescent Probe Targeting A β Plaques in Alzheimer's Disease

Yong Dae Park ¹, Jeum-Jong Kim,² Sungbeom Lee,¹ Chul-Hong Park,¹
Hyung-Woo Bai,¹ and Seung Sik Lee¹

¹Research Division for Biotechnology, Advanced Radiation Technology Institute, Korea Atomic Energy Research Institute, Jeongseup 580-185, Republic of Korea

²Technology Innovation Support Team, Korea Research Institute of Chemical Technology (KRICT), Deajeon 305-600, Republic of Korea

Correspondence should be addressed to Yong Dae Park; ydpark@kaeri.re.kr

Received 10 October 2017; Accepted 14 December 2017; Published 27 February 2018

Academic Editor: Subhankar Singha

Copyright © 2018 Yong Dae Park et al. This is an open access article distributed under the Creative Commons Attribution License, which permits unrestricted use, distribution, and reproduction in any medium, provided the original work is properly cited.

Accumulation of β -amyloid (A β) plaques comprising A β 40 and A β 42 in the brain is the most significant factor in the pathogenesis of Alzheimer's disease (AD). Thus, the detection of A β plaques has increasingly attracted interest in the context of AD diagnosis. In the present study, a fluorescent pyridazine-based dye that can detect and image A β plaques was designed and synthesized, and its optical properties in the presence of A β aggregates were evaluated. An approximately 34-fold increase in emission intensity was exhibited by the fluorescent probe after binding with A β aggregates, for which it showed high affinity ($K_D = 0.35 \mu\text{M}$). Moreover, the reasonable hydrophobic properties of the probe ($\log P = 2.94$) allow it to penetrate the blood brain barrier (BBB). In addition, the pyridazine-based probe was used in the histological costaining of transgenic mouse (APP/PS1) brain sections to validate the selective binding of the probe to A β plaques. The results suggest that the pyridazine-based compound has the potential to serve as a fluorescent probe for the diagnosis of AD.

1. Introduction

The misfolding and aggregation of proteins cause numerous neurodegenerative diseases, such as Alzheimer's disease (AD), prion disease (PrD), and Parkinson's disease (PD) [1]. AD, one of the most common protein misfolding diseases (PMDs), is characterized by the accumulation of misfolded β -amyloid (A β) peptides and neurofibrillary tangles (NFTs) containing tau protein in the brain. A recent report revealed that the buildup of A β plaques in the brain plays a significant role in the pathogenesis of AD [2, 3]. Therefore, approaches to visualize A β deposition might prove useful for diagnosing AD and evaluating the efficacy of AD therapeutics [4–6].

Several groups have reported novel positron emission tomography (PET) imaging agents targeting A β plaques to diagnose AD, including BAY94-9172, FDDNP, PIB, SB-13, AV-45, and IMPY [7–13]. However, these agents are hindered by factors such as long data acquisition processes,

costly equipment, exposure to radioactivity, need for proficient personnel, and comparatively poor spatial resolution [14]. Interest in monitoring the progression of AD by imaging A β plaques using fluorescence spectroscopy has also increased [15, 16]. Compared to nuclear imaging methods, fluorescence imaging has many advantages, including providing real-time, nonradioactive, inexpensive, and high-resolution imaging, both in vivo and ex vivo. Consequently, various fluorescent probes for imaging A β plaques have been developed [17–22]. An excellent fluorescent probe for A β plaques must meet the following requirements [18, 21, 23]: (1) selective targeting of A β plaques, (2) acceptable lipophilicity ($\log P$ value between 1 and 3), (3) high-affinity binding, (4) straightforward synthesis, and (5) a significant change in fluorescent properties upon binding to A β deposits.

Based on these requirements, we developed and reported fluorescent pyridazine probes targeting A β plaques [24].

These pyridazine probes can be used for imaging through selective binding but lack the required binding affinity for A β plaques. Here, we describe the optimization of pyridazine derivatives based on the conjugation of an electron acceptor with an electron donor.

To optimize these fluorescent probes, the electron-donating *p*-dimethylamino group and electron-accepting cyano group were introduced to construct a compound with a donor- π -acceptor structure (Figure 1). In this paper, we describe the synthesis and optical and biological properties of a cyano-based probe based on pyridazine. The *ex vivo* staining of A β plaques in APP/PS1 mice brain sections by this fluorescent probe is also presented.

2. Materials and Methods

2.1. General Experimental Methods. ^1H NMR spectra were recorded in CDCl_3 unless otherwise noted (values in ppm) using TMS as the standard with a JNM-ECA 500 spectrometer. Low resolution mass spectra were recorded using a Varian MAT 212 mass spectrometer. IR spectra (KBr) were measured with a Bruker-Vector 22 instrument (Bruker, Bremen). Flash column chromatography was performed using silica gel (70–230 mesh). All reagent-grade chemicals were purchased from Sigma-Aldrich (St. Louis, MO, USA), and synthetic A β_{42} peptide was purchased from rPeptide (Bogart, GA, USA).

2.2. Synthesis and Characterization of Catechol Aldehyde (2). A mixture of **1** (300 mg, 0.97 mmol), 3,4-dihydroxybenzaldehyde (147 mg, 1.06 mmol), and K_2CO_3 (293 mg, 2.12 mmol) was dissolved in DMF (20 ml) and refluxed for 24 h. After evaporating the solvent under reduced pressure, H_2O (100 ml) and methylene chloride (50 ml) were added. The organic layer was separated and dried over MgSO_4 . The pure product (**2**) was obtained by column chromatography on silica gel using CH_2Cl_2 as the eluent. Yield: 89%. IR (KBr) = 3091, 2920, 2852, 1691, 1671, 1647, 1605, 1590, 1526, 1499, 1364, 1280, 1188. ^1H NMR (CDCl_3) = 9.83 (s, 1H), 8.01 (d, 1H, J = 13.75 Hz), 7.67 (s, 1H), 7.54–7.38 (m, 4H), 7.18–6.99 (m, 2H), 6.69 (d, 2H, J = 8.70 Hz), 2.98 (s, 6H). MS (EI) m/z 375 [M] $^+$, 188, 159, 145, 117.

2.3. Synthesis and Characterization of Probe 3. A mixture of **2** (100 mg, 0.27 mmol) and cyanoacetic acid (30 mg, 0.36 mmol) was vacuum dried, and CHCl_3 (50 ml) and piperidine were added. The solution was refluxed for 15 h. Then, H_2O (50 ml) was added. The organic layer was separated and dried over MgSO_4 . The pure product (**3**) was obtained by column chromatography on silica gel (CH_2Cl_2 : MeOH = 6 : 1). Yield: 58%. IR (KBr) = 3398, 3091, 2922, 2853, 2211, 1651, 1632, 1603, 1524, 1503, 1363, 1335, 1277, 1187, 1163, 1125. ^1H -NMR (CDCl_3) = 8.04 (d, 1H, J = 6.86 Hz), 7.81 (d, 1H, J = 14.25 Hz), 7.80 (s, 1H), 7.55–7.51 (m, 2H), 7.37–7.33 (dd, 2H, J = 8.56, 8.52 Hz), 7.18–7.09 (m, 1H), 6.99 (d, 1H, J = 14.29 Hz), 6.66 (d, 2H, J = 7.42 Hz), 2.89 (s, 6H). MS (EI) m/z 398 [$\text{M}-\text{CO}_2$] $^+$, 382, 256, 145, 129, 111, 97, 83, 78, 63.

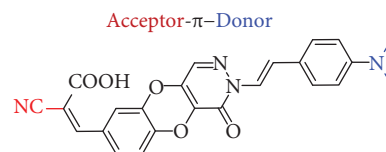


FIGURE 1: Chemical structure of fluorescent probe 3.

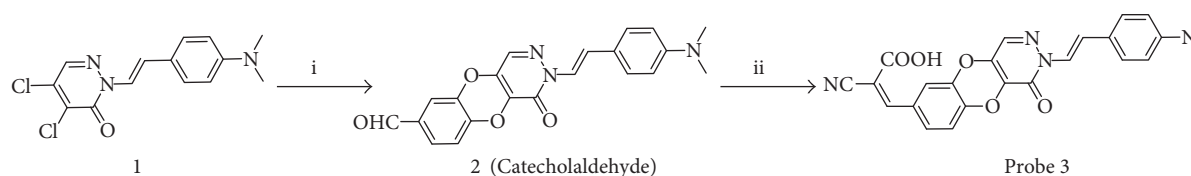
2.4. UV/VIS and Fluorescence Analysis. UV/VIS and fluorescence spectra were recorded and analyzed. For the UV/VIS spectra, an Infinite M200 Pro Microplate reader (Tecan, Switzerland) equipped with cells with a 1.0 cm path length was used. The scan rate was 120 nm/min. The excitation and emission λ_{max} values of probe **3** (10 μM) were recorded with a detector (slit of 1 mm) and a data interval of 5 nm in DMF.

2.5. Preparation of A β 42 Aggregates and Fluorescence Spectrum Measurement. Aggregated A β peptide was prepared by diluting A β 42 to a final concentration of 100 μM in PBS (pH 7.4). This solution was incubated at 200 rpm and 37°C for 3 days. The formation of A β fibrils was confirmed by ThT assay. The excitation and emission λ_{max} values of probe **3** were measured using an Infinite M200 Pro Microplate reader (Tecan, Switzerland) equipped with a detector (slit 1 mm) with a data interval of 5 nm. The scan rate was 120 nm/min. Probe **3** (10 μM) was reacted with and without 20 μM A β aggregates for 20 min in PBS at 37°C. The emission spectra and fluorescence intensity of the samples were measured. The fold increase was calculated by comparing the fluorescence intensity with and without 20 μM A β aggregates.

2.6. Binding Constant (K_D) Measurement. A 10 μM solution of aggregated A β 42 was combined with probe **3** (0.1, 0.5, 1, 2, 5, and 10 μM) in PBS (pH 7.4). The solutions were incubated for 10 min at 37°C, and then their fluorescence intensity was determined at 408 nm (excitation wavelength). K_D was determined as described previously [25].

2.7. Lipophilicity (log P). Probe **3** was added to a premixed suspension containing 500 μL of octanol and 500 μL of PBS solution, and the resulting suspension was vortexed vigorously for 10 min and centrifuged at 3000 rpm for 5 min. Two layers separated out, and 100 μL aliquots from octanol and the PBS solution layers were removed and analyzed for their fluorescence intensity. The log P value was calculated as the logarithm of the ratio of the fluorescence intensity in octanol versus that in PBS solution.

2.8. Maestro Images Analysis. An optical data study was performed using a Maestro 2.0 *in vivo* imaging system. The images were acquired as described previously [25]. Solutions of probe **3** (1 μM) were prepared with and without 20 μM A β aggregates in PBS. Fluorescence emission was obtained by analyzing the resulting images with commercial software (Maestro™ 2.4).



SCHEME 1: Reaction scheme for the synthesis of the pyridazine-based probe (3). (i) DMF, 3,4-dihydroxybenzaldehyde, K_2CO_3 , refluxed for 24 h; (ii) $CHCl_3$, cyanoacetic acid, piperidine, refluxed for 15 h.

2.9. Histological Costaining with $A\beta$ Antibody and Probe 3

The brain from 12-month-old transgenic APP/PS1 mice was removed and cut into $5\ \mu\text{m}$ sections. The mouse brain sections were stained with probe 3 and anti- $A\beta$ using the following method: first, the brain sections were equilibrated in PBS solution for 10 min, washed with PBS containing 0.1% Tween 20 (PBS-T) and 5% BSA for 30 min, and washed again with PBS-T supplemented with 1% BSA for 5 min 3 times. Second, the washed sections were incubated with primary antibody (rabbit anti- $A\beta$, 1 : 100 dilution in PBS-T supplemented with 1% BSA) overnight at 4°C , washed with PBS-T supplemented with 1% BSA 3 times, and stained with secondary antibody (Alexa 555 goat antirabbit IgG, 1 : 100 dilution in PBS-T supplemented with 1% BSA). After washing with PBS, the prestained sections were stained with $10\ \mu\text{M}$ probe 3 for 30 min. The stained section was washed with PBS and analyzed under an FV1000D (Olympus, Tokyo, Japan) confocal laser scanning microscope.

3. Results and Discussion

The synthesis of probe 3 is outlined in Scheme 1. First, commercially available 3,4-dihydroxybenzaldehyde was converted to the corresponding catechol aldehyde (2) by reacting it with compound 1. The Knövenagel condensation of compound 2 with cyanoacetic acid afforded the final fluorescent probe (3).

The optical properties of the synthesized fluorescent probe (3) with aggregated $A\beta_{42}$ peptides in PBS (pH 7.4) were analyzed, and the results are shown at Table 1. Probe 3 exhibited an excitation maximum at 408 nm and an emission maximum at 670 nm (Table 1 and Figure 2).

To operate as a fluorescent probe targeting $A\beta$ plaques, a compound must show a significant rise in fluorescence intensity upon binding with $A\beta$ aggregates compared to the fluorescence intensity of free $A\beta$ aggregates in solution [15]. Therefore, we compared the fluorescence intensity of probe 3 to the fluorescence intensity of the probe in the presence of $A\beta$ aggregates (Figure 3(a)). As shown in Table 1, we observed a remarkable increase (35-fold) in the fluorescence intensity of probe 3 in the presence of $A\beta$ aggregates. Additionally, the gain in fluorescence intensity was visually confirmed using a Maestro fluorescence imaging system (Figure 3(c)). This effect is due to conformational changes: When the probe in solution with $A\beta$ aggregates is in the unbound state, free rotation through a single bond is permitted, whereas upon binding to $A\beta$ aggregates, the probe exhibits a significant increase in fluorescence intensity due to restricted movement [26]. The binding of probe 3 to $A\beta$ aggregates was also accompanied by a blueshift in the

TABLE 1: Fluorescence profile and K_D and $\log P$ values of probe 3 with $A\beta$ aggregates.

Optical properties	Probe 3
λ_{ex} (nm)	408
λ_{em} (nm)	670
$\lambda_{\text{ex}}/\lambda_{\text{em}}$ with $A\beta$ (nm)	408/604
Fold increase with $A\beta$	34.92
K_D (mean \pm SD) (μM)	0.35 ± 0.03
$\log P$ (lipophilicity)	2.94

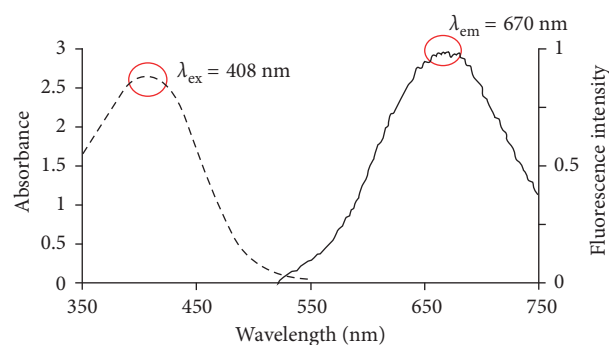


FIGURE 2: Absorbance and emission spectra of probe 3 in DMF. The maximum wavelengths in the absorbance and emission spectra are 408 nm and 670 nm, respectively.

emission spectrum [15]. The emission wavelength of probe 3 exhibited significant blueshifts (66 nm, Table 1), indicating that probe 3 likely intercalated into the hydrophobic pocket of the $A\beta$ aggregates. This result suggested that probe 3 could be “turned on” via an increase in fluorescence intensity and a blueshift in its emission wavelength upon interacting with $A\beta$ aggregates.

Next, we measured the apparent binding constant (K_D) of fluorescent probe 3 to $A\beta$ aggregates. The fluorescence intensity of solutions of probe 3 at various concentrations in the presence of $A\beta$ aggregates was measured, revealing that the K_D value of probe 3 was $0.35 \pm 0.03\ \mu\text{M}$ (Table 1 and Figure 3(b)). This binding constant was significantly higher than that of our previously reported fluorescence probe, probe 1 ($1.83 \pm 0.31\ \mu\text{M}$) [24]. The lipophilicity ($\log P$) of probe 3 was also evaluated to determine whether it could permeate through the blood brain barrier (BBB). The $\log P$ value of probe 3 was found to be 2.94 (Table 1), suggesting that probe 3 has desirable properties regarding BBB permeability [21].

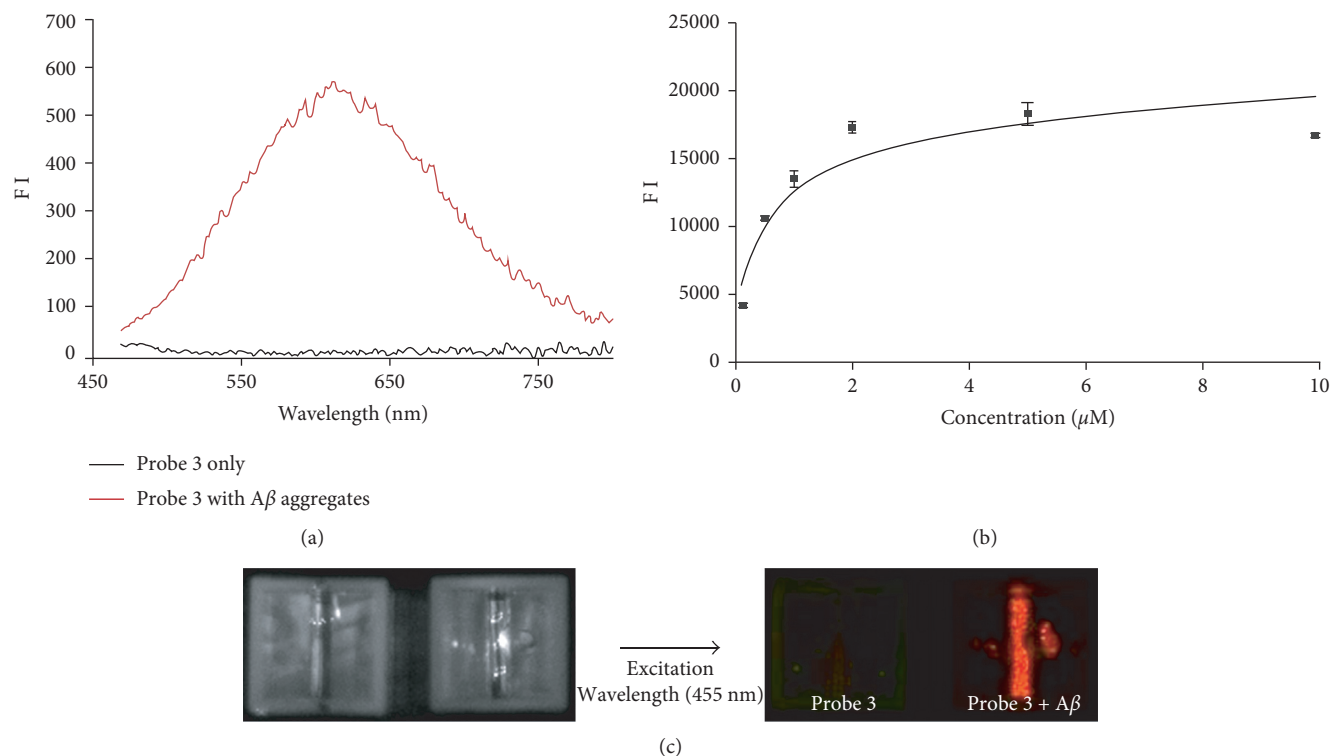


FIGURE 3: Emission spectra of probe 3 in the presence and absence of $A\beta$ aggregates (a) and a plot of the fluorescence intensity (at $\lambda_{em} = 604$) as a function of the concentration of probe 3 in the presence of $A\beta$ aggregates ($10 \mu\text{M}$) in PBS (b). The apparent dissociation constant (K_D) was $0.35 \pm 0.03 \mu\text{M}$. (c) Imaging of the fluorescence intensity of probe 3 and $A\beta_{42}$ aggregates using a Maestro imaging system.

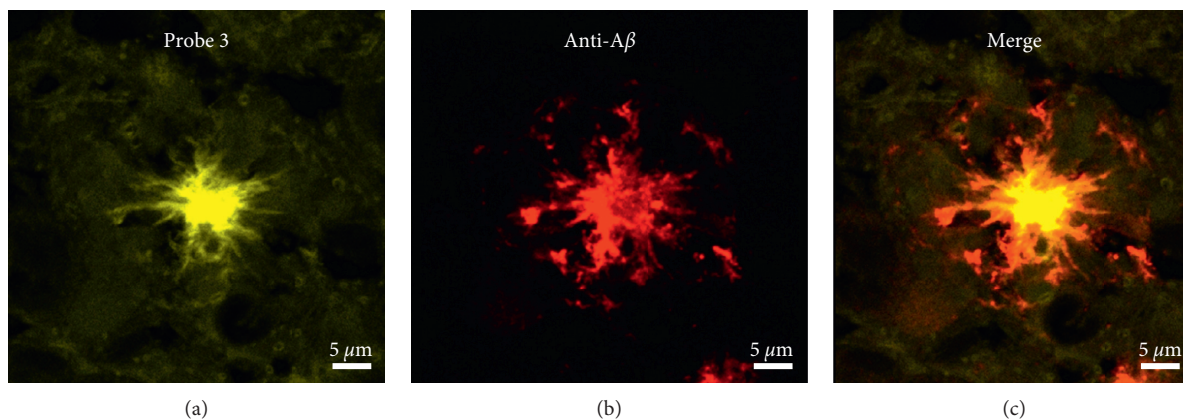


FIGURE 4: Histological double staining of $5 \mu\text{m}$ double sections from the cortex of APP/PS1 mouse brains with probe 3 and anti- $A\beta$. All of the images were acquired at a certain excitation wavelength (anti- $A\beta$: 555 nm and probe 3: 408 nm) by a confocal laser scanning microscope.

The probe developed in this paper, probe 3, meets the requirements for a fluorescence imaging probe for AD: high fluorescence receptivity, strong binding affinity, and hydrophobicity. To assess whether fluorescent probe 3 could stain $A\beta$ plaques in mouse brain tissue, we further evaluated the histological costaining of $A\beta$ plaques in APP/PS1 mouse brain sections with probe 3 and anti- $A\beta$. $A\beta$ plaques in the mouse brain section were identified by staining with anti- $A\beta$ as a control. As shown in Figure 4, the brain section exposed to probe 3 exhibited significant fluorescence. Notably, the merged images showed colocalization of the areas stained

with probe 3 and anti- $A\beta$, which demonstrates the selective targeting of $A\beta$ plaques by probe 3.

4. Conclusions

In summary, we successfully synthesized probe 3 as a novel $A\beta$ plaque-targeting fluorescent probe by applying the concept of a donor- π -acceptor structure to the scaffold of a previously reported pyridazine dye, probe 1. Probe 3 exhibited a strong fluorescence response ($F_{A\beta}/F_0 > 34$ -fold), high affinity for $A\beta_{42}$ aggregates ($K_D = 0.35 \pm 0.03 \mu\text{M}$), and

sufficient hydrophobicity to penetrate the BBB (log $P = 2.94$). Furthermore, probe **3** specifically stained the $A\beta$ plaques in APP/PS1 mouse brain sections. These results indicate probe **3** as a novel fluorescence imaging agent for the study of AD.

Conflicts of Interest

The authors declare that they have no conflicts of interest.

Acknowledgments

This project was supported by the Ministry of Science and ICT (MIST), Republic of Korea.

References

- [1] G. Edwards III, I. Moreno-Gonzalez, and C. Soto, "Amyloid-beta and tau pathology following repetitive mild traumatic brain injury," *Biochemical and Biophysical Research Communications*, vol. 483, no. 4, pp. 1137–1142, 2017.
- [2] E. D. Roberson and L. Mucke, "100 years and counting: prospects for defeating Alzheimer's disease," *Science*, vol. 314, no. 5800, pp. 781–784, 2006.
- [3] J. H. Kim, J. Lee, S. Lee, and E. J. Cho, "Quercetin and quercetin-3- β -d-glucoside improve cognitive and memory function in Alzheimer's disease mouse," *Applied Biological Chemistry*, vol. 59, no. 5, pp. 721–728, 2016.
- [4] C. A. Mathis, Y. Wang, and W. E. Klunk, "Imaging beta-amyloid plaques and neurofibrillary tangles in the aging human brain," *Current Pharmaceutical Design*, vol. 10, no. 13, pp. 1469–1492, 2004.
- [5] A. Nordberg, "PET imaging of amyloid in Alzheimer's disease," *The Lancet Neurology*, vol. 3, no. 9, pp. 519–527, 2004.
- [6] D. J. Selkoe, "Imaging Alzheimer's amyloid," *Nature Biotechnology*, vol. 18, no. 8, pp. 823–824, 2000.
- [7] E. D. Agdeppa, V. Kepe, J. Liu et al., "Binding characteristics of radiofluorinated 6-dialkylamino-2-naphthylethyldene derivatives as positron emission tomography imaging probes for beta-amyloid plaques in Alzheimer's disease," *Journal of Neuroscience*, vol. 21, no. 24, p. RC189, 2001.
- [8] H. F. Kung, S. R. Choi, W. Qu, W. Zhang, and D. Skovronsky, "18F stilbenes and styrylpyridines for PET imaging of $A\beta$ plaques in Alzheimer's disease: a miniperspective," *Journal of Medicinal Chemistry*, vol. 53, no. 3, pp. 933–941, 2010.
- [9] C. A. Mathis, Y. Wang, D. P. Holt, G. F. Huang, M. L. Debnath, and W. E. Klunk, "Synthesis and evaluation of 11C-labeled 6-substituted 2-arylbenzothiazoles as amyloid imaging agents," *Journal of Medicinal Chemistry*, vol. 46, no. 13, pp. 2740–2754, 2003.
- [10] N. Okamura, Y. Shiga, S. Furumoto et al., "In vivo detection of prion amyloid plaques using [(11)C]BF-227 PET," *European Journal of Nuclear Medicine and Molecular Imaging*, vol. 37, no. 5, pp. 934–941, 2010.
- [11] M. Ono, A. Wilson, J. Nobrega et al., "11C-labeled stilbene derivatives as $A\beta$ -aggregate-specific PET imaging agents for Alzheimer's disease," *Nuclear Medicine and Biology*, vol. 30, no. 6, pp. 565–571, 2003.
- [12] C. C. Rowe, U. Ackerman, W. Browne et al., "Imaging of amyloid beta in Alzheimer's disease with 18F-BAY94-9172, a novel PET tracer: proof of mechanism," *The Lancet Neurology*, vol. 7, no. 2, pp. 129–135, 2008.
- [13] Z. P. Zhuang, M. P. Kung, A. Wilson et al., "Structure-activity relationship of imidazo[1,2-a]pyridines as ligands for detecting beta-amyloid plaques in the brain," *Journal of Medicinal Chemistry*, vol. 46, no. 2, pp. 237–243, 2003.
- [14] R. Weissleder and U. Mahmood, "Molecular imaging," *Radiology*, vol. 219, no. 2, pp. 316–333, 2001.
- [15] W. M. Chang, M. Dakanali, C. C. Capule, C. J. Sigurdson, J. Yang, and E. A. Theodorakis, "ANCA: a family of fluorescent probes that bind and stain amyloid plaques in human tissue," *ACS Chemical Neuroscience*, vol. 2, no. 5, pp. 249–255, 2011.
- [16] G. Yu, H. Jung, and H. Mok, "Indocyanine green-incorporated exosomes for improved in vivo imaging of sentinel lymph node," *Applied Biological Chemistry*, vol. 59, no. 1, pp. 71–76, 2016.
- [17] M. Hintersteiner, A. Enz, P. Frey et al., "In vivo detection of amyloid-beta deposits by near-infrared imaging using an oxazine-derivative probe," *Nature Biotechnology*, vol. 23, no. 5, pp. 577–583, 2005.
- [18] E. E. Nesterov, J. Skoch, B. T. Hyman, W. E. Klunk, B. J. Bacskai, and T. M. Swager, "In vivo optical imaging of amyloid aggregates in brain: design of fluorescent markers," *Angewandte Chemie International Edition*, vol. 44, no. 34, pp. 5452–5456, 2005.
- [19] S. B. Raymond, J. Skoch, I. D. Hills, E. E. Nesterov, T. M. Swager, and B. J. Bacskai, "Smart optical probes for near-infrared fluorescence imaging of Alzheimer's disease pathology," *European Journal of Nuclear Medicine and Molecular Imaging*, vol. 35, no. S1, pp. S93–S98, 2008.
- [20] Q. Li, J. S. Lee, C. Ha et al., "Solid-phase synthesis of styryl dyes and their application as amyloid sensors," *Angewandte Chemie International Edition*, vol. 43, no. 46, pp. 6331–6335, 2004.
- [21] C. Ran, X. Xu, S. B. Raymond et al., "Design, synthesis, and testing of difluoroboron-derivatized curcumins as near-infrared probes for in vivo detection of amyloid-beta deposits," *Journal of the American Chemical Society*, vol. 131, no. 42, pp. 15257–15261, 2009.
- [22] M. Ono, M. Ishikawa, H. Kimura et al., "Development of dual functional SPECT/fluorescent probes for imaging cerebral beta-amyloid plaques," *Bioorganic and Medicinal Chemistry Letters*, vol. 20, no. 13, pp. 3885–3888, 2010.
- [23] W. E. Klunk, H. Engler, A. Nordberg et al., "Imaging brain amyloid in Alzheimer's disease with Pittsburgh Compound-B," *Annals of Neurology*, vol. 55, no. 3, pp. 306–319, 2004.
- [24] Y. D. Park, J. H. Park, M. G. Hur et al., "Fluorescent 2-styrylpyridazin-3(2H)-one derivatives as probes targeting amyloid-beta plaques in Alzheimer's disease," *Bioorganic and Medicinal Chemistry Letters*, vol. 22, no. 12, pp. 4106–4110, 2012.
- [25] S. J. Jung, S. H. Park, E. J. Lee et al., "Development of fluorescent probes that bind and stain amyloid plaques in Alzheimer's disease," *Archives of Pharmacal Research*, vol. 38, no. 11, pp. 1992–1998, 2015.
- [26] M. Staderini, M. A. Martin, M. L. Bolognesi, and J. C. Menendez, "Imaging of beta-amyloid plaques by near infrared fluorescent tracers: a new frontier for chemical neuroscience," *Chemical Society Reviews*, vol. 44, no. 7, pp. 1807–1819, 2015.